Palaeogeography, Palaeoclimatology, Palaeoecology 613 (2023) 111373

Contents lists available at ScienceDirect

Palaeogeography, Palaeoclimatology, Palaeoecology

journal homepage: www.elsevier.com/locate/palaeo

Invited Research Article

Cretaceous climates: Mapping paleo-Köppen climatic zones using a Bayesian statistical analysis of lithologic, paleontologic, and geochemical proxies

Landon Burgener [a,*], Ethan Hyland [b], Brian J. Reich [c], Christopher Scotese [d]

[a] Department of Geological Sciences, Brigham Young University, Provo, UT 84602, USA
[b] Department of Marine, Earth, and Atmospheric Sciences, North Carolina State University, Raleigh, NC 27695, USA
[c] Department of Statistics, North Carolina State University, Raleigh, NC 27695, USA
[d] Department of Earth and Planetary Sciences, Northwestern University, Evanston, IL 60208, USA

ARTICLE INFO

Editor: H. Falcon-Lang

Keywords:
Paleoclimate
Cretaceous
Köppen
Palaeogeography
Bayesian statistics
Climate proxies
GIS

ABSTRACT

The Cretaceous Period (145 to 66 Ma) was a prolonged warmhouse to hothouse period characterized by high atmospheric CO_2 conditions, elevated surface temperatures, and an enhanced global hydrologic cycle. It provides a case study for understanding how a hothouse climate system operates, and is an analog for future anthropogenic climate change scenarios. This study presents new quantitative temperature and precipitation proxy datasets for nine key Cretaceous time slices (Berriasian/Valanginian, Hauterivian/Barremian, Aptian, Albian, Cenomanian, Turonian, Coniacian/Santonian, Campanian, Maastrichtian), and a new geostatistical analysis technique that utilizes Markov Chain Monte Carlo algorithm and Bayesian hierarchical models to generate high resolution, quantitative global paleoclimate reconstructions from these proxy datasets, with associated uncertainties. Using these paleoclimate reconstructions, paleo-Köppen (-Geiger) climate zone maps are produced that provide new insights into the changing spatial and temporal climate patterns during the Cretaceous. These new paleoclimate reconstructions and paleo-Köppen climate maps provide new insight into the timing of the initiation of the Early Cretaceous equatorial humid belt over Gondwana and reveal temporal shifts in the width of the subtropical arid belts from the Early to mid- to Late Cretaceous. A comparison of these proxy-based reconstructions and model simulations of Cretaceous climate reveal continued proxy/model differences. In addition, the methodology developed for this study can be applied to other time periods, providing a framework for better understanding ancient climate, environments, and ecosystems.

1. Introduction

1.1. *Cretaceous paleoclimate methodologies*

This paper presents a new synthesis of global climate for nine subdivisions of the Cretaceous Period (145 Ma – 66 Ma) in the form of quantitative temperature and precipitation reconstructions and paleo-Köppen(-Geiger) climate zone maps. The Cretaceous was a warmhouse to hothouse world that was generally characterized by hot to temperate continental climates that stretched from pole to equator (Scotese et al., 2021). During the cooler, early Cretaceous, there is some evidence for snow and ice at high latitudes, but no geological evidence of permanent ice caps. If permanent icecaps were present they would have been small (20% the size of the modern Antarctic icesheet) and ephemeral (Bornemann et al., 2008; Ladant and Donnadieu, 2016). In many respects, the Cretaceous was the antithesis of the ice house worlds of the last 40 million years during which time the South Pole and more recently the North Pole (~last five million years), were covered in snow and ice. Though the climates of the Cretaceous were very different from the modern climate system, they represent a natural laboratory for studying how earth's climate may evolve under future climate change scenarios.

The history of the Earth's changing climate has been the subject of numerous studies (e.g., Vaughan, 2007; Valdes et al., 2018; Mills et al., 2019; Scotese et al., 2021; Judd et al., 2021a, 2021b; Grossman and Joachimski, 2022). The goal of these investigations has been to better understand how the Earth's climate has changed through time and to use this knowledge to understand aspects of modern climate and predict future climate change (Tierney et al., 2020, Scotese, 2021; Skea, 2022).

---

* Corresponding author.
E-mail address: landon.burgener@byu.edu (L. Burgener).

https://doi.org/10.1016/j.palaeo.2022.111373
Received 1 September 2022; Received in revised form 21 December 2022; Accepted 22 December 2022

Table 1
Cretaceous quantitative and censored paleoclimate data summary for the nine analysis windows.[a]

Age/Stage	MAT		WMMT		MAP		Coal (censored)	Stage Totals	
	n (quantitative)	n (censored)	n (quantitative)	n (censored)	n (quantitative)	n (censored)		n (quantitative)	n (censored)
Berriasian/ Valanginian	297	83	1	382	5	290	403	303	1158
Hauterivian/ Barremian	499	125	0	628	6	394	433	505	1580
Aptian	739	189	56	856	13	572	501	808	2118
Albian	1130	197	12	1311	10	411	562	1152	2481
Cenomanian	1124	214	244	1088	15	379	400	1383	2081
Turonian	1014	184	22	1177	10	311	279	1046	1951
Coniacian/ Santonian	480	233	66	640	17	324	363	563	1560
Campanian	1286	328	66	1548	20	424	612	1372	2912
Maastrichtian	1286	567	82	1851	50	593	499	1418	3510
Total	7855	2120	549	9481	146	3698	4052	8550	19,351

a - Depending on a sample's age uncertainty, it may be included in multiple analysis windows.

Though these studies share the same goal, the methods and data that they have employed differed. These investigations can be grouped into one modelling and two proxy-based categories: 1) computer simulations of global paleoclimate (e.g., Huber, 2012; Valdes et al., 2017; Haywood et al., 2019; Valdes et al., 2021), 2) quantitative reconstructions of climate parameters using various isotopic and molecular systems (e.g., δ^{18}O, clumped isotopes, and TEX$_{86}$; Royer et al., 2004; Grossman, 2012a, 2012b; Veizer and Prokoph, 2015; O'Brien et al., 2017; Song et al., 2019; Vérard and Veizer, 2019; Grossman and Joachimski, 2020, 2022), and 3) censored climate estimates from geological and paleontological proxies (Wegener, 1912a, 1912b, 1915; Du Toit, 1937; Frakes, 1979; Habicht, 1979; Frakes et al., 1992; Parrish et al., 1982; Sellwood and Price, 1994; Parrish, 1998; Ziegler et al., 1985; Boucot et al., 2013; Cao et al., 2019). Here the term “censored” refers to truncated or limited observations where the value is only partially known (e.g., “greater than 30 °C" or “<500 mm yr^{-1}). This terminology is not often encountered in the geologic literature, but is common in the medical and statistical fields (see Wijeysundera et al., 2012 and references therein).

Numerous authors have employed either the second or third approaches separately, using quantitative climate proxies or lithologic and paleontologic indicators to decipher past climates (see references in previous paragraph). However, recent improvements in quantitative paleoclimate proxies (e.g., Eiler, 2011; Hyland et al., 2015; Reichgelt et al., 2018), the expansion of spatial and temporal proxy availability (e.g., Tabor et al., 2016; Burgener et al., 2021), refinements in paleoclimate zone classification schemes (e.g., Zhang et al., 2016), and the development of novel geospatial interpolation methodologies that can incorporate both quantitative and censored data (Gill et al., 2016), provide an opportunity to create improved, proxy-based climate reconstructions for key deep time events by combining both approaches. In this study we leverage these advancements to improve the use of quantitative and censored paleoclimate proxies by compiling new paleoclimate proxy databases and then applying a novel analytical approach that employs Bayesian statistics to create global maps of continuous temperature and precipitation estimates from our compiled datasets. We use the resulting interpolated mean annual temperature (MAT), warmest mean monthly temperature (WMMT), and mean annual precipitation (MAP) maps to create paleo-Köppen climate zone maps for nine key time intervals across the Cretaceous following the methods of Zhang et al. (2016).

Köppen climate zone classifications rely on the combination of multiple climate parameters to define climate regimes and display the resulting climate zones spatially to highlight links between climates and ecosystems (Köppen, 1936). Updates and refinements to the original classification scheme and observational data have improved the spatial resolution and classification criteria (e.g., Trewartha, 1968; Peel et al., 2007; Beck et al., 2018), and allowed for more detailed applications like the evaluation of changing climate regimes in the modern era (e.g., Chen and Chen, 2013). Köppen maps have also become a regular component used in predictions and planning for current and future climate change, providing a crucial resource for protecting and adapting human infrastructure and agricultural systems (e.g., Quadrennial Defense Review Report (QDRR), 2010; Arias et al., 2021).

Developing these maps for the past provides a natural case study for understanding global climate change during warm periods like the Cretaceous. Historically, such paleoclimate maps have relied on censored lithologic or fossil climate indicators of a limited set of climate conditions, and have used subjective classification and delineation schemes to identify major zones and produce basic reconstructions. These climate indicators typically provide an upper or lower bound on climate parameters such as MAT, WMMT, or MAP. Some of the most common climate indicators include coals (warm/cool and wet), calcretes (warm/dry), tillites (cold), and glendonites (cold), and the temperature tolerance thresholds of key taxa (e.g., palms, crocodilians). Maps created using such methods are limited to broad environmental assignments like ‘paratropical’ or ‘arid’ (e.g., Ziegler et al., 1985; Boucot et al., 2013).

While such qualitative maps are useful for describing some aspects of regional climate and major global environments in deep time, their limited temporal and spatial resolution (and relatively high uncertainty and/or subjectivity) leaves many important questions unanswerable. As an example, past paleoclimate maps of the Cretaceous typically featured just two (Early and Late) or at most three (Early, middle, and Late) time slices, resulting in analysis windows with an average time span of ~40 or ~ 26 million years, respectively (e.g., Parrish et al., 1982; Boucot et al., 2013). These large analysis windows mask shorter-term global climate changes that have been documented for the Cretaceous, such as the brief Barremian/Aptian cooling interval (Price et al., 2000; Masse and Fenerci-Masse, 2008). In contrast, the nine new Cretaceous paleo-Köppen presented in this study yield detailed, quantitative reconstructions of temporal and spatial climate change across the Cretaceous with associated uncertainties, shed new light on long-standing questions regarding the behavior of earth's climate system during greenhouse periods, and provide a quantitative foundation for comparing model and proxy paleoclimate reconstructions.

2. Analysis framework and methods

In the following sections we detail our analytical framework, data sources, and the data processing steps that we employed in our study. The entire analytical process is presented as a schematic graphic in Fig. S1.

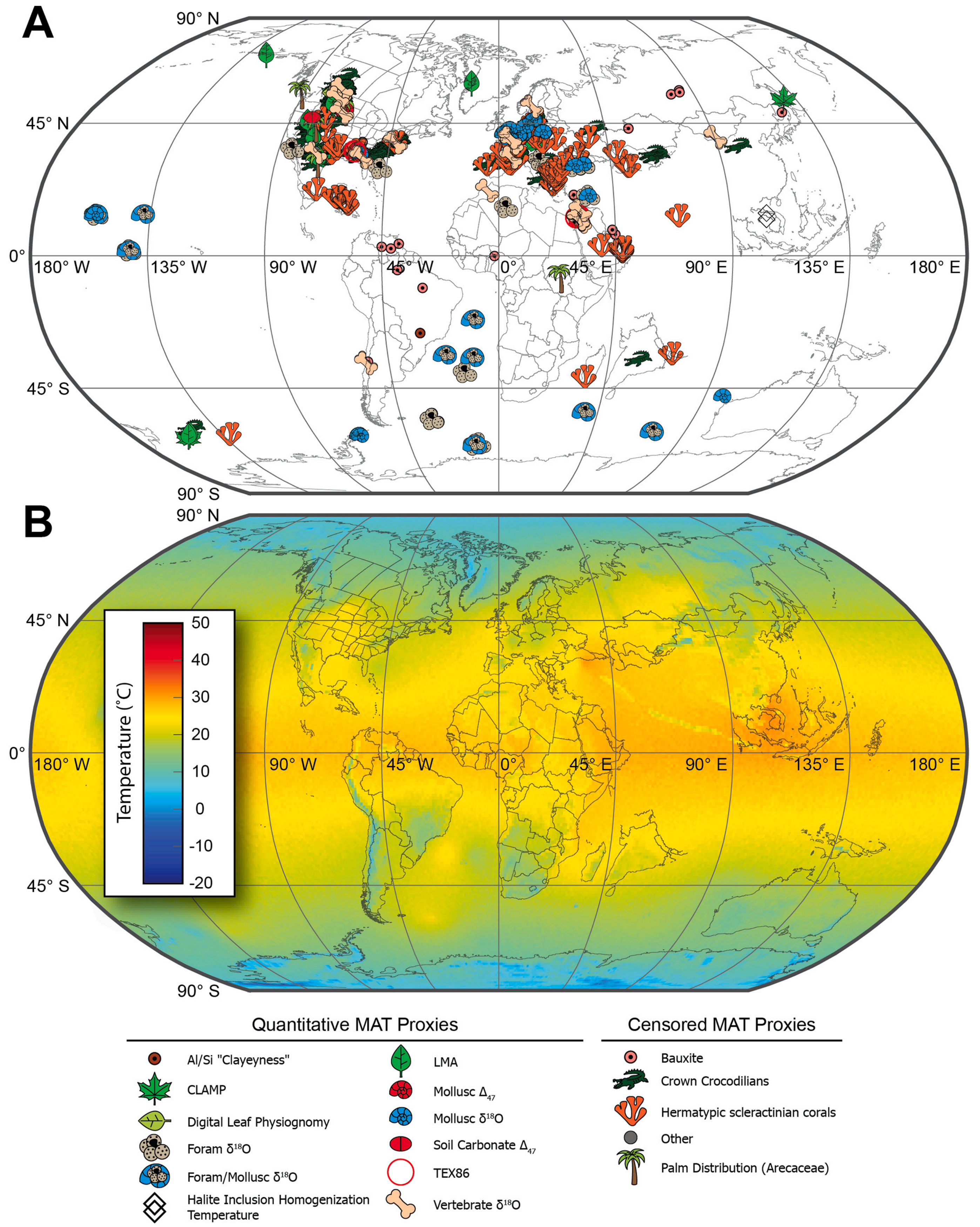

Fig. 1. Global map of Campanian (83.6–72.1 Ma) mean annual temperature data points (A), and the resulting interpolated mean annual temperature map (B).

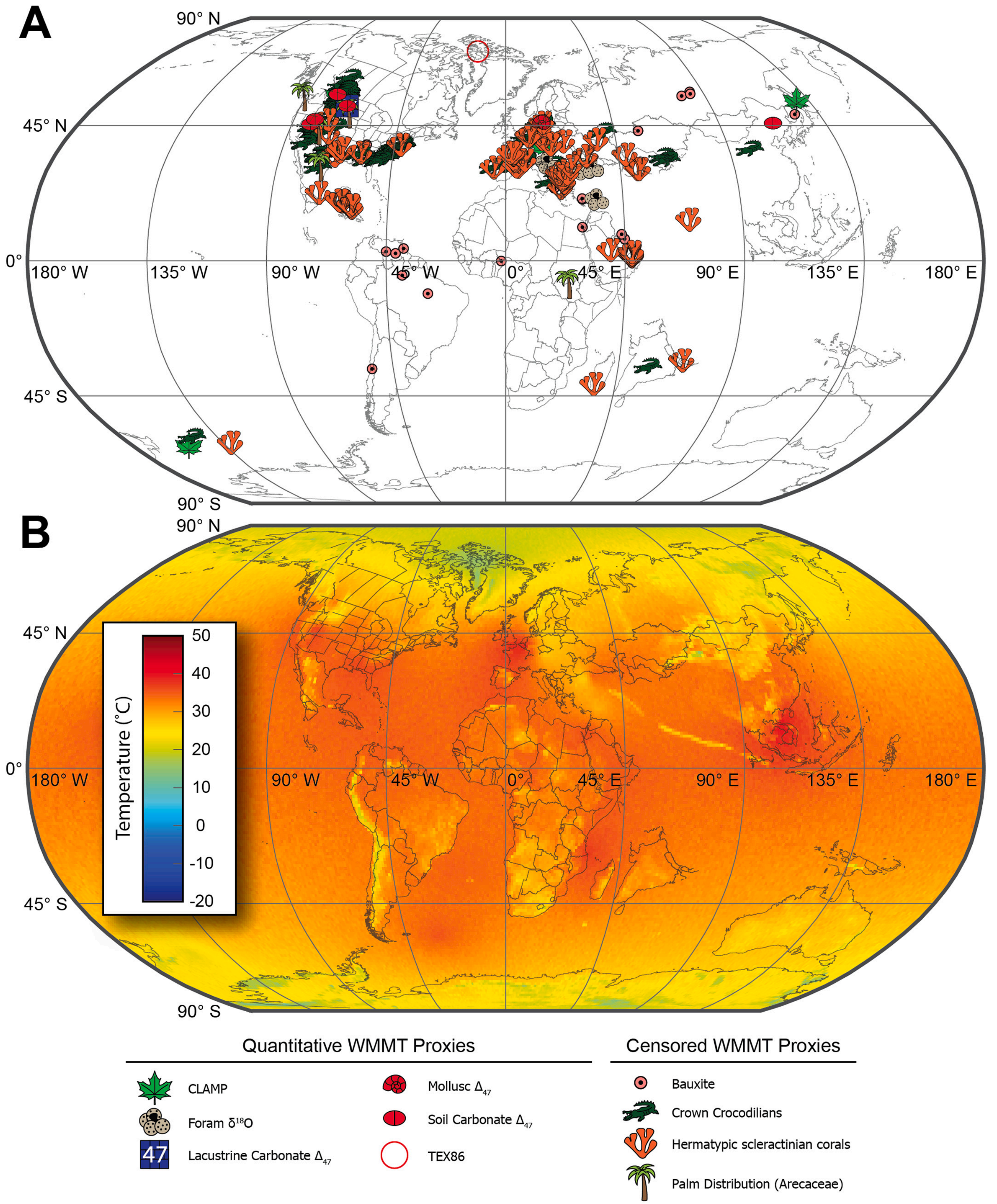

Fig. 2. Global map of Campanian (83.6–72.1 Ma) warmest mean monthly temperature data points (A), and the resulting interpolated warmest mean monthly temperature map (B). See Figure SI11 for symbol legend.

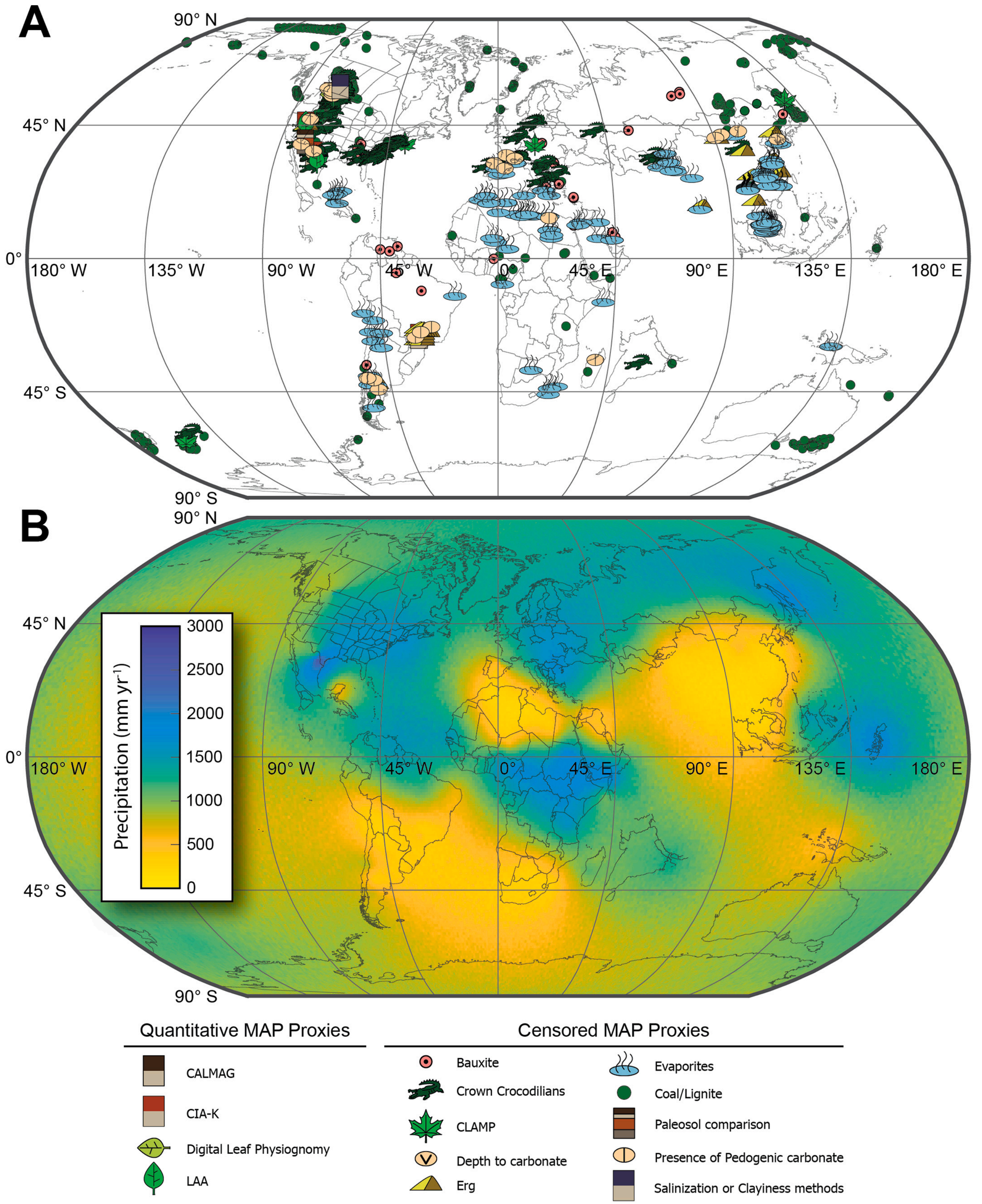

Fig. 3. Global map of Campanian (83.6–72.1 Ma) mean annual precipitation and coal/lignite data points (A), and the resulting interpolated mean annual precipitation map (B). See Figure SI20 for symbol legend.

2.1. New data compilations

Building on recent data compilations for the Cretaceous (e.g., Tabor et al., 2016; Burgener et al., 2021), we have compiled >4500 MAT, >1600 WMMT observations, >2000 MAP observations, and > 2200 coal and lignite observations from >4200 distinct localities (Table 1 and Tables SI1-SI4) throughout the Cretaceous. Evaluated data included terrestrial and marine observations from 1) previous compilations (e.g., Tabor et al., 2016; Burgener et al., 2021), 2) new observations using novel proxy methods, and 3) updated quantitative or threshold-based paleoclimate proxies. Tables SI5-SI10 provide a complete list of the temperature and precipitation proxies used in this study, as well as their associated temperature and/or precipitation constraints. Paleoclimate reconstructions for which a season (e.g., mean annual precipitation or warmest mean monthly temperature) was not identifiable were excluded from the compilations. As detailed below (*Section 3.4*), the climate constraints provided by some lithologic and fossil indicators were updated from previous studies based on new modern climate comparisons performed in this study. Paleolatitude and Paleolongitude for each sample was reconstructed using the PALEOMAP Global Plate Model (Scotese, 2016) and the GPlates program (Müller et al., 2018).

Mean annual temperature was estimated using 40 unique quantitative and semi-quantitative proxies which are summarized in Tables SI5-SI8. In the case of geochemical data, quantitative estimates of temperature were obtained directly from the climate proxy (e.g. δ^{18}O). In other cases, a range of probable temperatures were associated with the geological or paleontological climate proxies (Tables SI6 and SI8). These “censored” data provided useful, but less precise, temperature information. Fig. 1 illustrates the relationship between this information and the derived global estimate of MAT for the Campanian. A more detailed discussion of our methodology and the temperature range associated with these proxy data is given in Sections 2.3–2.4 and Tables SI5-SI8.

Warmest mean monthly temperature was estimated using 23 unique quantitative and semi-quantitative proxies which are summarized in Tables SI5-SI8. Fig. 2 illustrates the relationship between this information and the derived global estimate of WMMT for the Campanian. A more detailed discussion of our methodology and the maximum temperature range associated with these proxy data is given in Section 2.3–2.4 and Tables SI5-SI8.

Mean annual precipitation was estimated using 19 unique quantitative and semi-quantitative proxies which are summarized in Tables SI7-SI10. Fig. 3 illustrates the relationship between this information and the derived global estimate of MAP for the Campanian. A more detailed discussion of our methodology and the range of precipitation values associated with these proxy data is given in Section 2.3–2.4 and Tables SI7-SI10.

2.2. Sample ages and age weights

Data were sorted by age into 9 bins (Berriasian/Valanginian, Hauterivian/ Barremian, Aptian, Albian, Cenomanian, Turonian, Coniacian/ Santonian, Campanian, Maastrichtian) (Figures SI2–37, Table 1). Samples with quantitative age estimates were assigned to a given bin based on their associated maximum and minimum age estimates. If the associated age range overlapped two or more bins, the sample was included in each bin. For example, the boundary between the Aptian and Albian stages is dated to 113.2 Ma (Gradstein et al., 2020). A sample with a maximum age of 115 Ma and a minimum age of 105 Ma would thus be included in both the Aptian and Albian analysis bins. Most of the compiled samples have not been quantitatively dated, and are instead associated with a specific stage(s) or sub-stage(s) (e.g., “Barremian”, “Aptian-Albian”, or “early Maastrichtian”). These samples were assigned quantitative ages based on the ages of the upper and lower stage (or sub-stage) boundaries (Gradstein et al., 2020).

For the geospatial analysis, samples were weighted based on the degree of confidence in their quantitative or qualitative ages. Weights were calculated using the following formula:

$$W = \frac{1}{n} \tag{1}$$

where W is the calculated age weight and n is the number of analysis bins to which the sample is assigned. For example, if a sample had a relatively large associated age range and was included in three analysis bins (e.g., Albian, Cenomanian, and Turonian), n would equal 3, and the corresponding age weight W would be 0.33. The age weights for our compiled datasets range from 1 to 0.11. For our MAT, WMMT, MAP and coal datasets 80%, 52%, 30%, and 55% of the samples, respectively, have age weights of 1.

2.3. New and revised quantitative paleoclimate proxies

Novel quantitative terrestrial climate proxies have been introduced, improved, and/or expanded in recent years, providing more accurate estimates of MAT and MAP as well as additional parameters like temperature and precipitation seasonality. Examples of such quantitative proxies include carbonate clumped isotope paleothermometry (e.g., Eiler, 2011), phyllosilicate crystallization temperature (e.g., Andrezejewski, 2018), paleosol geochemistry (e.g., Sheldon and Tabor, 2009; Hyland et al., 2015; Hyland and Sheldon, 2016), leaf physiognomy (e.g., Spicer et al., 2009; Peppe et al., 2011), and organic lipid-based paleothermometers like TEX_{86} (e.g., Tierney and Tingley, 2014; Polik et al., 2018). Each of these proxies formed in unique environmental and depositional settings and have important limitations and caveats when interpreting their results. Those proxies that required special treatment in our study are discussed below.

2.3.1. Biogenic $\delta^{18}O$ temperatures

A large body of research exists regarding the best practices and methodologies associated with paleotemperature estimates from biogenic (e.g., foraminifera, mollusks, gastropods, etc.) δ^{18}O values. The oxygen isotope composition of calcium carbonate shells is determined by both the δ^{18}O value of the water the shell forms in, and the temperature of formation (e.g., Emiliani, 1954; Erez and Luz, 1983). For the purposes of our study, we have used the original paleotemperature estimates from compiled studies, except where those temperatures have been recalculated by later studies (e.g., Tabor et al., 2016). We recognize that this approach has the potential to introduce bias into our reconstructions (de Winter et al., 2021); however, we feel it is justified because our goal is to identify large-scale climate zones rather than study temporally or spatially small-scale climate changes.

For those studies that reported foraminifera δ^{18}O values but did not calculate formation temperatures, we estimated paleotemperatures using the δ^{18}O-T calibration of Erez and Luz (1983) as described by Tabor et al. (2016):

$$T = 16.998 - 4.52\left(\delta^{18}Oc - \delta^{18}Ow\right) + 0.028\left(\delta^{18}Oc - \delta^{18}Ow\right)^2 \tag{2}$$

where T is the carbonate formation temperature in °C, and $\delta^{18}O_c$ and $\delta^{18}O_w$ are the oxygen isotope composition of the carbonate shell and formation water, respectively. We chose to use the Erez and Luz (1983) δ^{18}O-temperature calibration becauseit was developed specifically for use with planktonic foraminifera. Benthic foraminifera, which act as a record of deep ocean conditions, were excluded from our study.

For studies that reported gastropod and/or mollusk δ^{18}O values but did not calculate formation temperatures, we estimated paleotemperatures using the Anderson and Arthur (1983) δ^{18}O-T calibration per Tabor et al. (2016):

$$T = 16.4 - 4.14\left(\delta^{18}Oc - \delta^{18}Ow\right) + 0.13\left(\delta^{18}Oc - \delta^{18}Ow\right)^2 \tag{3}$$

We used the Anderson and Arthur (1983) calibration because of its use in previous paleotemperature reconstruction studies that made use of mollusk and gastropod δ^{18}O values (e.g. Pirrie et al., 1995, 2004; Voigt et al., 2003; Hall and Tracy, 2005; Zakharov et al., 2005, 2006; El-Shazly et al., 2011; Price et al., 2012; Tabor et al., 2016; Walliser and Schöne, 2020).

Regardless of the δ^{18}O-T calibration employed, we assumed a uniform seawater δ^{18}O value of −1 ‰ VSMOW for the paleotemperatures calculated in this study (Kennett and Shackleton, 1975).

2.3.2. CLAMP precipitation estimates

The Climate Leaf Analysis Multivariate Program (CLAMP) is a multivariate leaf physiognomy-based paleoclimate proxy that provides estimates of multiple parameters including coldest mean monthly temperature, MAT, WMMT, and mean growing season precipitation (Spicer et al., 2009; Spicer et al., 2021). Because mean growing season precipitation is less than total MAP (Spicer et al., 2021), we treat it as a censored sample in our analysis, representing a lower limit on MAP.

2.3.3. TEX_{86} paleotemperature estimates

The TetraEther indeX of 86 carbon atoms (TEX_{86}) paleotemperature proxy is a relatively new method for reconstructing marine temperatures from the relative distribution of glycerol dibihytanyl glycerol tetraether lipids (Schouten et al., 2007). Two issues complicated the use of TEX_{86} temperatures in this study. First, lipid production tends to be seasonal, with the result that TEX_{86} temperatures are representative of growing season rather than mean annual sea surface temperatures (Sluijs et al., 2006; Bijl et al., 2009; Hollis et al., 2012; and Ho et al., 2014). At lower latitudes, this seasonal bias is relatively small, but at high latitudes the difference between growing season and mean annual temperatures can become quite large due to the curtailed growing season (Bijl et al., 2009, supplementary information). To account for this, we classified any TEX_{86} samples below paleolatitudes 65° N/S as MATs, and samples poleward of 65° N/S as WMMTs following Sluijs et al. (2006), Bijl et al. (2009), and Hollis et al. (2019). We note that the issue of TEX_{86} seasonality is an area of ongoing research (Ho et al., 2014; Tierney and Tingley, 2014) and that future findings may necessitate updates to this treatment of the TEX_{86} data. Second, TEX_{86} paleotemperature estimates are often significantly warmer than estimates from other proxies (e.g., Tierney and Tingley, 2015). This is caused both by non-temperature factors that influence lipid distributions, such as influx of terrestrial lipids via rivers, and by the fact that Cretaceous TEX_{86} values are often higher than maximum values from modern core-top datasets (O'Brien et al., 2017). To account for this, we excluded any temperature estimates from the $TEX_{86\text{-Linear}}$ calibration from our datasets, due to the large offset between this calibration and δ^{18}O marine paleotemperature estimates (see O'Brien et al., 2017 for extended discussion of this issue). Additionally, we included a flag in our statistical analysis (see *Section 3.7* for a detailed explanation) to estimate the bias in $TEX_{86\text{-Linear}}$ temperature reconstructions relative to other proxies.

2.4. Previous and new climate constraints from lithologic and fossil indicators

2.4.1. Coal and lignite constraints on MAP lower limits

Coals and lignites are often associated with warm, wet environments; however, modern peat deposits are found in a wide variety of environments with high water tables (Markwick, 2007). Markwick (2007) summarizes the challenges associated with relating the occurrence of coal and lignite to specific precipitation or temperature conditions; to avoid these issues, we opt to treat the Cretaceous coal and lignite samples as censored data that, when paired with reconstructed MAT estimates, provide a lower limit on local MAP values. Modern peat localities were taken from Xu et al. (2018), and MAT and MAP values were taken from the CHELSA temperature and precipitation climatologies (Karger et al., 2017; Repository: Karger et al., 2018).

To relate MAP to MAT at modern peat localities, we performed three experiments. Modern peat samples were grouped into 1 °C (Fig. SI38A), 2 °C (Fig. SI38B), and 5 °C (Fig. SI39C) MAT bins based on mean MAT values calculated in a 1° × 1° area around each sample site, after which the lower 5% and 10% quantiles were calculated for each MAT bin. Cubic polynomial regressions were then fit to the resulting data. The results of these calculations show that from MAT values of −10 °C to 4 °C, the lower limit of peat locality MAPs increases from <200 mm yr^{-1} to 350–400 mm yr^{-1}. Between MAT values of 4 °C and 14 °C, MAP lower limits decrease to nearly 0 mm yr^{-1}, after which MAP lower limits increase as MAT increases, to a maximum of ~1700 mm yr^{-1} at 27 °C. Most of the extremely low MAP lower limits found between MAT values of 4 °C and 14 °C are associated with irrigated agricultural areas in extremely arid and continental regions of central Eurasia. For this reason, we favor the following 10% quantile regression, which minimizes the extremely low MAP lower limits:

$$MAP_{LL} = 0.1081 \times MAT^3 - 0.8647 \times MAT^2 - 2.1039 \times MAT + 331.5 \tag{4}$$

where MAP_{LL} is the mean annual precipitation lower limit and MAT is the mean annual temperature at the coal or peat locality.

2.4.2. Other fossil indicators

In addition to the development of new quantitative climate proxies, previous qualitative climate indicators such as palms (e.g., Reichgelt et al., 2018) and laterites (e.g., Thorne et al., 2012), have seen significant increases to their precision and accuracy. Tables SI5-SI10 list the temperature and precipitation constraints associated with the different lithologic and fossil climate indicators. We developed new or updated seasonal constraints for many of these indicators (Table SI11) by relating their previously established MAT or coldest mean monthly temperature (CMMT) limits to the 1st or 99th percentile of previously unconstrained seasonal temperatures (e.g., MAT or WMMT; Fig. SI39) using the Global Historical Climatology Network (GHCN; Menne et al., 2018; Lawrimore et al., 2011), the CHELSA temperature and precipitation climatologies, the Global Land Ice Measurements from Space (GLIMS; Kargel et al., 2014) dataset, and National Oceanographic Data Center (NODC) World Ocean Atlas 1998 sea surface temperatures provided by the NOAA PSL (Boulder, Colorado, USA; https://psl.noaa.gov/). For many of the censored paleotemperature indicators, only a single seasonal temperature constraint was calculated by earlier studies. For example, Rogov et al. (2021) calculated a CMMT range of −1.9 to 7 °C for the formation of ikaite (altered to glendonite in sedimentary records) in Arctic seawater. Using the NODC sea surface temperature dataset, for modern areas with a CMMT range of −1.9 to 7 °C, the corresponding lower limits (1st percentile) on MAT and WMMT are −1.6 and − 1.3 °C (Fig. SI39E). For left-censored paleotemperature indicators (e.g., CMMT ≥5 °C), we assumed that at any given latitude, temperatures in the corresponding warmer seasons (in this case, both MAT and WMMT) would be higher during the Cretaceous than for modern sites with the same temperature limit. In such cases, modern temperature data should provide a reasonable *lower limit* on potential Cretaceous temperatures. In contrast, we did not calculate colder season temperature upper limits for right-censored paleotemperature indicators (e.g., WMMT ≤25 °C), because modern temperatures at any given latitude are likely to be colder than Cretaceous conditions at the same latitude.

For all of the censored data, reasonable maximum or minimum values were chosen for the non-truncated tail of each distribution. In some cases, the choice of a reasonable limit was simple; for example, the lower limit on censored MAP proxies was set at 0 mm yr^{-1}. For more ambiguous parameters like MAT and WMMT, reasonable upper or lower limits were chosen based on Cretaceous climate model results (Table SI12; Poulsen et al., 2007; Sewall and Fricke, 2013; Ladant and Donnadieu, 2016; Niezgodzki et al., 2017). Based on these models, minimum and maximum MAT and WMMT limits were set at −15 and 40 °C and 0 and 50 °C, respectively.

2.5. New geography and DEMs

Here we use updated paleogeographies (e.g., Müller et al., 2018) and paleocoastline and paleo-digital elevation model (DEM) reconstructions of the continents (e.g., Scotese and Wright, 2018) as a base for our analyses. The paleo-DEMs were constructed by first identifying the general depositional environment for a given site based on the observed lithologies at that location (see Scotese and Wright (2018) for additional detail). These initial lithofacies maps were constructed using lithologic datasets developed by Ziegler et al. (1985) and Rees et al. (2000, 2002). After creating the lithofacies maps for a given time period (e.g., the Turonian), paleo-elevations can be calculated based on the modern relationship between a given lithology and modern elevation. See Scotese and Wright (2018) for a complete discussion of these methods.

2.6. Spatial interpolation

Compiled data are analyzed using geostatistical methods where we assume the mean annual temperature, seasonal temperature, and precipitation variables follow Gaussian spatial processes with means that depend on polynomial functions of latitude and have exponential spatial covariance and a nugget variance. To accommodate interval censoring, we use Bayesian hierarchical models with a censored likelihood. The Markov Chain Monte Carlo algorithm produces estimates (and measure of uncertainty) on a 1° x 1° global grid. Estimated temperature and precipitation fields are then converted to zonal climate classifications using the Paleo-Köppen climate classification system.

Two MAT and WMMT interpolation analyses were performed for each analysis window. The first analysis was conducted using only the raw MAT or WMMT data. The second analysis took into account the elevation information provided by the paleo-DEMs, and applied a mean temperature-elevation lapse rate to model the effect of increased elevation for unsampled areas. The temperature-elevation lapse rate was assumed to be -5 ± 1 °C km^{-1} based on modelling studies of Eocene temperature-elevation lapse rates (Feng and Poulsen, 2016; Dutra et al., 2020). The elevation-adjusted temperature results and associated paleo-Köppen reconstructions will be referred to as MAT_{elev}, $\text{WMMT}_{\text{elev}}$, and paleo-$\text{Köppen}_{\text{elev}}$ hereafter.

For the MAT and WMMT analyses, the general spatial model is defined by its mean and covariance functions. The most general mean function is:

$$T = \beta_0 + (|latitude| \times \beta_1) + \left(|latitude|^2 \times \beta_2\right) + (elevation \times \beta_3) + TEX86 \times \beta_4 \tag{5}$$

where T is MAT or WMMT, βi are the coefficients for each parameter, *latitude* is the sample's paleolatitude, *elevation* is the sample's reconstructed paleoelevation, and *TEX86* is a binary variable that equals 1 if the observation is from the TEX_{86} proxy and 0 otherwise. For the model fit without elevation, β_3 is set to 0. The coefficient β_4 quantifies the bias of TEX_{86} temperature reconstructions compared to other proxy reconstructions.

Temperature (MAT or WMMT) has variance $\sigma^2 + \tau^2$ and the covariance between temperature at two locations separated by distance d is $\sigma^2 \times e^{-d/p}$. The covariance thus decays exponentially with decay rate ρ so that temperature for nearby sites are more correlated than distant sites. The two variances are the spatial variance σ^2 and the error, or nugget, variance τ^2. For a review of spatial/geostatistical modelling see Cressie and Wikle (2011).

The two earliest analysis windows (Berriasian-Valanginian and Hauterivian-Barremian) had fewer MAT and WMMT reconstructions and a more spatially restricted distribution of data points than the other Cretaceous analysis windows. Due to this relative scarcity of data, we imposed two additional prior assumptions on our MAT and WMMT models for these two analysis windows. For WMMT, the longitudinal trends were fixed based on the MAT results and the relationship between WMMT and MAT in the current climate. Referring to Eq. (6), the latitudinal coefficients were fixed at $\beta_0 = \widehat{\beta}_0 - 0.4430$, $\beta_1 = \widehat{\beta}_1 + 0.2602$ and $\beta_2 = \widehat{\beta}_2 - 0.0004832$, where $\widehat{\beta}_j$ are the estimates for the era's MAT analysis and the constants are based on quadratic (in absolute latitude) regressions of MAT and WMMT in the current climate. In some cases, the constant for $\widehat{\beta}_1$ was adjusted to ensure a decreasing trend in absolute latitude.

Table 2

Paleo-Köppen climate zone descriptions and criteria (modified from Zhang et al., 2016).

Symbol		Major Climate		Criteria	
1st Order	2nd Order	1st Order	2nd Order	1st Order	2nd Order
A		Tropical		MAT ≥23 °C	
	Af/ Am		Tropical Rainforest		MAP ≥1800 mm yr^{-1}
	As/ Aw		Tropical Savannah		MAP <1800 mm yr^{-1}
B		Dry		$\text{AI}_{\text{köppen}} < 10.4$	
	BSh		Hot Steppe		$5.7 \leq \text{AI}_{\text{köppen}} < 10.4$, MAT ≥18 °C
	BSk		Cold Steppe		$5.7 \leq \text{AI}_{\text{köppen}} < 10.4$, MAT <18 °C
	BWh		Hot Desert		$\text{AI}_{\text{köppen}} < 5.7$, MAT ≥18 °C
	BWk		Cold Desert		$\text{AI}_{\text{köppen}} < 5.7$, MAT <18 °C
C		Temperate		9 ≤ MAT <23 °C	
	Ca		Humid Subtropical		WMMT ≥21 °C
	Cb		Maritime Temperate		15 ≤ WMMT <21 °C
	Cc		Maritime Subarctic		WMMT <15 °C
D		Continental		-10 ≤ MAT <9 °C	
	Da		Continental (Hot Summer)		WMMT ≥21 °C
	Db		Continental (Warm Summer)		15 ≤ WMMT <21 °C
	Dc/Dd		Continental Subarctic		WMMT <15 °C
E		Polar		MAT < −10 °C	

In contrast to the MAT and WMMT statistical models, which assumed a quadratic relationship between temperature and latitude, we made no prior assumption regarding the relationship between MAP and latitude (i.e., $T = \beta_0$).

2.7. Climate zone classifications

While modern Köppen climate classifications or thresholds are in many cases impractical or impossible to apply to deep time conditions, researchers have simplified and reorganized classifications for key boundaries delineating major climate zones. Here we use Zhang et al. (2016)'s guidelines to distinguish zones in these maps, modified to accommodate available proxy conditions in our compilation (Table 2). Unlike the traditional Köppen climate classification, which relies on monthly temperature and precipitation measurements in addition to MAT and MAP, the Zhang et al. (2016) paleo-Köppen climate classification system relies on only MAT, WMMT (optionally), and MAP, which are among the most commonly reconstructed paleoclimate parameters,

Table 3
Means and standard deviations of the interpolated non-elevation MAT and non-elevation WMMT maps.

Stage(s)	Mean MAT (°C)	Min Std. Dev. (°C)	Mean Std. Dev. (°C)	Max Std. Dev. (°C)	MAT Quantiles (°C)						Mean WMMT (°C)	Min Std. Dev. (°C)	Mean Std. Dev. (°C)	Max Std. Dev. (°C)	WMMT Quantiles (°C)					
					1%	5%	10%	90%	95%	99%					1%	5%	10%	90%	95%	99%
Berriasian-Valanginian	17.3	0.8	4.9	7.9	−2.7	3.2	6.4	28.3	31.1	35.8	28.8	1.7	6.6	8.6	9.9	15.2	18.3	39.0	41.7	46.2
Hauterivian-Barremian	13.0	0.7	2.9	4.8	−7.2	−2.4	0.6	25.5	27.7	31.2	24.0	2.9	6.3	8.3	3.4	8.2	11.2	36.2	39.1	44.1
Aptian	15.2	0.9	5.3	7.4	−5.9	−0.9	2.2	28.0	30.9	35.5	24.0	1.2	4.9	6.8	5.6	10.2	12.9	34.5	36.8	40.9
Albian	16.4	1.1	4.5	6.7	0.8	5.0	7.3	25.9	28.4	32.8	29.7	2.2	7.4	9.5	10.3	16.1	19.2	39.9	42.6	47.0
Cenomanian	18.9	0.6	4.8	7.2	2.0	6.7	9.2	29.6	32.3	36.5	27.7	0.9	4.4	6.2	14.3	18.0	19.9	36.2	38.6	42.7
Turonian	21.0	1.4	4.4	6.2	3.5	7.7	10.1	32.3	34.6	37.9	28.6	1.8	5.3	7.2	11.0	15.3	17.7	39.9	42.5	46.6
Coniacian-Santonian	19.7	0.6	4.2	6.3	3.5	7.7	9.9	29.9	32.3	36.3	27.2	0.4	4.0	5.7	11.9	15.7	17.6	37.3	39.8	44.5
Campanian	16.2	0.9	4.9	7.5	−3.1	2.1	5.0	27.2	29.7	34.0	27.4	0.9	5.5	8.1	9.6	14.5	17.2	37.2	39.6	43.9
Maastrichtian	14.2	0.7	4.2	6.6	−3.2	1.1	3.6	24.7	27.3	31.5	23.3	0.8	4.0	5.9	8.0	12.0	14.3	32.3	34.2	37.7

Table 4
Means and standard deviations of the interpolated MAT_{elev} and $WMMT_{elev}$ maps.

Stage(s)	Mean MAT (°C)	Min Std. Dev. (°C)	Mean Std. Dev. (°C)	Max Std. Dev. (°C)	MAT Quantiles (°C)						Mean WMMT (°C)	Min Std. Dev. (°C)	Mean Std. Dev. (°C)	Max Std. Dev. (°C)	WMMT Quantiles (°C)					
					1%	5%	10%	90%	95%	99%					1%	5%	10%	90%	95%	99%
Berriasian-Valanginian	17.4	1.0	5.6	8.8	−3.8	2.2	5.5	29.5	32.6	37.2	28.6	1.6	6.7	8.8	8.9	14.4	17.6	39.4	42.2	46.7
Hauterivian-Barremian	12.6	0.9	3.6	5.5	−7.2	−2.6	0.2	25.7	28.3	32.4	23.8	2.8	6.4	8.4	3.6	8.4	11.4	35.9	38.8	44.0
Aptian	14.3	1.0	5.4	7.5	−6.8	−2.0	1.1	27.6	30.6	35.3	22.8	1.1	5.0	6.9	4.2	8.7	11.4	33.7	36.3	40.6
Albian	15.4	1.1	4.3	6.5	−0.8	3.6	6.0	25.4	28.0	32.4	28.3	2.1	7.5	10.1	8.4	14.2	17.4	39.0	41.8	46.6
Cenomanian	17.8	0.7	4.7	7.2	1.2	5.7	8.2	28.4	31.3	35.7	26.6	0.9	4.3	6.1	13.0	16.7	18.8	34.9	37.2	41.1
Turonian	19.3	1.5	4.5	6.5	0.5	5.1	7.7	31.5	34.0	37.7	26.9	1.9	5.1	7.2	9.0	13.4	15.9	38.5	41.2	45.5
Coniacian-Santonian	18.6	0.6	4.2	6.2	1.3	6.0	8.5	29.2	31.7	35.9	26.1	0.5	4.0	5.5	10.3	14.5	16.6	36.2	38.7	43.5
Campanian	14.6	0.8	4.9	7.0	−5.6	−0.4	2.6	26.4	29.0	33.5	26.4	0.9	5.8	8.3	8.1	13.4	16.3	36.1	38.5	42.9
Maastrichtian	13.4	0.6	4.3	6.6	−4.1	0.4	2.8	24.0	26.6	31.1	22.3	0.8	3.9	6.1	6.7	10.8	13.0	31.9	34.0	37.5

Table 5
Means and standard deviations of the interpolated MAP maps.

Stage(s)	Mean MAP (mm yr^{-1})	Min Std. Dev. (mm yr^{-1})	Mean Std. Dev. (mm yr^{-1})	Max Std. Dev. (mm yr^{-1})	MAP Quantiles (mm yr^{-1})					
					1%	5%	10%	90%	95%	99%
Berriasian-Valanginian	1048.4	77.5	423.6	677.9	50.6	198.7	332.4	1787.8	2016.9	2457.2
Hauterivian-Barremian	830.7	43.9	266.1	469.3	85.3	240.1	351.7	1314.7	1475.1	1803.2
Aptian	989.3	85.8	326.7	551.1	65.2	221.0	346.7	1650.9	1871.4	2381.9
Albian	1093.3	66.6	356.8	562.2	66.5	236.2	378.2	1819.4	2015.3	2373.9
Cenomanian	1324.2	115.9	527.1	777.1	60.9	246.4	420.7	2209.8	2464.3	2948.9
Turonian	1507.0	124.8	612.4	969.7	46.5	206.1	372.8	2717.8	3074.4	3732.6
Coniacian-Santonian	1307.2	113.5	478.9	715.7	47.8	200.3	349.9	2295.9	2563.6	3026.2
Campanian	1012.2	64.4	351.8	521.7	54.0	201.2	328.0	1686.0	1856.3	2160.6
Maastrichtian	1043.7	73.4	368.4	549.2	52.5	204.4	340.3	1715.1	1890.1	2216.1

Table 6
Average percent land area of the five Köppen Aridity Index categories.

Stage(s)	Aridity Category Mean Abundance (%)				
	Hyper-Arid	Arid	Semi-arid	Sub-humid	Humid
Berriasian-Valanginian	0	2.7	9.9	9.5	77.9
Hauterivian-Barremian	0	3.8	7.6	14.3	74.3
Aptian	0	2.4	8.7	12.4	76.5
Albian	0	0.6	7.8	9.3	82.3
Cenomanian	0	0.5	5.9	7.4	86.2
Turonian	0	0.6	7.2	9.0	83.1
Coniacian-Santonian	0	1.7	10.3	5.7	82.3
Campanian	0	2.4	11.4	6.0	80.1
Maastrichtian	0	0.7	9.9	6.9	82.6

and the Köppen aridity index, which is calculated as

$$AI_{Köppen} = \frac{MAP}{MAT + 33} \tag{6}$$

(Köppen, 1936). See Zhang et al. (2016) for a full discussion of the AI$_{Köppen}$ thresholds chosen to distinguish dry climate zones. As outlined in Fig. S1, AI$_{Köppen}$ means and standard deviations were calculated for each analysis window using the associated MAP and MAT distributions.

This paleo-Köppen climate classification system is readily applicable to most geographic areas and periods; however, it is not as detailed as the modern Köppen classification system, with just thirteen climate zones instead of the full 30 zones. Additionally, because the classification only makes use of annual average climate parameters and WMMT, it lacks seasonal precipitation information. However, it provides a robust, quantitative framework for classifying and comparing paleoclimate conditions spatially and temporally, and still delineates major climate zones (A, B, C, D, E) commonly used for proxy-model comparisons and decision-making predictions.

For each analysis window, paleo-Köppen zones were calculated at each grid cell 500 times by randomly sampling from the interpolated MAT, WMMT, and MAP distributions. From those 500 calculations, the most commonly identified paleo-Köppen zone was then selected as the final climate zone for each grid cell. A normal standard deviation does not provide meaningful information regarding the uncertainty associated with this distribution of paleo-Köppen values. Instead, we generated a confidence estimate associated with the final paleo-Köppen identification by calculating the percentage of the 500 iterations that yielded the final paleo-Köppen value.

3. Results

3.1. Interpolated temperature and precipitation precision and errors

One of the benefits of the approach outlined in this paper is the ability to estimate precision (Tables SI13-SI15) and uncertainties (Tables 3-6) associated with our interpolated MAT, WMMT, and MAP values. With respect to the quantitative, non-censored data, we employed a 5-fold cross validation approach to constrain the precision of our interpolated temperature and precipitation values at measured locations. As shown in Tables SI13-SI15, the resulting root-mean-square-error (RMSE) values for 1) MAT range from 1.9 °C (Aptian) to 4.0 °C (Hauterivian-Barremian); 2) WMMT range from 1.7 °C (Aptian) to 5.7 °C (Turonian); and 3) MAP range from 111.1 mm yr^{-1} (Hauterivian-Barremian) to 574.8 mm yr^{-1} (Campanian). Note that WMMT RMSE estimates were not calculated for the Berriasian-Valanginian and Hauterivian-Barremian because there are no quantitative WMMT samples for these analysis windows.

The precision of the estimated MAT, WMMT, and MAP values at censored data locations was more difficult to constrain because a conventional cross validation scheme could not be employed. Table SI14 shows the percent of the estimated data points that fall within the corresponding censored data interval for each analysis window. These percents range from 70% (Hauterivian-Barremian) to 96% (Turonian and Coniacian-Santonian) for the MAT data, 98% (Cenomanian) to 100% for the WMMT data, and 76% (Berriasian-Valanginian) to 89% (Aptian) for the MAP data. For those estimated values that fall outside the corresponding censored data interval (Table SI15), the MAT RMSE values range from 0.9 °C (Coniacian-Santonian) to 6.0 °C (Aptian), the WMMT RMSE values range from 1.1 °C (Turonian and Campanian) to 16.5 °C (Albian), and the MAP RMSE values range from 386.5 mm yr^{-1} (Maastrichtian) to1063.0 mm yr^{-1} (Turonian).

With regard to estimate uncertainties, when temperature-elevation lapse rates are ignored, mean MAT standard deviations range from 2.9 °C in the Hauterivian-Barremian to 4.9 °C in the Berriasian-Valanginian and Campanian, and mean WMMT standard deviations vary between 3.9 °C in the Coniacian-Santonian and Maastrichtian to 7.5 °C in the Albian. Mean MAP standard deviations range from 266.1 mm yr^{-1} in the Hauterivian-Barremian to 612.4 mm yr^{-1} in the Turonian (Tables 3-5).

3.2. Interpolated MAT, MAP and Köppen Aridity Index results

Tables 3-6 and Figures SI42 to SI77 summarize the temperature and precipitation statistics and results for the interpolated MAT, MAT$_{elev}$, WMMT, WMMT$_{elev}$, MAP, and Aridity maps from each of our nine Cretaceous time slices. For the analyses that did not consider elevation, interpolated mean global MATs decrease from 17 °C (also 17 °C when elevation is included) in the Berriasian-Valanginian to 13 °C (13 °C) in the Hauterivian-Barremian, then increase to a maximum of 21 °C (19 °C)

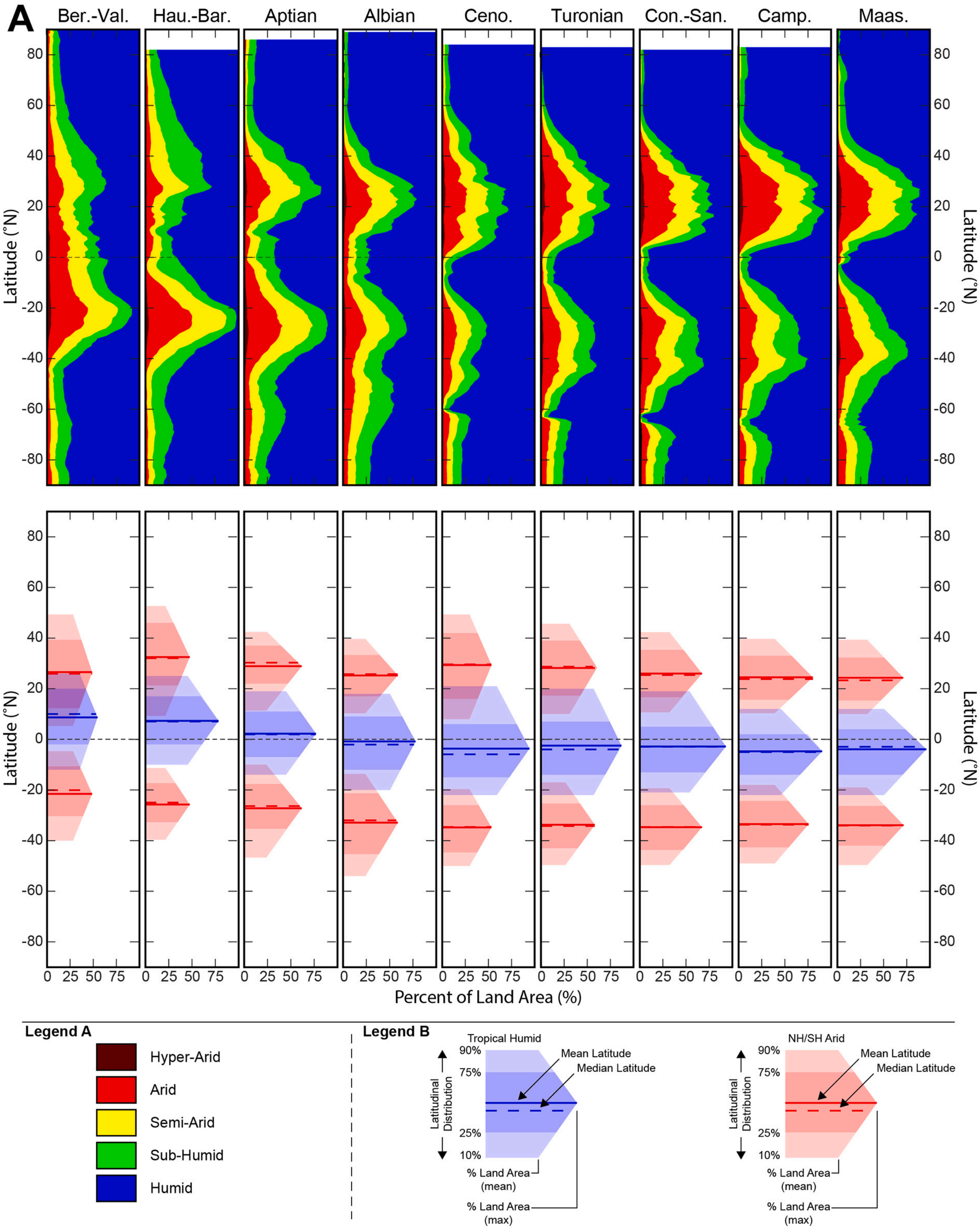

Fig. 4. Evolution of the strength and latitudinal extent of the Cretaceous equatorial humid belt and sub-tropical arid belts. A) Mean percent of land area in each of the nine analysis windows classified as Hyper-Arid, Arid, Semi-Arid, Sub-Humid and Humid using the Köppen Aridity Index. We consider a higher percent land area to represent a "stronger" humid or arid belt. B) The blue and red polygons provide a simplified visual of the equatorial humid and subtropical arid belts, respectively, with vertical width of the polygons showing the latitudinal extent of the belts, and the horizontal width showing the strength or magnitude of the belts. The solid and dashed lines show the mean and median position of each belt. Ber.-Val. = Berriasian-Valanginian, Hau.-Bar. = Hauterivian-Barremian, and Con.-San. = Coniacian-Santonian. (For interpretation of the references to colour in this figure legend, the reader is referred to the web version of this article.)

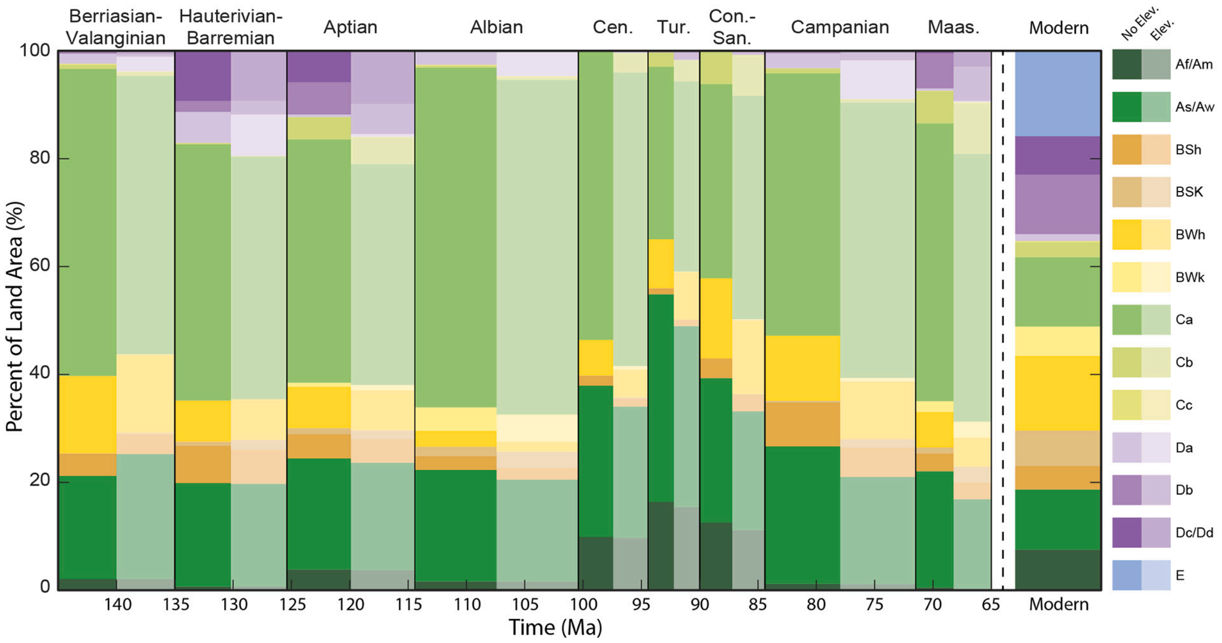

Fig. 5. The percent of land area occupied by each paleo-Köppen climate zone for all nine Cretaceous analysis windows and the modern climate system. For each analysis window, the bold colors on the left show the percentages for the non-elevation raw paleo-Köppen climate zones, while the pale colors on the right represent the percentages for the paleo-Köppen$_{elev}$ climate zones.

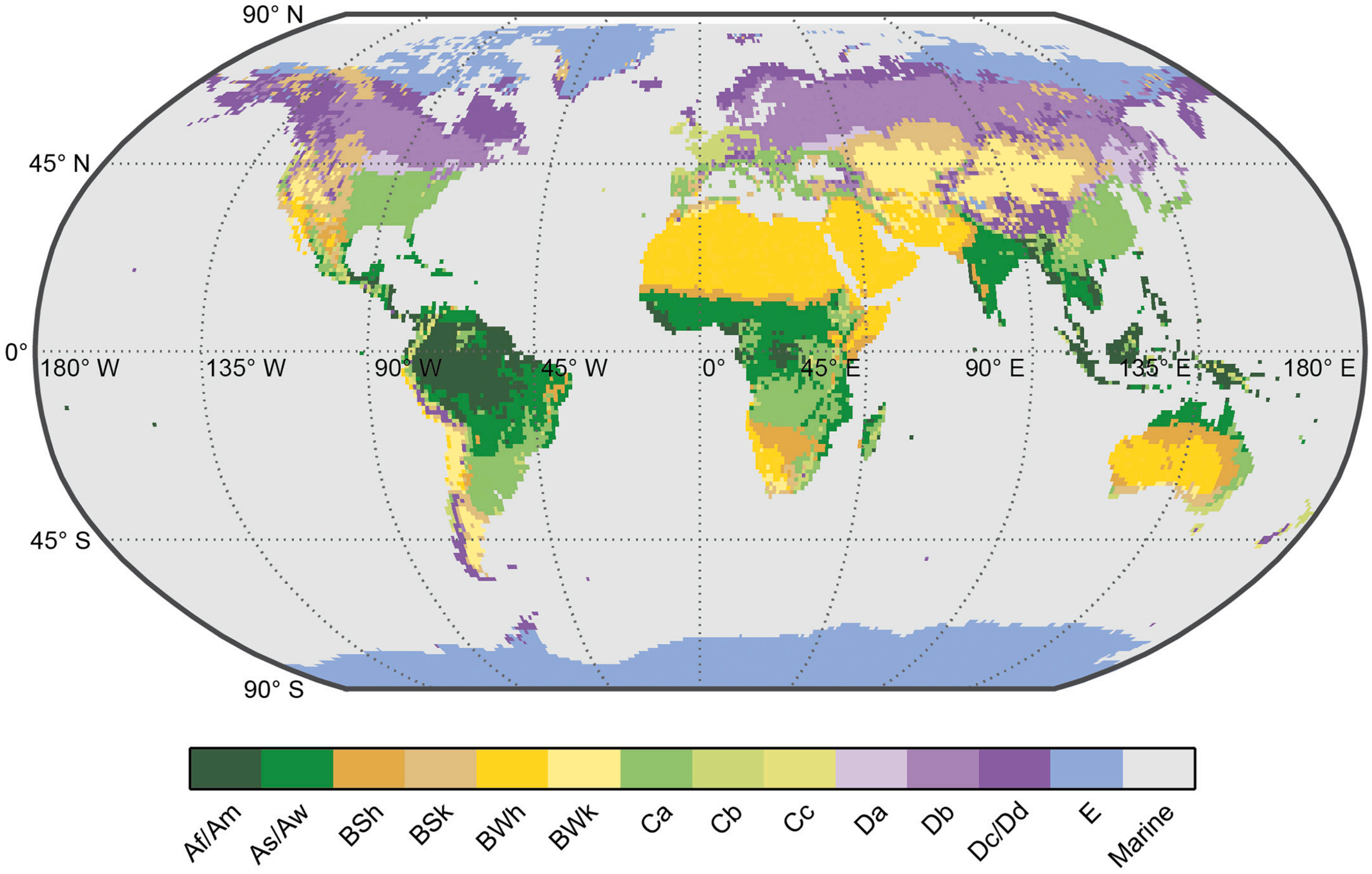

Fig. 6. Modern climate zones as defined by the paleo-Köppen climate classification system developed by Zhang et al. (2016). Af/Am = tropical rainforest, As/Aw = tropical savannah; BSh = hot steppe, BSk = cold steppe, BWh = hot desert, BWk = cold desert; Ca = temperate, humid subtropical, Cb = temperate, maritime temperate, Cc = temperate, maritime subarctic; Da = continental, hot summer, Db = continental, warm summer, Dc/Dd = continental, subarctic; E = polar. See Table 2 for a complete description of the climate zone classification criteria.

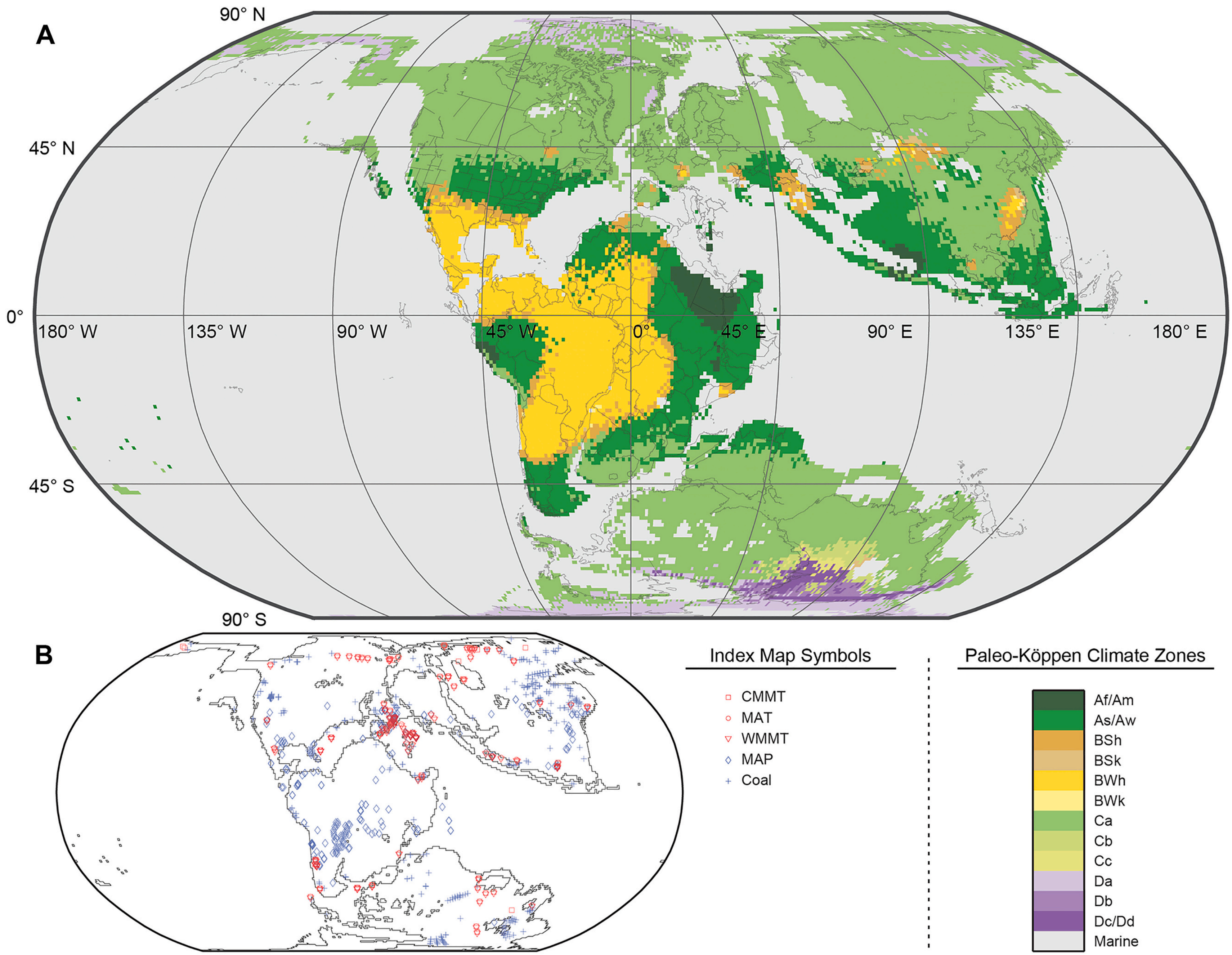

Fig. 7. Berriasian-Valanginian paleo-Köppen climate zones. Af/Am = tropical rainforest, As/Aw = tropical savannah; BSh = hot steppe, BSk = cold steppe, BWh = hot desert, BWk = cold desert; Ca = temperate, humid subtropical, Cb = temperate, maritime temperate, Cc = temperate, maritime subarctic; Da = continental, hot summer, Db = continental, warm summer, Dc/Dd = continental, subarctic; E = polar.

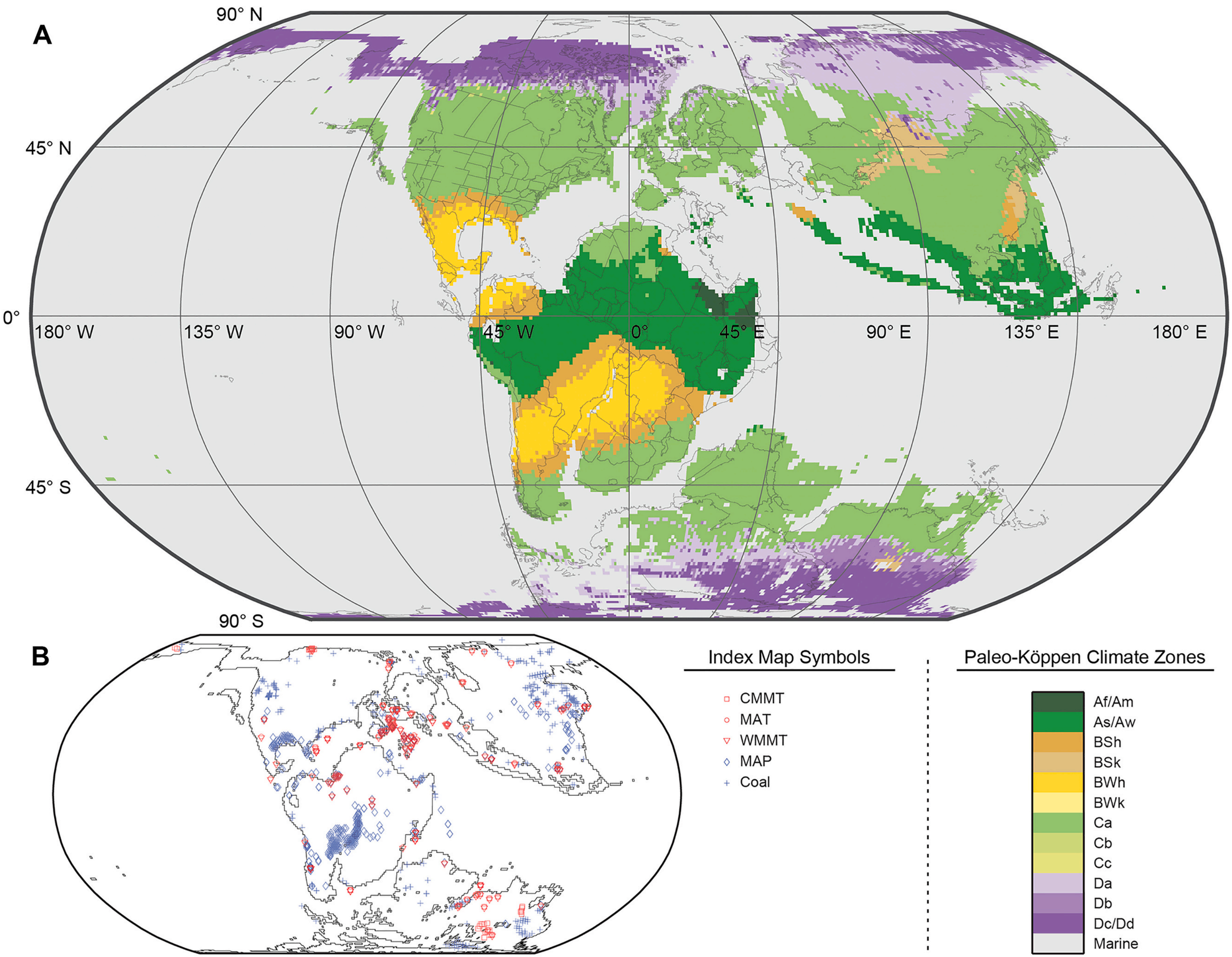

Fig. 8. Hauterivian-Barremian paleo-Köppen climate zones. Af/Am = tropical rainforest, As/Aw = tropical savannah; BSh = hot steppe, BSk = cold steppe, BWh = hot desert, BWk = cold desert; Ca = temperate, humid subtropical, Cb = temperate, maritime temperate, Cc = temperate, maritime subarctic; Da = continental, hot summer, Db = continental, warm summer, Dc/Dd = continental, subarctic; E = polar.

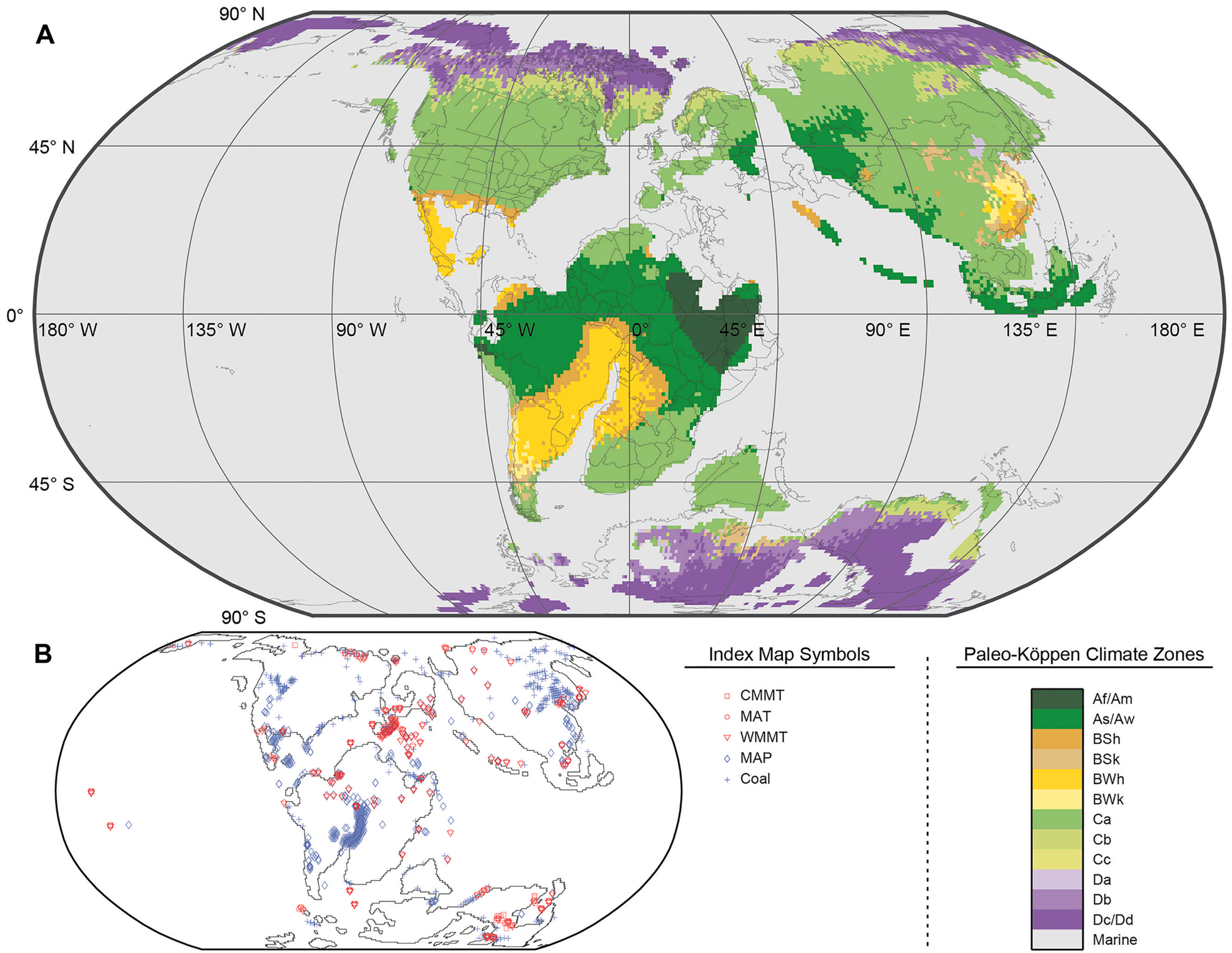

Fig. 9. Aptian paleo-Köppen climate zones. Af/Am = tropical rainforest, As/Aw = tropical savannah; BSh = hot steppe, BSk = cold steppe, BWh = hot desert, BWk = cold desert; Ca = temperate, humid subtropical, Cb = temperate, maritime temperate, Cc = temperate, maritime subarctic; Da = continental, hot summer, Db = continental, warm summer, Dc/Dd = continental, subarctic; E = polar.

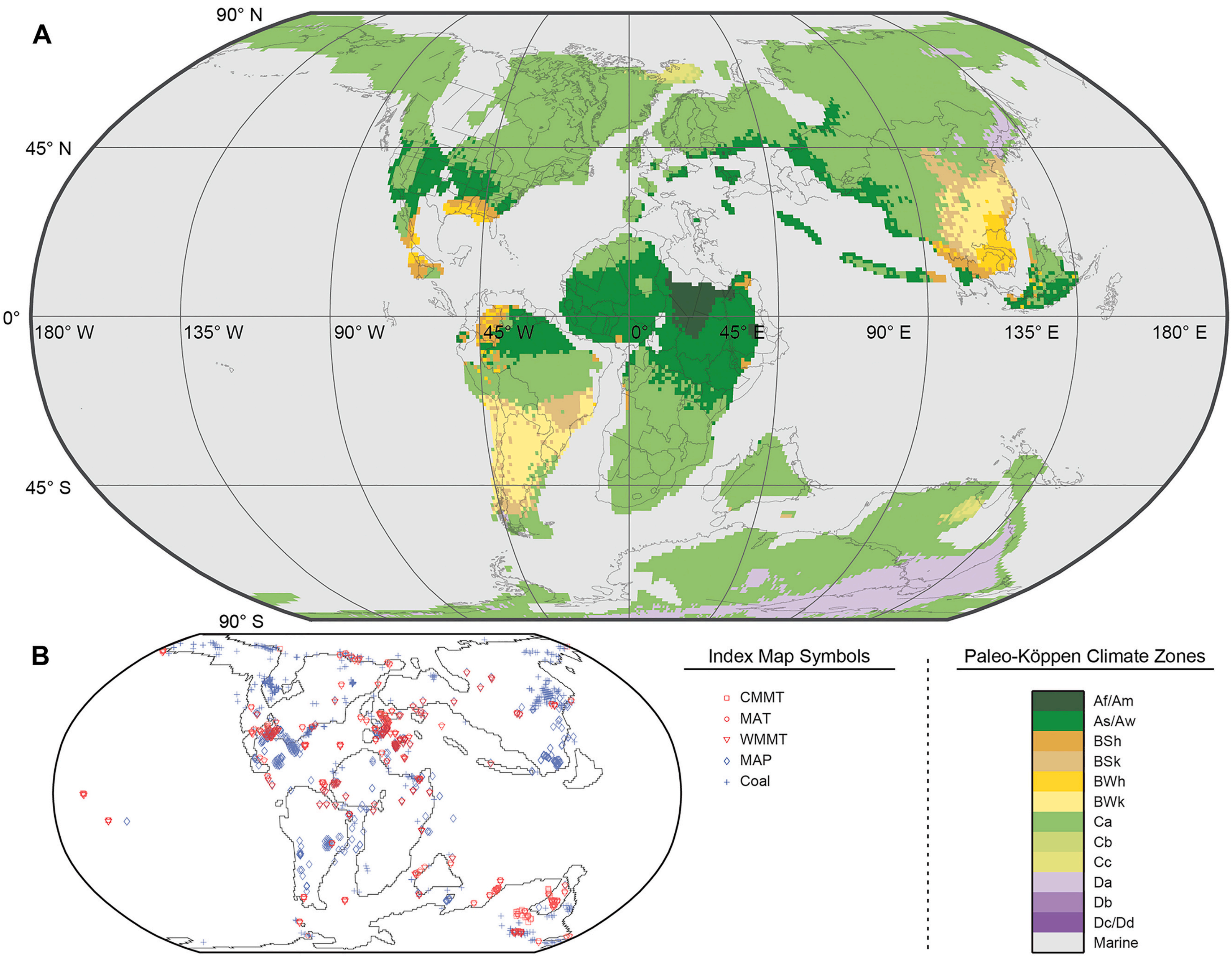

Fig. 10. Albian paleo-Köppen climate zones. Af/Am = tropical rainforest, As/Aw = tropical savannah; BSh = hot steppe, BSk = cold steppe, BWh = hot desert, BWk = cold desert; Ca = temperate, humid subtropical, Cb = temperate, maritime temperate, Cc = temperate, maritime subarctic; Da = continental, hot summer, Db = continental, warm summer, Dc/Dd = continental, subarctic; E = polar.

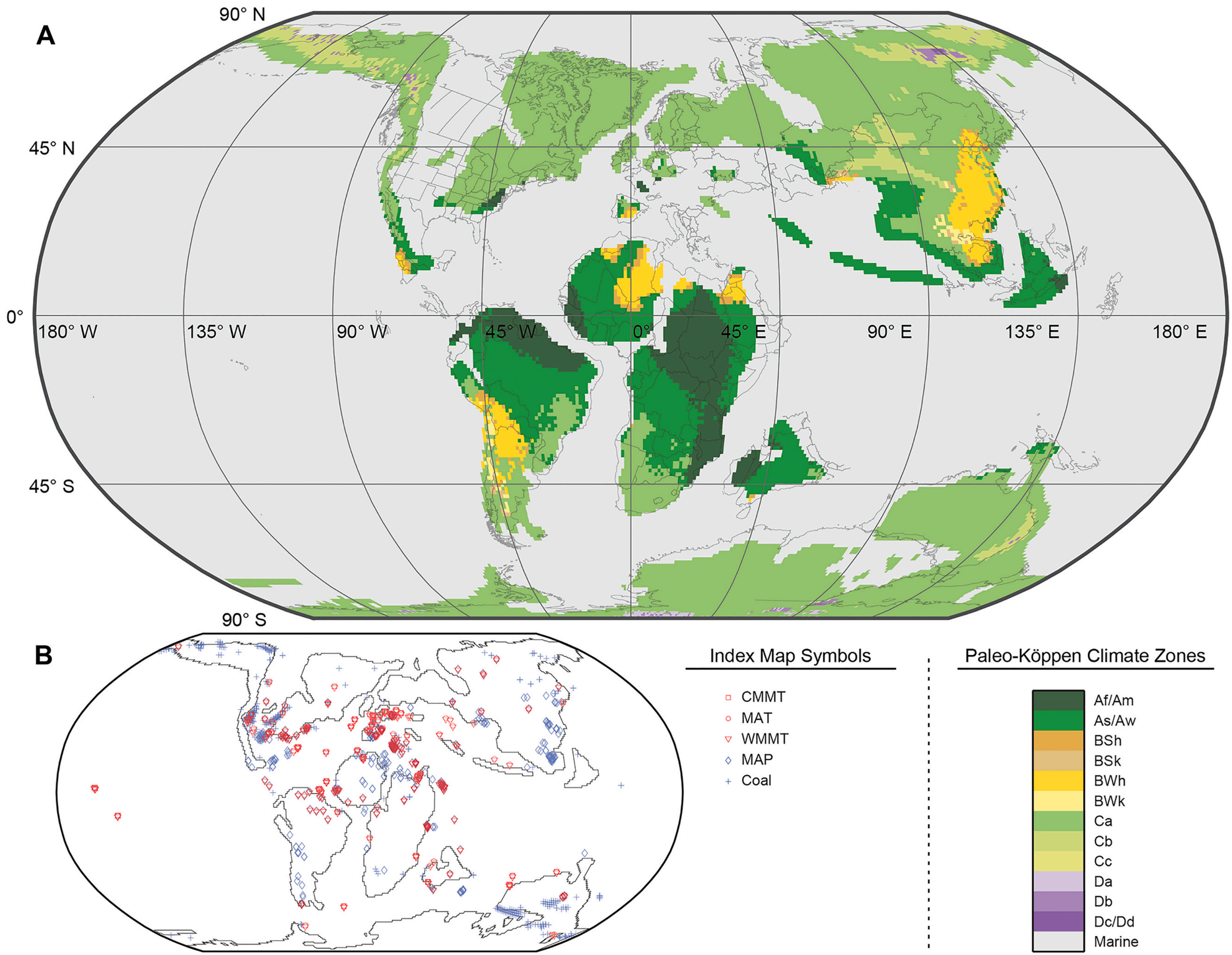

Fig. 11. Cenomanian paleo-Köppen climate zones. Af/Am = tropical rainforest, As/Aw = tropical savannah; BSh = hot steppe, BSk = cold steppe, BWh = hot desert, BWk = cold desert; Ca = temperate, humid subtropical, Cb = temperate, maritime temperate, Cc = temperate, maritime subarctic; Da = continental, hot summer, Db = continental, warm summer, Dc/Dd = continental, subarctic; E = polar.

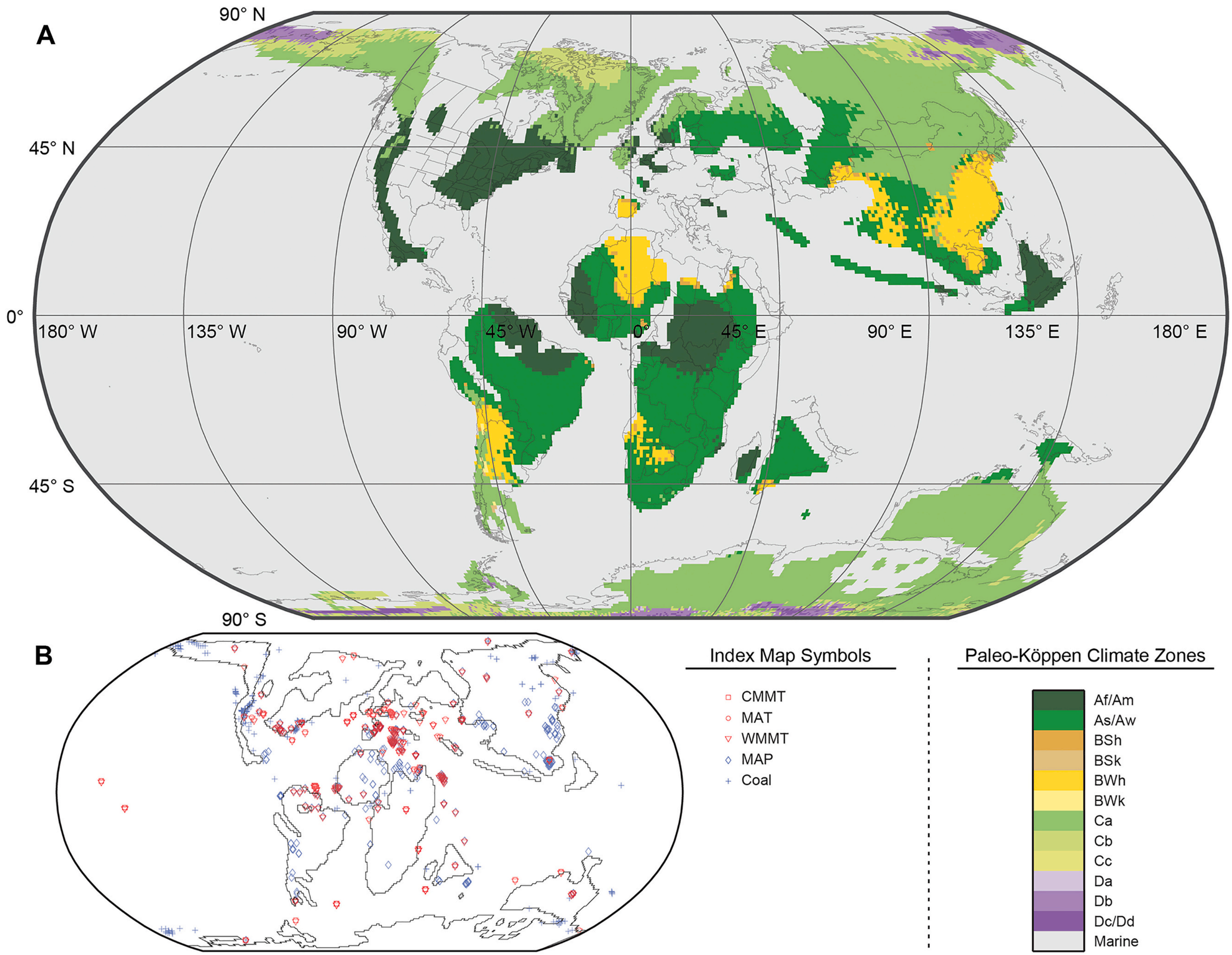

Fig. 12. Turonian paleo-Köppen climate zones. Af/Am = tropical rainforest, As/Aw = tropical savannah; BSh = hot steppe, BSk = cold steppe, BWh = hot desert, BWk = cold desert; Ca = temperate, humid subtropical, Cb = temperate, maritime temperate, Cc = temperate, maritime subarctic; Da = continental, hot summer, Db = continental, warm summer, Dc/Dd = continental, subarctic; E = polar.

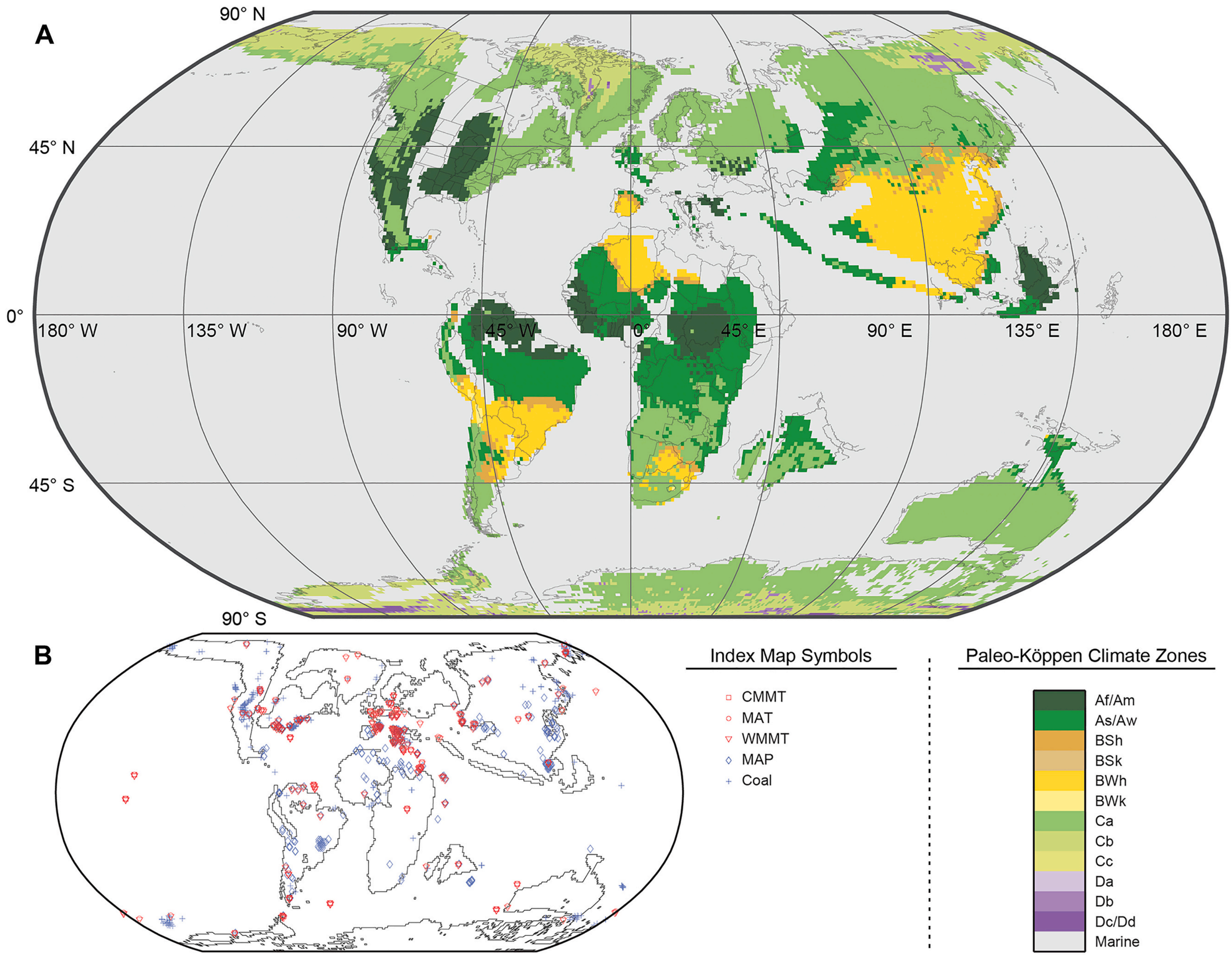

Fig. 13. Coniacian-Santonian paleo-Köppen climate zones. Af/Am = tropical rainforest, As/Aw = tropical savannah; BSh = hot steppe, BSk = cold steppe, BWh = hot desert, BWk = cold desert; Ca = temperate, humid subtropical, Cb = temperate, maritime temperate, Cc = temperate, maritime subarctic; Da = continental, hot summer, Db = continental, warm summer, Dc/Dd = continental, subarctic; E = polar.

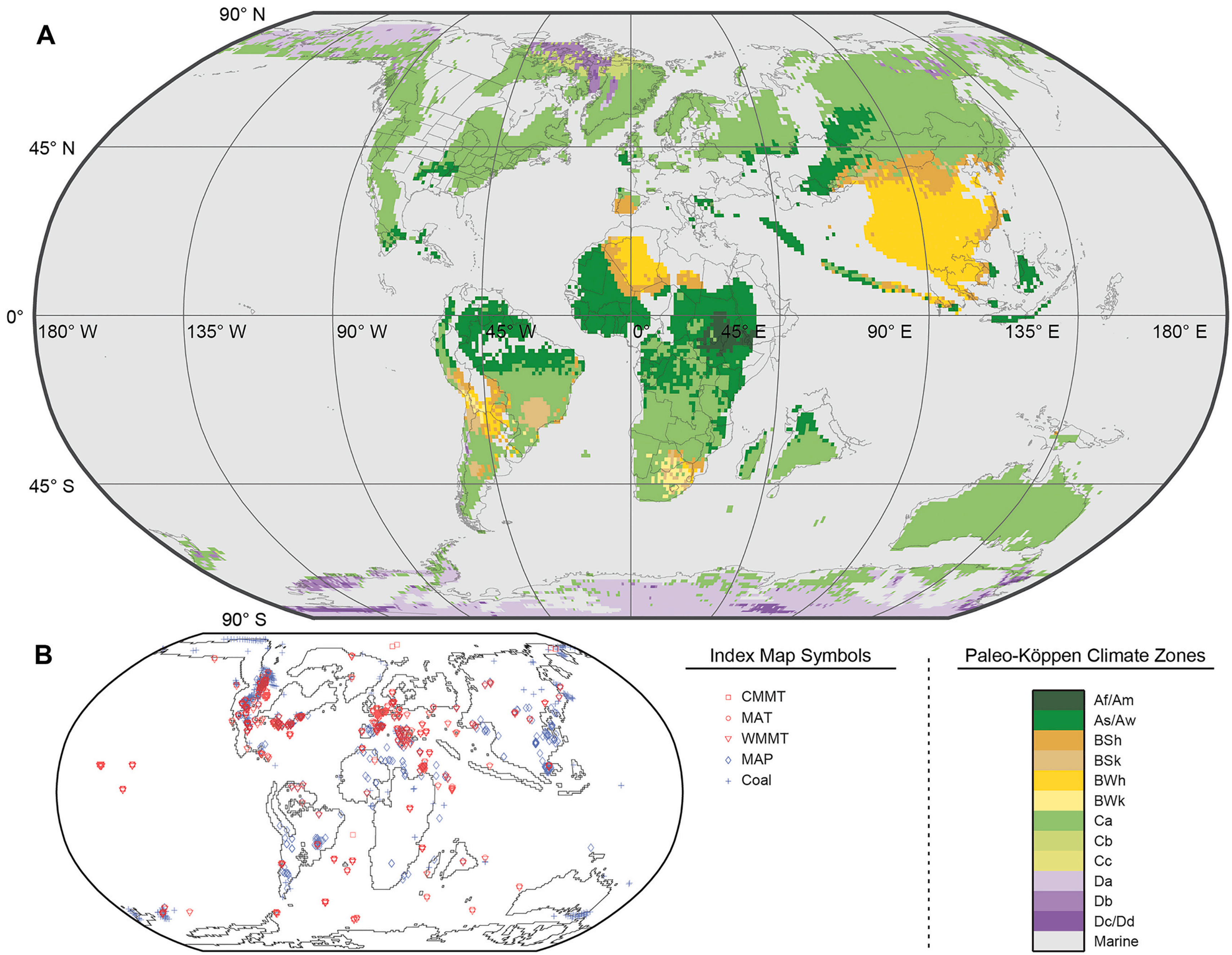

Fig. 14. Campanian paleo-Köppen climate zones. Af/Am = tropical rainforest, As/Aw = tropical savannah; BSh = hot steppe, BSk = cold steppe, BWh = hot desert, BWk = cold desert; Ca = temperate, humid subtropical, Cb = temperate, maritime temperate, Cc = temperate, maritime subarctic; Da = continental, hot summer, Db = continental, warm summer, Dc/Dd = continental, subarctic; E = polar.

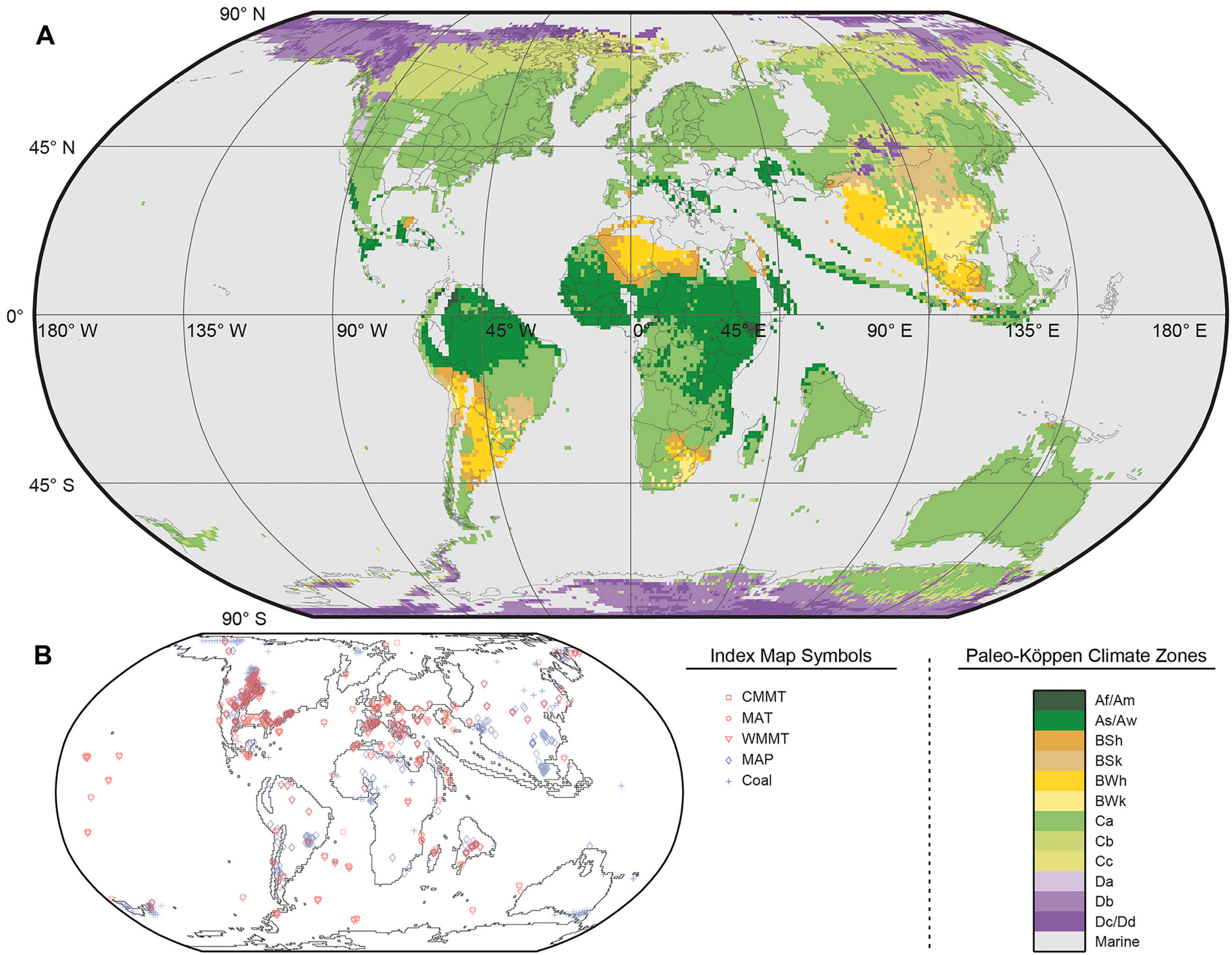

Fig. 15. Maastrichtian paleo-Köppen climate zones. Af/Am = tropical rainforest, As/Aw = tropical savannah; BSh = hot steppe, BSk = cold steppe, BWh = hot desert, BWk = cold desert; Ca = temperate, humid subtropical, Cb = temperate, maritime temperate, Cc = temperate, maritime subarctic; Da = continental, hot summer, Db = continental, warm summer, Dc/Dd = continental, subarctic; E = polar.

in the Turonian, and finally decrease over the remainder of the Late Cretaceous to 14 °C (13 °C) in the Maastrichtian. Interpolated mean global WMMTs closely follow this same pattern, although peak WMMT values occur during the Albian, rather than the Turonian. The mean difference between WMMT and MAT (with and without elevation) averages 10 °C, with a maximum of 13 °C in the Albian and a minimum of 8 °C in the Coniacian-Santonian. Interpolated MAPs decrease from 1048 mm yr^{-1} in the Berriasian-Valanginian to 831 mm yr^{-1} in the Hauterivian-Barremian, then increase to 1507 mm yr^{-1} in the Turonian, followed by a decrease to 1044 mm yr^{-1} in the Maastrichtian.

The mean difference between the MAT and MAT_{elev} reconstructions varies between 0.1 °C (Berriasian-Valanginian) and 1.8 °C (Campanian), and the mean difference between WMMT and $WMMT_{elev}$ reconstructions ranges from 0.01 °C (Hauterivian-Barremian) and 1. °C (Turonian). The maximum and minimum differences between the non-elevation and elevation datasets is summarized in Table SI16. The major MAT_{elev} and $WMMT_{elev}$ differences are associated with high elevation features like mountain ranges and plateaus.

The percent land area identified as arid and sub-humid using the Köppen Aridity index is essentially constant during Berriasian-Valanginian (3% and 10% of terrestrial environments, respectively) and Hauterivian-Barremian (4% and 15%, respectively). From the Hauterivian-Barremian to the Cenomanian, humid areas increase to a maximum of 86% of terrestrial environments, with a corresponding decrease in arid, semi-arid, and sub-humid environments (1%, 6%, and 7%, respectively). Humid and sub-humid areas decrease slightly through the remainder of the Cretaceous (83% and 7%, respectively), and semi-arid areas increase to ~10% of terrestrial areas.

Additionally, the Köppen Aridity results show that the continental subtropical arid and tropical humid belts experienced significant changes in strength and mean latitudinal position and width over the course of the Cretaceous (Fig. 4A and B). In the modern climate system, the tropical humid belt is associated with atmospheric upwelling, extends from 15° N to 15° S, and correspond to Köppen Zone A. In contrast, the subtropical arid belt is associated with atmospheric downwelling, extends from 15° to 35° N/S, and corresponds to Köppen Zone B. During the Berriasian-Valanginian, the continental tropical humid belt is only weakly expressed, and arid to sub-humid climates extend across the equator from the northern to Southern Hemisphere subtropics. Over the remainder of the Cretaceous, the mean latitude of the Northern Hemisphere continental arid belt moves equatorward from 33° N to 24° N. The width of the belt decreases from 27° in the Berriasian-Valanginian to 15° in the Aptian, then increases to 26° in Cenomanian, followed by a continuous decrease to 17° in the Maastrichtian. The strength of the Northern Hemisphere continental arid belt (calculated here as the maximum percent land area within the arid belt that is identified as hyper-arid, arid, semi-arid or sub-humid) increases from 49% in the Berriasian-Valanginian to 72% in the Maastrichtian, with a slight drop in the Cenomanian. The mean latitude of the Southern Hemisphere continental arid belt shows a prolonged decrease over the Cretaceous, from 22° S in the Berriasian-Valanginian to 34° S in the Maastrichtian. The Southern Hemisphere arid belt width increases from 16° in the Hauterivian-Barremian to a maximum of 24° in the Albian, then decreases to 15° in the Maastrichtian.The strength of the Southern Hemisphere continental arid belt decreases from 89% in the Hauterivian-Barremian to 33% in the Cenomanian, followed by a subsequent rise to 55% in the Maastrichtian. The mean latitude of the tropical continental humid belt shifts from 9° N to 3° S over the Cretaceous. The width of the humid belt decreases from 21° in the Berriasian-Valanginian to 18° in the Aptian, increases back to 21° in the Albian to Turonian, and finally decreases back to 18° in the Maastrichtian. The strength of the continental humid belt shows a dramatic increase from 55% in the Berriasian-Valanginian to 94% in the Cenomanian, after which it remains fairly constant over the remainder of the Late Cretaceous.

3.3. Cretaceous Paleo-Köppen climate zone results

Table 7 and Fig. 5 summarize the percentage of terrestrial areas occupied by the various paleo-Köppen climate zones for the modern world (Fig. 6) and each Cretaceous analysis window (Figs. 7-15 and Figs. SI78–86). For the first order paleo-Köppen zones (Table 2), the mean confidence estimates range from 63% to 81% (Table SI17). In contrast, the second order mean confidence estimates are 40% to 56%.

The most obvious contrast between the modern and Cretaceous terrestrial climate systems is the dominance of the Polar (E) climate zone, which accounts for 15% of land area in the modern world, but is completely absent in all of the Cretaceous analysis windows. In contrast, all of the Cretaceous analysis windows are dominated by the Temperate, Humid Subtropical (Ca) and Tropical Savannah (As/Aw) climate zones. The Temperate, Humid Subtropical zone accounts for just 12.9% of land area in the modern world, but ranges from a maximum of 63 ± 0.4% in the Albian to a minimum of 32 ± 0.3% in the Turonian. The Tropical Savannah zone ranges from a maximum of 39 ± 0.4% in the Turonian to 19 ± 0.3% in the Berriasian-Valanginian.

Over the course of the Cretaceous, the spatial extent of the Tropical Rainforest (Af/Am) climate zone varies significantly, from a minimum of 0.5 ± 0.1% in the Maastrichtian to a maximum of 16.4 ± 0.3% in the Turonian. On average, the spatial extent of the Tropical Rainforest climate zone is less than in the modern (percent land area = 7.4%) during the Berriasian-Valanginian to Albian (mean = 2.1 ± 1.3%) and Campanian to Maastrichtian (mean = 0.9 ± 0.5%), but nearly twice as large as in the modern from the Cenomanian to Coniacian-Santonian (mean = 12.9 ± 3.3%).

The mean percent land area classified as Hot Steppe (BSh) during the Cretaceous (4.0%) and the modern (4.3%) is broadly similar; however, there is a substantial difference between the extent of Cretaceous Colde Steppe (BSk) (0.6%) and modern Colde Steppe (6.6%). Additionally, there is a reduction in the both the Hot and Cold Desert (BWk) climate zones during the Cretaceous (8.9 and 0.8%) relative to the modern (13.8 and 5.5%). Aridity is relatively high during the first three Cretaceous analysis windows, and the Desert and Steppe climate zones are concentrated in the continental interior of southern hemisphere Gondwana (pre-rifting South America and Africa) and southern North America (Figs. 7, 8, and 9).

Our paleo-Köppen climate zone analysis resolves two cold phases when cooler Temperate (Cb and Cc) and Continental (Da, Db, and Dc/Dd) climate zones expand: first during the Hauterivian-Barremian and Aptian and second during the Maastrichtian. These two colder phases are separated by the extremely high temperatures and relatively wetter conditions of the mid-Cretaceous.

When the elevation dependent temperature lapse rate is taken into account, the resulting paleo-Köppen climate zone patterns are very similar to the non-elevation results. Generally, there is a reduction in the percentage of Tropical, Hot Desert and Hot Steppe climate zones in the elevation versus the non-elevation results, and an increase in the percentage of Temperate, Continental, Cold Desert, and Cold Steppe climate zones. These changes in climate zone type are associated with high elevation mountain ranges and plateaus like the proto-Andes mountains and the “Nevadaplano” (Suarez et al., 2014).

4. Discussion

4.1. Factors contributing to lower second order paleo-Köppen climate zone confidence estimates

The second order climate zone confidence estimates are on average 20% lower than the first order confidence estimates (Table SI17). We suggest that this difference is primarily due to two factors. First, the second order climate zones are defined by narrower MAT and MAP ranges; thus, the uncertainties associated with our interpolated MAT and MAP values lead to greater variability in the resulting second order climate zone classification than in the first order classification. Second, because our interpolated temperature and precipitation datasets have an associated uncertainty, values close to the temperature or precipitation cut-off between two climate zones (for example, the 1800 mm yr^{-1} MAP cut-off between the Tropical Rainforest and Tropical Savannah climate zones) will be identified as both zones in a significant proportion of the 1000 climate zone identification iterations. Consistent with this observation, when we identify not just the most common climate zone for each grid cell, but the *two* most common climate zones that are identified in at least 25% of the iterations, the second order climate zone confidence estimates increases by 10% (Table SI17), and ranges from a low of 51% in the Campanian to a high of 64% in the Albian. The number of grid cells where two different second order climate zones are identified at least 25% of the time ranges from 24% in the Cenomanian to 43% in the Coniacian-Santonian.

4.2. Temporal and spatial trends in Cretaceous MAT and MAP reconstructions

Both our interpolated terrestrial temperature results and the climate zone classifications confirm past findings that the Cretaceous was a period of warm to hot greenhouse conditions, with mean tropical (24° N to 24° S) terrestrial temperatures ranging from −0.6 °C cooler (Maastrichtian) to 7.0 °C (Turonian) warmer than modern terrestrial tropical temperatures, and mid- to high-latitude (>24° N and < 24° S) terrestrial temperatures being 20.9 °C (Hauterivian-Barremian) to 29.9 °C (Turonian) warmer than in the modern. These values are driven by amplified warming at higher latitudes and the reduced latitudinal temperature gradients that dominated throughout the Cretaceous (Spicer et al., 2008).

As reported in previous studies (e.g., Amiot et al., 2004; O'Brien et al., 2017), terrestrial latitudinal temperature gradients are significantly reduced relative to the modern gradient in all nine Cretaceous analysis windows (Fig. SI40); however, our study also shows that terrestrial latitudinal temperature gradients varied significantly over the course of the Cretaceous, and that these variations were approximately inversely related to MAT. From 30° to 75° N/S, the modern terrestrial temperature gradient as calculated from CHELSA climatologies is $-0.83\,^{\circ}\mathrm{C}\,^{\circ}\mathrm{latitude}^{-1}$. In contrast, the Cretaceous latitudinal temperature gradients ranged from a low of $-0.18\,^{\circ}\mathrm{C}\,^{\circ}\mathrm{latitude}^{-1}$ in the Albian to a high of $-0.36\,^{\circ}\mathrm{C}\,^{\circ}\mathrm{latitude}^{-1}$ during the Hauterivian-Barremian. Our terrestrial latitudinal gradients are cooler than the sea surface temperature gradients reported in Gaskell et al. (2022); however, our findings are consistent with the results of Gaskell et al. (2022) which showed that over the past 95 million years, greenhouse periods are associated with reduced latitudinal temperature gradients, and icehouse periods are associated with steeper latitudinal temperature gradients (Fig. SI40F-I).

The interpolated terrestrial MAP values provide evidence of an enhanced greenhouse hydrologic cycle, consistent with previous Cretaceous and Paleogene studies (e.g., Suarez et al., 2011; Carmichael et al., 2015). Across all nine analysis windows, total terrestrial MAP values are elevated relative to the modern (Fig. SI41), with average global Cretaceous MAP values being 96 mm yr^{-1} (Hauterivian-Barremian) to 606 mm yr^{-1} (Turonian) higher than the modern. These results are consistent with previous studies that have shown that higher global temperatures correspond to higher MAP (Held and Soden, 2006; Carmichael et al., 2015), with maximum total terrestrial MAP rates during the elevated MAT conditions of the Cenomanian, Turonian, and Coniacian-Santionian. Figure SI41 shows that in all nine analysis windows, tropical MAP rates are lower, and mid- to high-latitude MAP rates are higher, than in the modern. These conditions are most evident during the Albian to Coniacian-Santonian, but are even observed during relatively cool phases like the Hauterivian-Barremian and Aptian. We note that these proxy-based MAP reconstructions predict significantly drier equatorial conditions than recent machine learning studies using proxy-model assimilation techniques (Chandra et al., 2021).

Our findings extend the observation of magnified mid- to high-latitude MAP rates from the mid- and Late Cretaceous (Spicer and Herman, 2010; Suarez et al., 2011) to the entire Cretaceous, and offer new proxy-based support for the hypothesis that the reduced latitudinal temperature gradients observed during greenhouse periods like the Cretaceous and early Paleogene may be due in part to increased poleward heat transport associated with an enhanced hydrologic cycle and increased atmospheric water vapor (Ufnar et al., 2004; Rose and Ferreira, 2013; Carmichael et al., 2015). We note that caution is warranted with regard to our highest latitude MAP reconstructions, due to the relatively small number of samples found at latitudes > ± 70° (maximum = 8 samples in the Maastrichtian).

4.3. Temporal and spatial trends in Cretaceous paleo-Köppen climate zones

The proxy-based Cretaceous terrestrial paleo-Köppen climate zone maps presented in this study provide new insight into the evolution of terrestrial climate at high temporal resolution. These maps are fully quantitative and reproducible, and for the first time provide estimates of the uncertainty associated with the climate zone assignments. Additionally, they improve on previous non-quantitative reconstructions by fully incorporating multiple climate parameters to reconstruct defined climate zones.

The paleo-Köppen climate maps derived from the interpolated MAT, MAP, and Aridity datasets reveal several interesting climate and environmental trends over the course of the Cretaceous. As reported in *Section 3.4*, the percent land area associated with modern tropical rainforest environments (MAT ≥23 °C and MAP ≥1800 mm yr^{-1}) varied significantly over the Cretaceous (Fig. 5). During the first four (Berriasian-Valanginian to Albian) and final two (Campanian-Maastrichtian) analysis windows Tropical Rainforest conditions were significantly reduced relative to the modern. It was only during the warmest part of the Cretaceous (the Cenomanian through the Coniacian-Santonian, Figs. 11-13) that the percentage of land area classified as Tropical Rainforest (Af/Am) approached or exceeded that of modern tropical rainforests, and even during those three analysis windows, much of the observed expansion of Tropical Rainforest area occurs along the eastern and western margins of the Western Interior Seaway in North America). Our datasets show that tropical MAT exceeds 23 °C for all 9 analysis windows (Fig. SI40), but tropical MAP only exceeds 1800 mm yr^{-1} during the Cenomanian to Coniacian-Santonian (Fig. SI41E -G). This suggests that the extent of tropical rainforest environments during the Cretaceous was largely controlled by precipitation availability rather than temperature.

We suggest the following explanations for the observed temporal evolution of Tropical Rainforest environments over the course of the Cretaceous. First is the fact that most precipitation proxies are biased towards underestimations of MAP, and may therefore be artificially limiting the abundance of this zone: paleosol proxies are either limited by calibration saturation (e.g., CIA-K; Sheldon et al., 2002) or postburial effects (e.g., Hyland et al., 2015); paleobotanical proxies generally record only growing season totals (e.g., Spicer et al., 2021); and lithologic proxies like coal/lignite are inherently minimum or "lower limit" constraints (see *Section 4.1*). During the Berriasian-Valanginian to Aptian, the lack of extremely-high terrestrial MAP rates over the tropics is likely attributable to two additional conditions. First, the complete (or almost complete) lack of the southern Atlantic Ocean between South America and Africa during this time would have dramatically reduced the evaporative formation of moist, rising air masses over the equatorial regions of these two continents. This in turn would have led to much lower equatorial precipitation rates and prevented the formation of tropical rainforest environmental conditions. Second, cooler MATs during the Hauterivian-Barremian and Aptian would have led to lower evaporation rates relative to the rest of the Cretaceous, further decreasing MAP. During the mid-Cretaceous, a combination of 1) the opening of the southern Atlantic, 2) higher evaporation rates associated with the highest MATs of the Cretaceous, and 3) high eustatic sea level resulting in a larger ocean surface exposed to evaporation, led to an increase in tropical terrestrial MAP and an increase in the extent of Tropical Rainforest zones. During the Campanian and Maastrichtian, the dramatic reduction in the spatial extent of Tropical Rainforest zones is more difficult to explain, particularly in the context of enhanced hydrological recycling resulting from the advent of angiosperm trees (e.g., Boyce et al., 2009, 2010), but may be related to the combined effects of cooling and substantial reductions in sea level (e.g., Haq, 2014).

The mean spatial extent of Hot Desert (BWh) and Hot Steppe (BSh) climate conditions appear to have been as, or more, common during the Cretaceous than in the modern, with significant hot arid periods during the Berriasian-Valanginian to Hauterivian-Barremain and Coniacian-Santonian to Campanian. During the intervening periods (Aptian to Turonian and Maastrichtian), arid conditions were reduced relative to the modern. The spatial extent of Cold Desert (BWk) conditions are significantly reduced over the entire Cretaceous, though Cold Steppe (BSk) conditions were slightly more common during the Albian and Maastrichtian than in the modern. These observations are consistent with the elevated MAT that characterized the Cretaceous. During the Early Cretaceous, the continental interior of Gondwana (South America and Africa) hosted a huge desert (BWk) similar in size to the modern Sahara. This desert straddled the equator and in the Northern Hemisphere extended into the southernmost, subtropical portions of North America. As South America and Africa separated and the Southern Atlantic opened and widened beginning in the Hauterivian-Barremian, this tropical hot desert shrank and divided into separate northern and southern hemisphere subtropical deserts separated by a tropical humid belt. By the Albian, only a small hot desert remained in southern North America and northernmost South America (present-day Columbia) (Fig. 10), and the dry regions in southern South America were slightly more humid, dominated by the Cold Steppe (BSk) climate zone. Over the remainder of the Cretaceous, significant arid zones, dominated by the Hot Desert climate zone, developed in 1) eastern Asia (Figs. 11-14), 2) northern Africa (Figs. 11-15), and 3) southern South America (Figs. 9-13); however, none of these deserts were as large as the Early Cretaceous Gondwana desert. It is interesting to note that in all of the Cretaceous analysis windows, the subtropical arid belts over the continents appear to have been more arid than in the modern, but also more latitudinally restricted (Fig. SI41), with the result that Cretaceous desert regions were slightly more arid but spatially more restricted than modern deserts (see also, *Sections 4.3.1* and *4.3.2*). If this is true, it is consistent with previous suggestions that the enhanced Cretaceous hydrologic cycle produced not just higher precipitation rates, but higher evaporation rates as well (e.g., Barron et al., 1989; Held and Soden, 2006).

Perhaps the most distinctive feature of our Cretaceous climate reconstructions is the dominance of the Temperate, Humid Subtropical (Ca) and Tropical Savannah (As/Aw) climate zones. In the modern, these two zones are also relatively large (second and third largest, respectively; Table 7) and together represent 24% of land area; however, in the Cretaceous these two zones represent a combined 63% (Coniacian-Santonian) to 84% (Albian) of land area (Fig. 5). Based on these observations, we suggest that during the Cretaceous higher Earth surface temperatures and reduced latitudinal temperature gradients resulted in less climate and environmental diversity than in the modern world. This hypothesis is supported by three lines of evidence. First, using the Zhang et al. (2016) paleo-Köppen classification system, the modern climate can be classified into 13 unique climate zones, but our Cretaceous analysis windows only have 6 to 12 unique zones. Second, the mean size of the modern paleo-Köppen climate zones is 7.7% of modern land area, while the mean size of Cretaceous paleo-Köppen climate zones ranges from 8.3 (Maastrichtian) to 16.2% (Coniacian-Santonian and Cenomanian), suggesting that Cretaceous climate zones covered more land area than their modern equivalents. Third, the variance in size between the modern paleo-Köppen climate zones is just 24.5%, but it ranges from 273% (Maastrichtian) to 450% (Cenomanian) for the Cretaceous analysis windows. This is consistent with the observation that the thirteen modern climate zones are similar in size to one another, while the Cretaceous climate zones tend to be dominated by one or two climate zones that cover significantly more area than the remaining climate zones. We note that these results hold true even when considering the paleo-Köppen$_{elev}$ Cretaceous reconstructions that take into account the elevation-dependent temperature lapse rate. Importantly, this hypothesis is consistent with paleo-Köppen climate zone calculations based on prior Community Earth System Model (CESM) version 1.2 simulations of latest Paleocene, Paleocene-Eocene Thermal Maximum (PETM), and Early Eocene Climatic Optimum (EECO) climates (Lunt et al., 2017, 2021), and Global Fluid Dynamics Laboratory Climate Model 2.1 (GFDL CM2.1) simulations of the Eocene-Oligocene Transition (EOT) climate (Hutchinson et al., 2018, 2019, 2021). The CESM and GFDL CM2.1 models predict mean terrestrial MATs of 10.4 °C, 25.1 °C, 17.0 °C, and 10.3–15.9 °C, and 11, 7, 8, and 11–12 unique climate zones for the latest Paleocene, PETM, EECO, and EOT, respectively.

The hypothesis that Cretaceous climates were characterized by fewer, more extensive climate zones makes intuitive sense, because significantly higher land surface temperatures should result in the expansion of the warmest zones (e.g., Tropical and Hot Dry zones), and the elimination of the coldest zones (e.g., Polar). Consistent with this idea, our data shows that the number of unique climate zones varies inversely with the mean global MAT (e.g., higher mean global MAT corresponds to fewer unique climate zones; Table SI18), though our nine analysis windows represent too small a dataset to rigorously test this hypothesis. One potential challenge to this interpretation is the relatively low spatial density of temperature and precipitation data points during the Cretaceous. The number of unique climate zones is positively correlated with dataset size (total number of MAT and MAP samples); however, the relationship is slightly weaker ($R^2 = 0.36$) than the inverse relationship between unique climate zones and global MAT ($R^2 = 0.58$). In the future, additional temperature and precipitation reconstructions will make it possible to produce more nuanced paleo-Köppen maps and determine whether the climatic zone homogeneity observed in our maps is an artifact of data density or a real feature of the Cretaceous climate system (see *Section 4.5*).

Another significant feature of the Cretaceous climate system that our paleo-Köppen results emphasize is the evolution of high latitude climate over the nine analysis windows. Coeval with the previously discussed cool phases during the Hauterivian-Barremian to Aptian and the Campanian to Maastrichtian, there is an expansion of cool Temperate (Cb and Cc) and Continental climate zones at higher latitudes, and our climate maps reveal interesting spatial patterns to these trends. For example, during both the Early and Late Cretaceous cold phases, our Northern Hemisphere reconstructions suggest that high latitude North America was characterized by larger regions of colder MAT and WMMT (climate zones Cb, Db, and Dc/Dd) than high latitude eastern Asia (Figs. 8, 9, 14, and 15). Additionally, during the Early Cretaceous cold phase, Continental climate zones extend further equatorward in the Southern Hemisphere than in the Northern Hemisphere (Figs. 8 and 9). Finally, our maps show that Polar climate zones were completely absent during the Cretaceous, even in our paleo-Köppen$_{elev}$ reconstructions and across all 500 Monte-Carlo simulations for each analysis window. With the caveat that additional high-latitude temperature data is needed, our findings imply that even after proxy uncertainties are taken into account, Cretaceous temperature conditions were likely too warm for the formation of extensive or long-term ice sheets or regions of alpine glaciation, consistent with previous proxy studies (e.g., Spicer and Herman, 2010; Hay et al., 2019).

In addition to highlighting the spatial and temporal climate and environmental trends discussed above, our results make it possible to test several long-standing hypotheses regarding key features of the Cretaceous climate system. In the following sections, we present two case studies that highlight the utility of our proxy-based climate reconstructions.

4.3.1. Case study 1: early development of the Cretaceous equatorial humid belt

Previous reconstructions of Cretaceous climate have been interpreted as evidence that the modern Intertropical Convergence Zone (ITCZ) first began as an equatorial humid belt (EHB) during the Albian (e.g., Chumakov et al., 1995; Boucot et al., 2013). Initially, it was proposed that the ITCZ did not exist before the Albian (Chumakov et al., 1995); however, subsequent studies pointed out that 1) a complete shutdown of tropical upwelling is climatologically impossible, especially over areas of open ocean like the Pacific (Hay and Floegel, 2012); and 2) the arid conditions over Gondwana were likely due to the huge size of the supercontinent, which prevented coastal moisture from penetrating into the continental interior (e.g., the "Supercontinent effect"; Hay and Floegel, 2012; Santos et al., 2022).

Based on new palynomorph richness data from 13 sedimentary basins in South America and Brazil, Santos et al. (2022) proposed that the terrestrial EHB over Gondwana actually began to develop by the late Aptian, approximately 7 Ma before the end of the Aptian and beginning of the Albian. The paleoclimate reconstructions presented in our study do not incorporate the Santos et al. (2022) data; nevertheless, our findings are consistent with a pre-Albian development of a terrestrial EHB over Gondwana. In fact, our global reconstructions suggest that humid conditions may have developed over equatorial Gondwana even earlier. During the Berriasian-Valanginian, humid conditions (Aridity Index >15.6) can be found on the west and east coasts, in present day Peru and the eastern Sahara, based on the presence of coal and rare bauxite deposits; however, the continental interior along the equator is dominated by semi-arid conditions (Aridity Index = 5.7–13.6) based on the presence of abundant evaporites and erg deposits. These moisture conditions correspond with the Hot Desert (BWh) climate zone, which dominates the interior of Gondwana (Fig. 7). By the Hauterivian-Barremian, humid and sub-humid conditions, indicated by the appearance of bauxite deposits along the central north coast and equatorial interior of Gondwana, have already penetrated into Gondwana's equatorial interior, and the climate classification has shifted to Tropical Savannah (As/Aw) with a small increase in the Hot Steppe (BSh) climate zone as well (Fig. 8). In the Aptian, there is a further expansion of humid conditions in South America (western Gondwana) evidenced by additional bauxite deposits, the interior climate of Gondwana continues to be dominated by the Tropical Savannah climate zone, and there is an expansion of the Tropical Rainforest climate zone along Gondwana's eastern coast (Fig. 9). By the Albian, South America and Africa have completely separated. Humid/sub-humid conditions define all of equatorial Africa and most of equatorial South America, though there is a small area of semi-arid conditions in northwestern South America. These wetter conditions are indicated by an increase in the number of coal and bauxite deposits during this time period, and a decrease in evaporite, erg, and paleosol carbonate records. The Tropical Savannah climate zone continues to be the dominant environment in the Albian (Fig. 10). We note that each of our analysis windows represent time-averaging of data, and that within the general trends described above, all of these Early Cretaceous stages saw fluctuations between wetter and drier conditions.

Our results support the hypothesis that a wetter environment dominated equatorial Gondwana by the Aptian, as proposed by Santos et al. (2022); additionally, our climate reconstructions suggest that development of the terrestrial EHB began even earlier in the Hauterivian-Barremian. Santos et al. (2022) proposed that the development of wetter conditions over equatorial Gondwana was driven largely by a southward shift in the Cretaceous humid belt. Interestingly, our Aridity Index results show this predicted trend, with the mean latitudinal position of the equatorial humid belt shifting southward from ~9° N in the Berriasian-Valanginian to 1° S in the Albian (Fig. 4B). Beginning in the Hauterivian-Barremian, this shift in the equatorial humid belt coincided with a widening and southward shift of the Northern Hemisphere terrestrial arid belt and a southward shift of the Southern Hemisphere terrestrial arid belt that continued into the Albian (Fig. 4B).

In summary, our Early Cretaceous climate reconstructions show that wetting of the equatorial Gondwana interior began well before the Albian, consistent with the findings of Santos et al. (2022). Additionally we provide new evidence confirming the hypothesis that the development of the terrestrial EHB over Gondwana was accompanied by a distinct southward shift in the equatorial humid belt.

4.3.2. Case study 2: evolution of atmospheric circulation patterns during the Cretaceous

In this second case study, we explore how our global proxy-based paleoclimate reconstructions can shed new light on previously reported regional Cretaceous climate patterns. Hasegawa et al. (2012) proposed that the latitudinal position of Cretaceous lithologic arid climate indicators and wind-direction reconstructions from eolian sandstones in East and Southeast Asia provide evidence of dramatic Hadley cell expansion during the Berriasian to Barremian and Coniacian to Maastrichtian, and shrinking of the Hadley cell from the Aptian to Turonian. Based on these sedimentary observations, they proposed that—consistent with model simulations and proxy evidence from Quaternary glacial-interglacial cycles—a shift from a low CO_2 icehouse world to a moderately-high CO_2 greenhouse world causes an expansion of the Hadley cells, but that as continued warming causes a transition to a high CO_2 hothouse world a threshold is crossed and the Hadley cells begin to shrink (see Hasegawa et al., 2012 section 3.3 for more details).

Consistent with the Berriasian to Barremian results reported by Hasegawa et al. (2012), our Berriasian-Valanginian and Hauterivian-Barremian Aridity Index results reveal two large semi-arid zones in eastern Asia centered on 28–30° N and 43–45° N and a smaller semi-arid zone at ~14° N. These semi-arid zones correspond to Hot Desert and Hot Steppe climate zones (Figs. 7 and 8). This is consistent with the Hasegawa et al. (2012) proposal that the earliest part of the Cretaceous was dominated by a relatively wide arid belt and an expanded Hadley cell. In addition to these eastern Asia results, our study provides additional global context, showing that in North America and northern Gondwana, semi-arid and arid conditions covered a continuous belt from 5° N to 39° N, and that the Southern Hemisphere arid belt extended from 30° S to 47° S. These findings suggest that a relatively wide arid belt was a global feature of the Berriasian-Valanginian and Hauterivian-Barremian climate systems.

In the Aptian through Cenomanian, our reconstructions suggest that semi-arid conditions associated with Steppe and Desert climate zones—while reduced—persisted in eastern Asia at latitudes up to 43–53° N (Figs. 9 to 11). These dry conditions are indicated by the presence of evaporites and paleosol carbonates in Kyrgyzstan, Mongolia and China (Boucot et al., 2013; Cao et al., 2019), as well as low MAP reconstructions based on paleosol geochemistry (Harper et al., 2020) and vertebrate $\delta^{13}C$ (Amiot et al., 2015). In North America, semi-arid conditions also continued in Aptian and Albian North America up to a latitude of 44° N and 35° N, but retreated towards the equator in the Cenomanian. In the Southern Hemisphere, the poleward extent of semi-arid and arid conditions ranged from ~33° S to 53° S. In contrast to the hypothesis put forward by the Hasegawa et al. (2012) study, our reconstructions do not reveal a consistent global pattern of a narrowed or reduced Hadley cells during this time period; rather, different regions display distinctly different temporal trends in aridity and climate zone evolution.

The Turonian saw a reduction in the overall extent of arid and semi-arid climates world-wide (Figs. 12 and SI74), likely related to the increased moisture carrying capacity of a warmer atmosphere (e.g., Held and Soden, 2006). Desert and steppe climates almost completely disappeared in North America, and were significantly reduced in South America. In eastern Asia, the northern boundary of the semi-arid and

Table 7
Comparison of proxy-based and model simulated Cretaceous temperature reconstructions.

Study	GMST (C)	Tropical (C)	Polar (C)	Deep Sea (C)	Temperature Gradient (° latidue^{-1})
Modern (2000 CE)					
Legates and Willmott, 1990	14	26	−20	4	0.67
90 Ma (Turonian)					
This Study	28	33	12	21	0.34
Scotese et al. (2021)	27	32	14	22	0.32
Valdes et al. (2021)	19	30	−5	8	0.66
Li et al. (2022)	23	33	5	14	0.53
110 Ma mid-Albian)					
This Study	20	27	15	18	0.17
Scotese et al. (2021)	21	27	5	16	0.37
Valdes et al. (2021)	24	34	2	14	0.63
Li et al. (2022)	20	32	−2	10	0.66
130 Ma (Hauterivian-Barremian)					
This Study	18	30	4	13	0.4
Scotese et al. (2021)	21	29	2	16	0.47
Valdes et al. (2021)	21	32	−3	12	0.63
Li et al. (2022)	21	32	−3	11	0.7

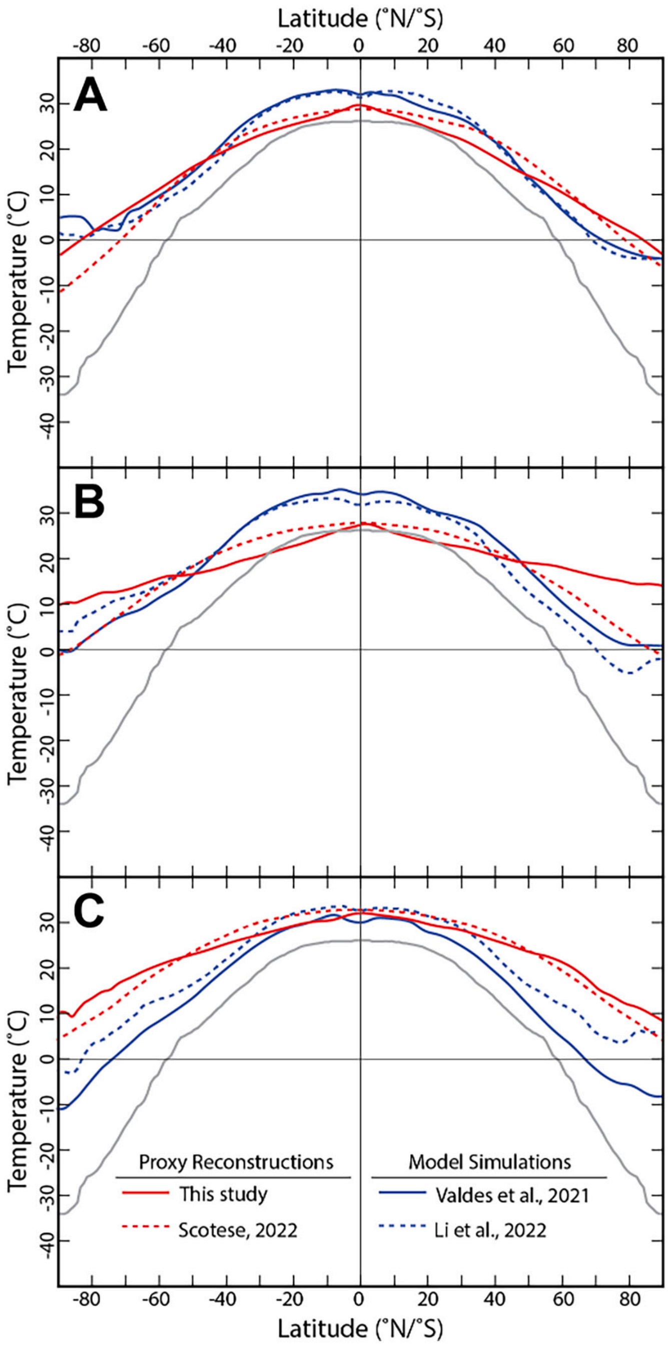

Fig. 16. Comparison of pole-to-equator global surface temperature gradients from two proxy-based reconstructions (this study; Scotese, 2022) and two model simulations (Valdes et al., 2021; Li et al., 2022) for the Hauterivian-Barremian (A), the Albian (B), and the Turonian (C). Red lines indicate the proxy-based reconstructions and blue lines indicate the model simulations. The modern pole-to-equator global surface temperature gradient (gray line) is shown for comparison (data from Legates and Willmott, 1990). (For interpretation of the references to colour in this figure legend, the reader is referred to the web version of this article.)

arid zone describes a distinct parabolic shape, with a relatively high latitudinal position (43–45° N) at longitudes of 68° E and 116° E, and a prominent southward deflection of the boundary at 90° E (Fig. SI74). This spatial moisture pattern leads to Hot Desert Zones at 68° E and 116° E, separated by a Tropical Savannah zone. We note that even though the overall spatial extent of dry climate zones was reduced in Turonian eastern Asia, Desert environments still extended northward to ~45° N, especially on the eastern margin of the continent, which is inconsistent with the idea of a narrowed Hadley cell during this time period (Fig. 10).

During the Coniacian-Santonian, there was a global increase in the spatial extent of Desert and Steppe climate zones in eastern Asia, South America and Africa (Fig. 13 and Fig. SI75), with arid environments extending to 48° N in eastern Asia and 50° S in South America and Africa. It is interesting to note that the poleward boundaries of arid regions in Africa and South America extend to relatively high latitudes in both hemispheres (33° N/51° S). In contrast, North America remained dominated by humid conditions (Fig. 13 and SI75). Once again, these reconstructions suggest that while arid conditions extended to high latitudes in eastern Asia and South America, this was not necessarily a global phenomena. In eastern Asia, the Coniacian-Santonian saw a significant expansion in the longitudinal extent of arid areas, but not a distinct change from the Turonian in terms of the poleward boundary of the arid belt, as posited by Hasegawa et al. (2012).

The Campanian and Maastrichtian saw a slight decline in the spatial extent of Desert and Steppe climate zones in eastern Asia, a slight equatorward shift in the southern boundary of the South American and African climate zones, and a decrease in MAP rates over North America. Otherwise, global climate patterns are similar to the Coniacian-Santonian. Again, despite changes in the magnitude and longitudinal extent of arid climate zones, the latitudinal position of the poleward arid belt boundary in eastern Asia does not shift significantly.

In summary, our global datasets suggest that rather than the Early and Late Cretaceous being dominated by large-scale global expansions and retreats of the northern and southern arid belts with an intervening equatorward shift during the mid-Cretaceous, the period was instead characterized by 1) a general widening of both arid belts over the course of the Cretaceous (Fig. 4), 2) a shift from a more diffuse arid belt in the northern hemisphere and a dominant (more pronounced) southern hemisphere arid belt during the Early Cretaceous, to a diffuse arid belt in the southern hemisphere and a dominant arid belt in the northern hemisphere; and 3) complex regional arid belt patterns that exhibited significant change over ~80 million years.

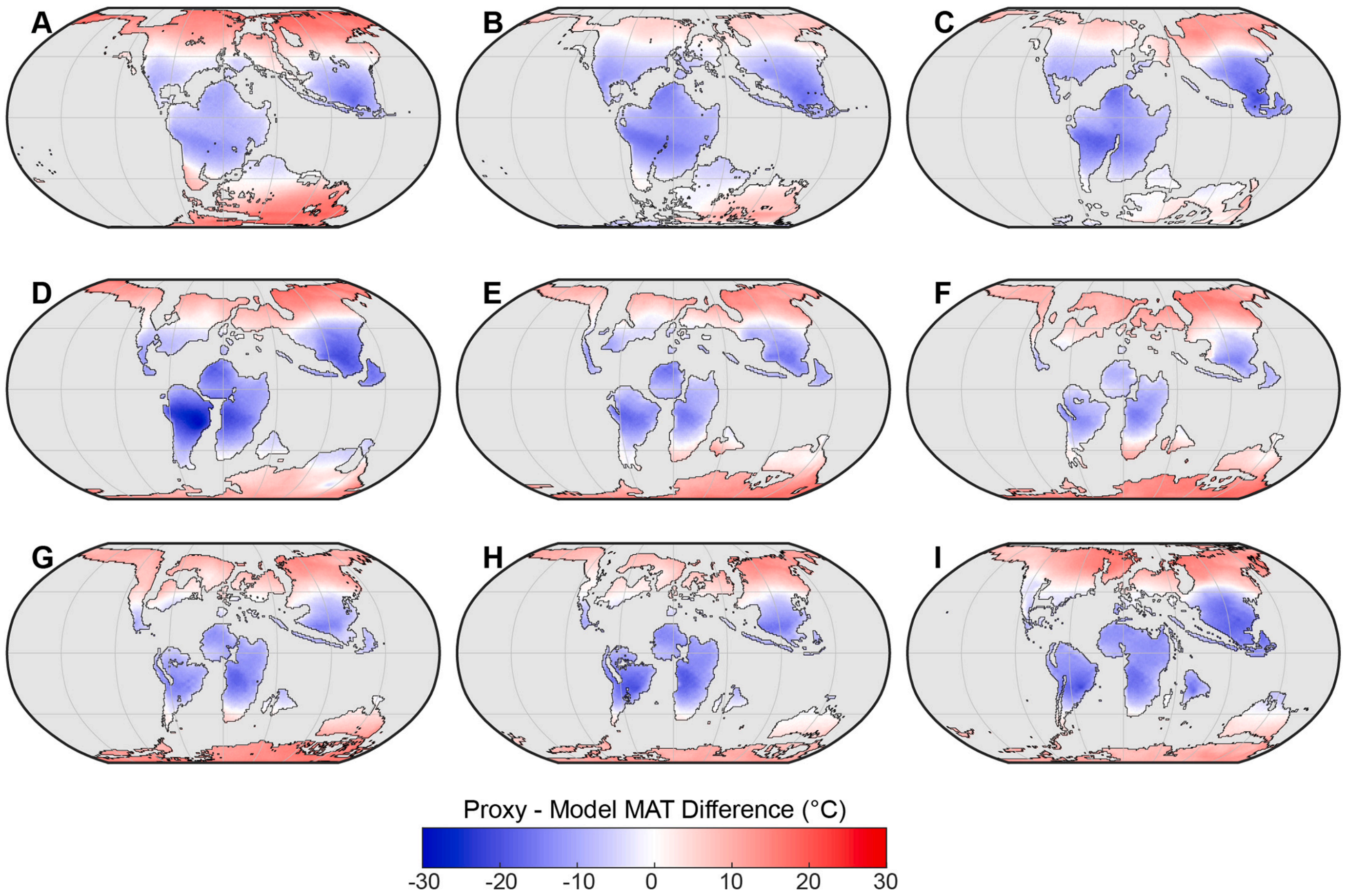

Fig. 17. Difference between proxy-reconstructed MAT values reported in this study and simulated MAT values from the HadCM3BL-M2.1aD model from Valdes et al. (2021). A) Berriasian-Valanginian, B) Hauterivian-Barremian, C) Aptian, D) Albian, E) Cenomanian, F) Turonian, G) Coniacian-Santonian, H) Campanian, I) Maastrichtian.

4.4. Comparison to other Cretaceous proxy reconstructions and model simulations

In this section we compare our temperature and climate zone reconstructions to the Scotese (2022) proxy-based Cretaceous pole-to-equator temperature dataset and to Cretaceous model simulations by Li et al. (2022) and Valdes et al. (2021). First we examine global pole-to-equator temperature reconstructions, and second we compare the paleo-Köppen results of our study to Cretaceous climate zone classifications using the Valdes et al. (2021) model simulations.

4.4.1. Proxy and model pole-to-equator temperature comparisons

Pole-to equator temperature diagrams are a convenient was to compare the results of various climate models because the following values can be directly estimated from the diagram: tropical temperature, mid-latitude temperature, polar temperature, and the pole to equator temperature gradient (30° N to 60° S; Table 7).We compare and contrast the pole-to-equator temperatures from our mean global temperature reconstructions for the Hauterivian-Barremian (131 Ma), Albian (107 Ma), and Turonian (92 Ma) to another recent Cretaceous paleoclimate reconstruction (Scotese, 2022) and two model simulations (Valdes et al., 2021; Li et al., 2022; Fig. 16). These three analysis windows were chosen because they represent cold, temperature, and hot Cretaceous climate conditions, respectively.

The Hauterivian-Barremian was relatively cool compared to the mid- and Late Cretaceous (Scotese, 2022). Figure SI2 summarizes the evidence for these mild temperatures, including the occurrence of dropstones, glendonites, and a few tillites (pebbly mudstones, Boucot et al., 2013) in polar latitudes that co-occur with evidence of temperate forests (coal, plant fossils) and dinosaurs and may suggest spatially restricted and/or ephemeral glacial conditions. The latitudinal gradients produced by the computer simulations (Valdes et al., 2021; Li et al., 2022) and the proxy-based reconstructions (this study; Scotese, 2022) are similar (Fig. 16A). Tropical temperatures average ~ 30 °C and the mean latitudinal temperature gradient is 0.55° latitude^{-1}, which is relatively steep compared with other Cretaceous stages, but is significantly more shallow than the modern latitudinal temperature gradient (0.67° latitude^{-1}). Both the proxy reconstructions and model simulations converge on an average polar temperature of (0 °C), which would have been cool enough for permanent ice above ±85° latitude.

Estimated tropical temperatures during the mid-Albian vary widely. The computer simulations (Valdes et al., 2021; Li et al., 2022) produce very warm tropical temperatures ranging from 32 °C to 34 °C. Summer temperatures under these regimes often would have exceeded 40 °C, which would have severely impeded photosynthesis in most terrestrial plants (Hüve et al., 2011). The proxy-based paleotemperature reconstructions (this study and Scotese et al., 2021) converge on average tropical temperatures of ~27 °C, which is slightly warmer than modern tropical temperatures (26 °C). It is interesting to note that the majority of the studies indicate mild-to-cool polar temperatures (~1 °C). It should be noted that the high latitude results of this study (solid red line, Fig. 16B) differ significantly from the results of the other three climate models. The pole-to-equator gradient is very shallow, ~ 0.18° latitude^{-1}, and the average polar temperature is very warm (~15 °C). This divergent result is probably due to the inclusion of quantitative, high-latitude temperature reconstructions in our study that were not

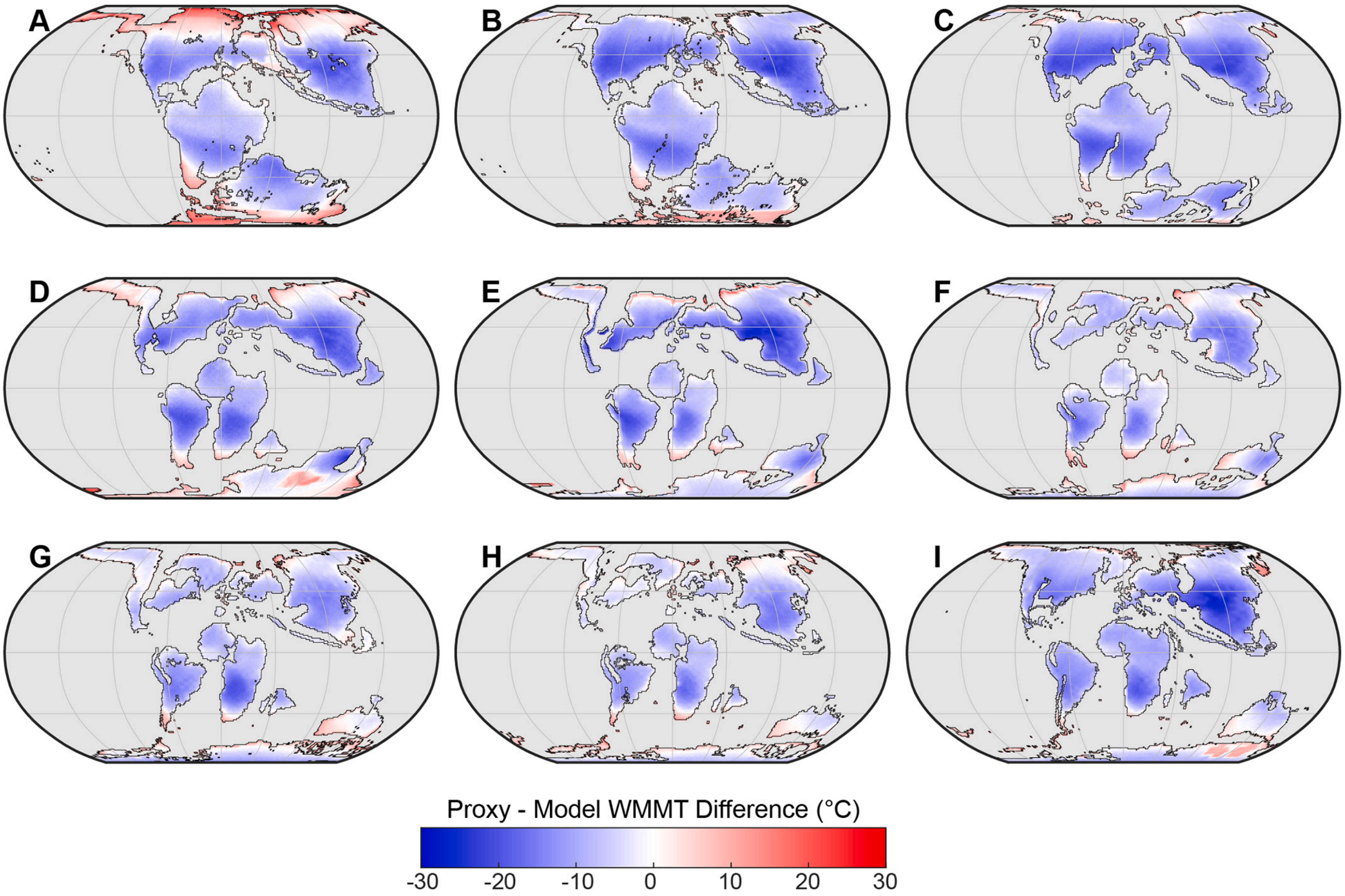

Fig. 18. Difference between proxy-reconstructed WMMT values reported in this study and simulated WMMT values from the HadCM3BL-M2.1aD model from Valdes et al. (2021). A) Berriasian-Valanginian, B) Hauterivian-Barremian, C) Aptian, D) Albian, E) Cenomanian, F) Turonian, G) Coniacian-Santonian, H) Campanian, I) Maastrichtian.

included in the Scotese, 2022 dataset (e.g., leaf physiognomy temperatures from Miller et al. (2006) and Parrish (1998); pedogenic carbonate $\delta^{18}O$ temperatures from Ferguson et al. (1999); and high-latitude marine $\delta^{18}O$ temperatures from Goswami, 2012).

The Turonian (Scotese, 2022) was the warmest interval of the Cretaceous (Fig. 16C), and both the proxy-based reconstructions (this study; Scotese, 2022) and model simulations (Valdes et al., 2021; Li et al., 2022) show a similar range of elevated tropical temperatures (~30 °C). The latitudinal temperature gradients fall into two groups: a proxy-based low temperature gradient of 0.34° latitude^{-1}, and a model-simulated high temperature gradient of 0.66° latitude^{-1}. Consequently, average polar temperatures are ~10 °C for climate models based on geologic data (red lines), whereas polar temperatures produced by computer simulation (gray lines) are much cooler (~0 °C).

In summary, both the proxy-based reconstructions and model simulations (this study; Scotese et al., 2021; Valdes et al., 2021; Li et al., 2022) produce temperatures much warmer than the modern world (Fig. 16). Tropical temperatures were, on average, 6 °C warmer than the modern world and polar temperatures were much warmer (+24 °C) than the modern world. The proxy-based reconstructions and the model simulations produce very similar average global temperatures (~22 °C, Table 7). It is important to note that despite the similarity in global average temperatures produced by the proxy-based reconstructions and model simulations, the latitudinal temperature gradients produced by each technique are systematically different. As can be seen in Fig. 16 and Table 7, the model simulations of temperature (blue lines) are warmer near the equator than the proxy-based temperature estimates (red lines). Conversely, at high latitudes the model simulations of temperature are cooler than the proxy-based temperature estimates.

4.4.2. *Proxy and model paleo-Köppen climate zone comparison*

We calculated paleo-Köppen climate zones for the stage-level model output from Valdes et al. (2021), which presented 109 global climate simulations for the Phanerozoic using the HadCM3BL-M2.1aD version of the Hadley Center Model (see Valdes et al., 2017 for a full description of the model). To facilitate comparison between the model and our proxy reconstructions, the model output was interpolated to the same 1°x1° grid as our climate maps. For analysis windows where multiple model simulations were performed (e.g., the early, middle, and late Albian), the results were averaged in order to compare proxy and model results over the same time period. Figures SI87 to SI88 show the resulting paleo-Köppen climate zones for the model simulations.

For all nine analysis windows, the model simulations yield significantly higher latitudinal temperature gradients, overestimating equatorial MAT and WMMT and underestimating high latitude MAT and WMMT relative to our proxy reconstructions, but generally agreeing across the mid-latitudes (Figs. 17, 18, SI89, and SI90). Table SI19 summarizes the proxy-model comparison results, with MAT RMSE values ranging from 4.1 (Hauterivian-Barremian and Aptian) to 11.0 °C (Albian), and WMMT RMSE values ranging from 3.4 (Campanian) to 14.1 °C (Albian). Model-proxy temperature disagreements have been a longstanding issue in Mesozoic and Cenozoic greenhouse paleoclimatology (Kump and Pollard, 2008; Huber and Caballero, 2011; Hollis et al., 2019). In part, the disagreement between our proxy-based results and the Valdes et al. (2021) model simulations (particularly at low latitudes) may be due to the 40 °C and 50 °C upper limit we imposed on our

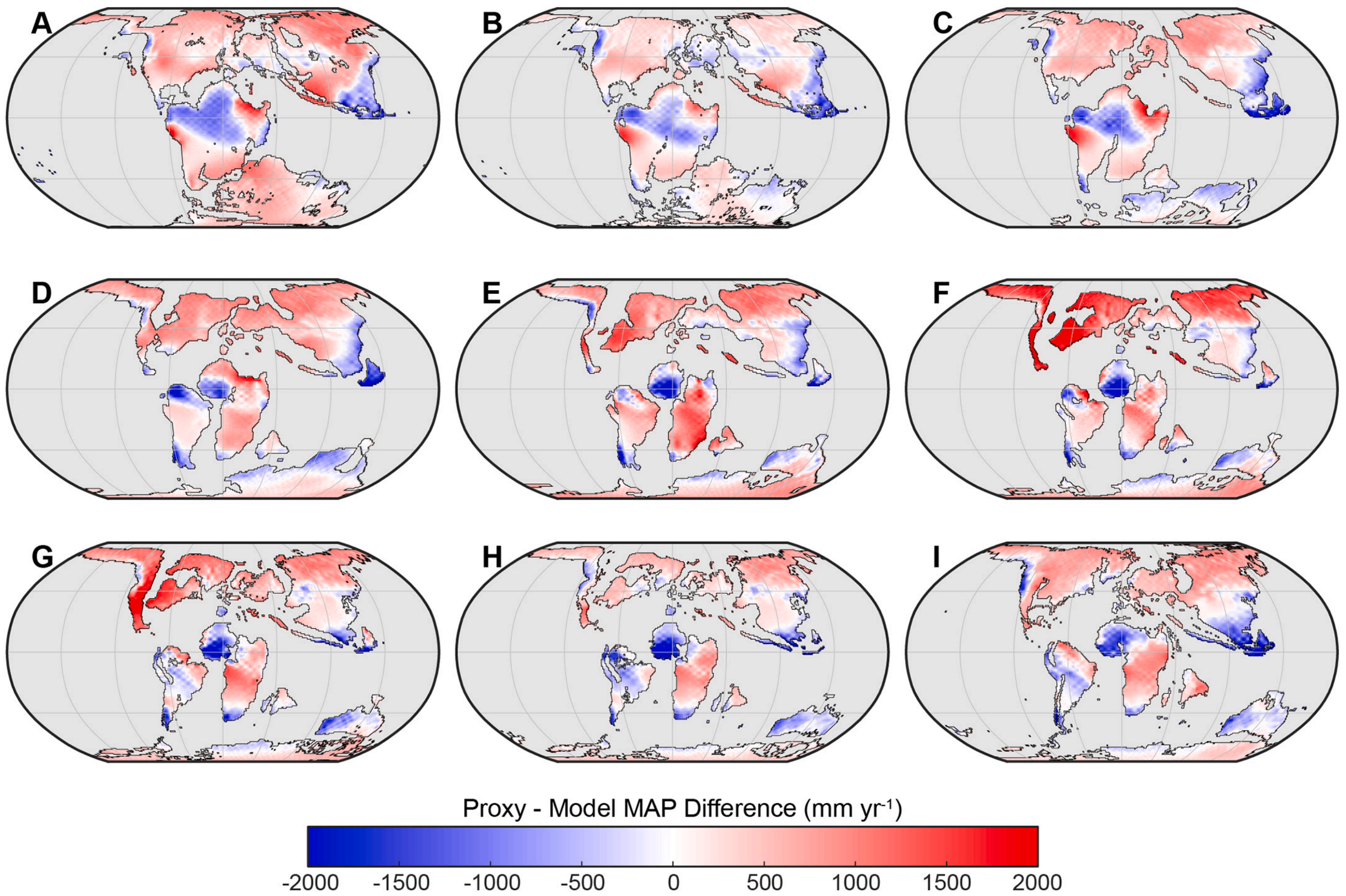

Fig. 19. Difference between proxy-reconstructed MAP values reported in this study and simulated MAP values from the HadCM3BL-M2.1aD model from Valdes et al. (2021). A) Berriasian-Valanginian, B) Hauterivian-Barremian, C) Aptian, D) Albian, E) Cenomanian, F) Turonian, G) Coniacian-Santonian, H) Campanian, I) Maastrichtian.

censored MAT and WMMT data, respectively. However, we suggest that these upper limits are reasonable in light of 1) the well-documented decline in photosynthesis at temperatures greater than ~35 °C (e.g., Berry and Bjorkman, 1980; Sharkey, 2000), 2) evidence for irreversible leaf damage and photosynthesis inhibition at temperatures >40 °C (Hüve et al., 2011), and 3) the presence of coal and plant fossils even at low latitudes during all of our Cretaceous analysis windows (Figs. SI29 to SI37).

Relative to our proxy MAP reconstructions, the Valdes et al. (2021) model simulations also generally overestimate MAP rates in areas with good proxy evidence for arid conditions (e.g., continental interior of Gondwana during the Early Cretaceous and Southeast Asia), underestimate MAP rates in mid- to high-latitude continental interiors (e.g., North America, Eurasia and Antarctica), and significantly overestimate ITCZ-related tropical MAP values (Fig. 19). Proxy-model RMSE values range from 251 (Hauterivian-Barremian) to 519 mm yr^{-1} (Turonian). These comparisons suggest that the model employed in the Valdes et al. (2021) fails to capture the progressive development of the EHB over the course of the Early Cretaceous and the enhanced poleward moisture transport indicated by proxy records. The inability of the model to accurately simulate the poleward moisture transport is especially critical because the movement of moisture towards the poles has been proposed as a critical process for transporting heat away from the tropics and towards high latitudes (Kump and Pollard, 2008), which likely has direct bearing on the model's overestimation and underestimation of tropical and polar temperatures, respectively.

With regard to the paleo-Köppen climate zones, Fig. 20 shows the probability of the Valdes et al. (2021) model and our proxy-based climate zone reconstructions identifying the same climate zone for a given grid cell. Across all nine analysis windows, there is a relatively high probability of identifying the same climate zone across the mid-latitudes, and significantly lower probabilities at high latitudes. This pattern reflects the steeper latitudinal MAT gradients predicted by the model relative to our proxy-based MAT reconstructions (c.f., Figure SI40). Interestingly, the model and our proxy-based climate zone classifications not only yield very low probabilities of matching climate zones for proxy-poor areas, but also for some proxy-rich areas where climate conditions are well-constrained by physical data, such as the western coast of the Western Interior Seaway during the Maastrichtian (Figs. SI10, SI19, SI28, and SI37) and the southern Atlantic region of Africa and South America during the Albian (Figs. SI5, SI14, SI23, and SI32).

In terms of spatial climate zone patterns, the Valdes et al. (2021) model yields significantly larger Continental (Da, Db and Dc/Dd) zones at high latitudes relative to our proxy reconstructions (Figs. SI87 and SI88). Additionally, the model predicts relatively widespread Polar (E) zones in Antarctica during the Berriasian-Valanginian and Hauterivian-Barremian, while our proxy reconstructions yield no Polar zones during the entirety of the Cretaceous. These colder climate zones are the result of the steeper latitudinal MAT gradient predicted by the model, as observed in our pole-to-equator temperature gradients discussed in the previous section. At lower latitudes, the Valdes et al. (2021) model predicts significantly more widespread Hot Desert climates in North America during Early Cretaceous relative to our proxy reconstructions. The model also predicts arid Desert and Steppe conditions along the central portion of the western margin of the Western Interior Seaway in

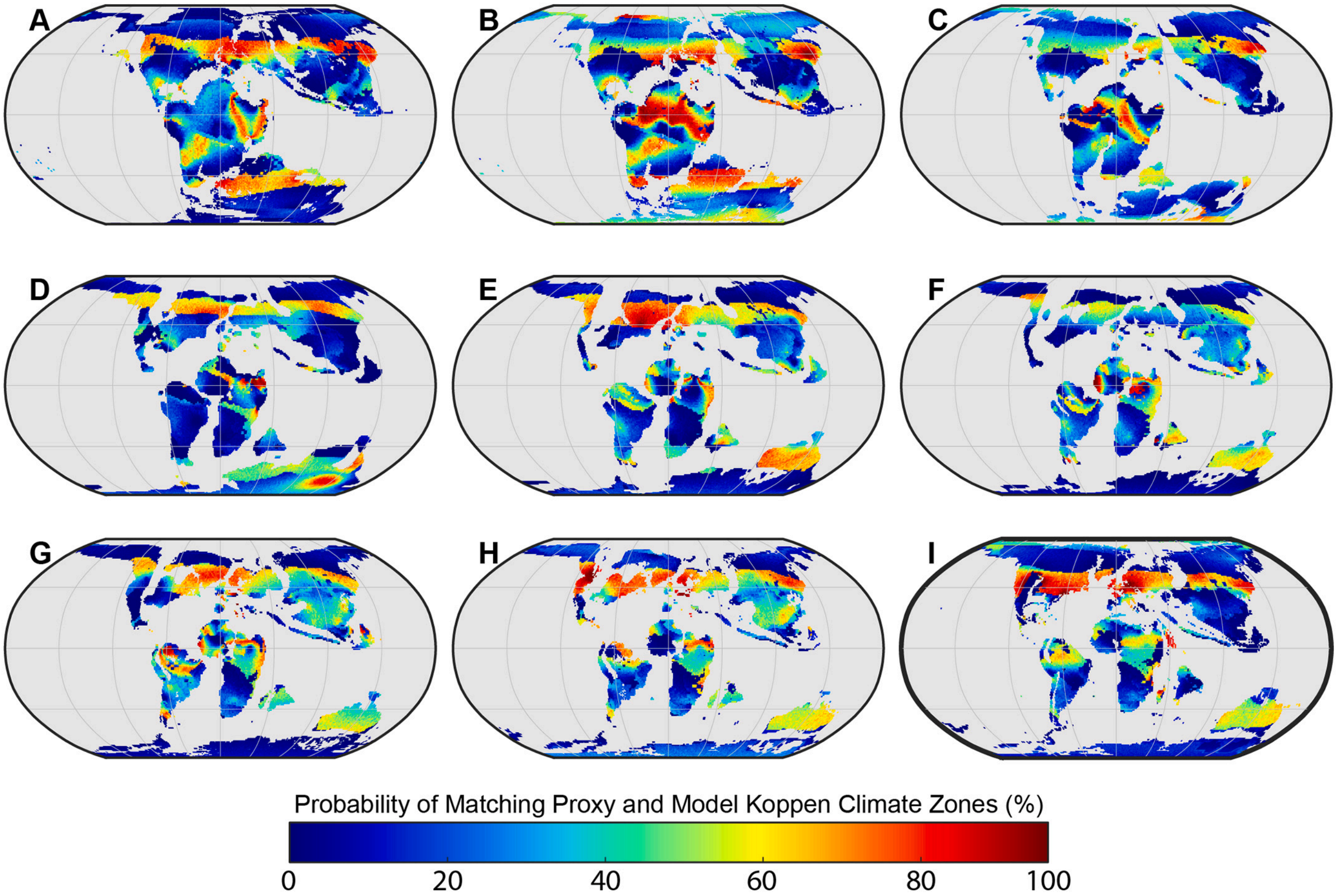

Fig. 20. Probability (in percentage) of the Valdes et al. (2021) model producing matching paleo-Köppen climate zones to the proxy-based climate zone reconstructions reported in this study, taking into account the uncertainties associated with the various climate proxies.

North America during the Albian and Maastrichtian—two periods for which there is ample evidence of more humid conditions in the presence of coal and lignite deposits.

While we recognize that some of the proxy-model mismatch is undoubtedly due to the relative scarcity of temperature and precipitation proxies for some analysis windows (e.g., the Berriasian-Valanginian) and locations (e.g., high latitude sites, south-central Africa, and central Australia during the Late Cretaceous), there are some times/locations where the model climate predictions are in direct contradiction to both quantitative reconstructions and lithologic climate indicators (e.g., bauxite and leaf physiognomy data from central Eurasia during the Albian to Turonian, and extensive coal deposits in western North America during the Maastrichtian). These discrepancies, and the observed systematic offsets between the proxy-based and model simulation pole-to-equator graphs, suggest that the “Equable Climate Problem” (Huber and Caballero, 2011) is still alive and well, and that despite significant advancements, global climate models still lack the ability to accurately simulate key aspects of greenhouse climate systems. One potential avenue forward is to employ new data assimilation techniques (e.g., Tierney et al., 2020; Judd et al., 2021a, 2021b; Annan et al., 2022) to combine proxy and model approaches to the Cretaceous climate system.

4.5. Critical areas for future development

While this work is a significant step forward in terms of proxy-based global reconstructions in past climate, there are a series of important targets for further development, including 1) adding new data to the base dataset to improve spatial and temporal resolution; 2) refining interpolation conditions, data treatment schemes (including updates to our treatment of older oxygen-isotope paleotemperature reconstructions), and Monte Carlo simulations to further constrain and minimize zone uncertainties; 3) introducing additional detail to paleo-DEM and paleocoastline base maps to enhance reconstruction output in complex/heterogeneous regions; and 4) directly linking zone predictions with paleoecological data both as a validation step and as a test of climate impacts hypotheses.

Specifically, some regions in our interpolation, such as Australia and Antarctica, exhibit limited change or heterogeneity across the Cretaceous as a result of limited data density and/or uncertain age determinations for existing data (Tables SI1-SI4). Any improvements in data density via new proxy reconstructions recovered from available Cretaceous sedimentary archives (e.g., Surat, Canning, and Perth basins, Australia; James Ross Basin, Antarctic Peninsula) would substantially improve spatial resolution, and revised or constrained ages for many of these successions could allow for more discrimination in terms of temporal binning, particularly improving interpolations for Southern Hemisphere high-latitude regions. In addition, some time periods suffer from limited available well-constrained data, which impacts resolution and requires additional temporal binning considerations (see *Section 2.2*; Table 1); the earliest Cretaceous (Berriasian - Barremian) is particularly data-poor and should be a high priority for future sampling and proxy application, especially given its potential to show Köppen zone shifts in the lead-up to an extended period of global warmth. Beyond the Cretaceous, other noteworthy climatic events with substantial proxy records should be high-priority targets for this interpolation framework as well, such as the oft-studied warming (e.g., Paleocene-Eocene Thermal Maximum; Korasidis et al., 2022) and cooling (e.g., Eocene-

Oligocene Transition; Tardif et al., 2021) events of the Paleogene.

Building on these interpolations, we also see great opportunity to pair ecological information with Köppen zone predictions in order to answer key questions about climatic drivers of ecological change and paleobiogeography, such as dinosaur provinciality or high-latitude habitability (e.g., Burgener et al., 2021; Chiarenza et al., 2019; Gates et al., 2022). Not only does this have potential to help answer key outstanding questions about climate impacts during the Cretaceous and other warm periods, but it also provides an important tool for testing paleontological hypotheses regarding the impact of climate and ecosystem change on the evolution and diversification of key terrestrial clades at multiple taxonomic levels.

5. Conclusions

This study presents newly updated Cretaceous proxy-based paleotemperature and paleoprecipitation databases that include both quantitative climate reconstructions and semi-quantitative (censored) climate indicators, as well as a new analytical methodology that utilizes spatial Bayesian statistics to calculate continuous global MAT, WMMT, and MAP fields from proxy data. We then employed the Zhang et al. (2016) paleo-Köppen climate classification system in order to create new, quantitative global climate zone maps for nine time slices across the Cretaceous, with associated uncertainties. These climate zone maps not only shed new light on temporal and spatial climate trends over the course of the Cretaceous, but provide a new foundation for future proxy-based studies of Cretaceous paleoclimate conditions specifically, and of greenhouse period climate dynamics more generally.

Our results confirm previous work suggesting that the Cretaceous was dominated by elevated global temperatures, reduced latitudinal temperature gradients, and an enhanced hydrologic cycle. Temporally, the Early and latest Cretaceous were characterized by cooler "warmhouse" conditions that bookended the extreme hothouse conditions of the mid-Cretaceous (Cenomanian-Turonian). Additionally, we use our new climate maps to show that 1) the Cretaceous equatorial humid belt (the ancient predecessor to the modern ITCZ) likely began developing during the Hauterivian-Barremian, nearly 20 million years earlier than most studies had previously suggested; and 2) global arid belts saw a distinct latitudinal widening over the course of the Cretaceous, and a general strengthening of the northern hemisphere arid belt, and weakening of the southern hemisphere arid belt.

A comparison of our proxy-based results with simulated findings show that climate models continue to struggle to reproduce the elevated high-latitude temperatures and reduced latitudinal temperature gradients characteristic of the Cretaceous, and that the models overestimate tropical terrestrial temperatures relative to our proxy-based reconstructions. An analysis of our MAP reconstructions suggest that the poleward transport of moisture and the associated movement of latent heat from the tropics to high latitudes may be a key Cretaceous climate process that models are not accurately capturing, as evidenced by the general underestimate of MAP at high latitudes in the model simulations, relative to our proxy-based MAP estimates.

The methods developed for this study are applicable to a wide range of time periods and climate states. We suggest that future work should focus on creating climate zone maps for the Early Cenozoic as well as other parts of the Mesozoic. Additionally, the paleoclimate information presented in this paper should provide a useful foundation for testing paleontological questions regarding the impact of climate on the behavior, diversity, and location of organisms.

Declaration of Competing Interest

The authors declare that they have no known competing financial interests or personal relationships that could have appeared to influence the work reported in this paper.

Data availability

Data will be made available on request.

Acknowledgements

This paper was funded by National Science Foundation Award 1925973 (E. Hyland). The authors thank the Paleo3 Research Group (North Carolina State University) for their suggestions and comments.

Appendix A. Supplementary data

Supplementary data to this article can be found online at https://doi.org/10.1016/j.palaeo.2022.111373.

References

Amiot, R., Lécuyer, C., Buffetaut, E., Fluteau, F., Legendre, S., Martineau, F., 2004. Latitudinal temperature gradient during the Cretaceous Upper Campanian-Middle Maastrichtian: δ18O record of continental vertebrates. Earth Planet. Sci. Lett. 226, 255–272. https://doi.org/10.1016/j.epsl.2004.07.015.

Amiot, R., Wang, X., Zhou, Z., Wang, X., Lécuyer, C., Buffetaut, E., Fluteau, F., Ding, Z., Kusuhashi, N., Mo, J., Philippe, M., Suteethorn, V., Wang, Y., Xu, X., 2015. Environment and ecology of East Asian dinosaurs during the Early Cretaceous inferred from stable oxygen and carbon isotopes in apatite. J. Asian Earth Sci. 98, 358–370. https://doi.org/10.1016/j.jseaes.2014.11.032.

Anderson, T., Arthur, M., 1983. Stable isotopes of oxygen and carbon and their application to sedimentologic and paleoenvironmental problems. In: Arthur, M., Anderson, T., Kaplan, I., Veizer, J., Land, L. (Eds.), SEPM SHORT COURSE NOTES: Stable Isotopes in Sedimentary Geology. SEPM Society for Sedimentary Geology, pp. 1.1–1.151. https://doi.org/10.2110/scn.83.10.

Andrezejewski, K., 2018. Cretaceous dinosaurs and the world they lived in: a new species of ornithischian dinosaur from the early Cretaceous (Aptian) of Texas. In: Reconstruction of the Brain Endocast and Inner Ear of Malawisaurus Dixeyi, And Reconstruction of The Paleoclimate and Pa. Southern Methodist University.

Annan, J.D., Hargreaves, J.C., Mauritsen, T., 2022. A new global surface temperature reconstruction for the Last Glacial Maximum. Clim. Past v. 18, 1883–1896. https://doi.org/10.5194/cp-18-1883-2022.

Arias, P.A., Bellouin, N., Coppola, E., Jones, R.G., Krinner, G., Marotzke, J., Naik, V., Palmer, M.D., Plattner, G.K., Rogelj, J., Rojas, M., Sillmann, J., Storelvmo, T., Thorne, P.W., Trewin, B., Achuta Rao, K., Adhikary, B., Allan, R.P., Armour, K., Zickfeld, K., 2021. Technical summary. In: Zhai, P., Pirani, A., Connors, S.L., Péan, C., Berger, S., Caud, N., Chen, Y., Goldfarb, L., Gomis, M.I., Huang, M., Leitzell, K., Lonnoy, E., Matthews, J.B.R., Maycock, T.K., Waterfield, T., Yelekçi, O., Yu, R., Zhou, B. (Eds.), Climate Change 2021: The Physical Science Basis. Contribution of Working Group I to the Sixth Assessment Report of the Intergovernmental Panel on Climate Change. Cambridge University Press, pp. 33–144. https://doi.org/10.1017/9781009157896.002.

Barron, E.J., Hay, W.W., Thompson, S., 1989. The hydrologic cycle: A major variable during earth history. Palaeogeogr. Palaeoclimatol. Palaeoecol. 75 (3), 157–174. https://doi.org/10.1016/0031-0182(89)90175-2.

Beck, H.E., Zimmermann, N.E., McVicar, T.R., Vergopolan, N., Berg, A., Wood, E.F., 2018. Present and future köppen-geiger climate classification maps at 1-km resolution. Sci. Data 5. https://doi.org/10.1038/sdata.2018.214.

Berry, J., Bjorkman, O., 1980. Photosynthetic response and adaptation to temperature in higher plants. Annu. Rev. Plant Physiol. 31 (1), 491–543. https://doi.org/10.1146/annurev.pp.31.060180.002423.

Bijl, P.K., Schouten, S., Sluijs, A., Reichart, G.J., Zachos, J.C., Brinkhuis, H., 2009. Early palaeogene temperature evolution of the southwest Pacific Ocean. Nature 461, 776–779. https://doi.org/10.1038/nature08399.

Bornemann, A., Norris, R., Friedrich, O., Beckmann, B., Schouten, S., Damste, J., Vogel, J., Hofmann, P., Wagner, T., 2008. Isotopic evidence for glaciation during the Cretaceous Supergreenhouse. Science 319, 189–192.

Boucot, A.J., Chen, Xu, Scotese, C.R., 2013. Phanerozoic Paleoclimate: An Atlas of Lithologic Indicators of Climate, SEPM Concepts in Sedimentology and Paleontology, (Print-on-Demand Version), No. 11, 478 p, ISBN 978-1-56576-289-3. October 2013. Society for Sedimentary Geology, Tulsa, OK.

Boyce, C.K., Brodribb, T.J., Feild, T.S., Zwieniecki, M.A., 2009. Angiosperm leaf vein evolution was physiologically and environmentally transformative. Proc. R. Soc. B Biol. Sci. 276 (1663), 1771–1776. https://doi.org/10.1098/rspb.2008.1919.

Boyce, C.K., Lee, J.E., Feild, T.S., Brodribb, T.J., Zwieniecki, M.A., 2010. Angiosperms helped put the rain in the rainforests: The impact of plant physiological evolution on tropical biodiversity. Ann. Mo. Bot. Gard. 97 (4), 527–540. https://doi.org/10.3417/2009143.

Burgener, L., Hyland, E., Griffith, E., Mitášová, H., Zanno, L.E., Gates, T.A., 2021. An extreme climate gradient-induced ecological regionalization in the Upper Cretaceous Western Interior Basin of North America. Bull. Geol. Soc. Am. 133 (9–10), 2125–2136. https://doi.org/10.1130/B35904.1.

Cao, W., Williams, S., Flament, N., Zahirovic, S., Scotese, C., Müller, R.D., 2019. Palaeolatitudinal distribution of lithologic indicators of climate in a palaeogeographic framework. Geol. Mag. 156 (2), 331–354. https://doi.org/10.1017/S0016756818000110.

Carmichael, M.J., Lunt, D.J., Huber, M., Heinemann, M., Kiehl, J., Legrande, A., Loptson, C.A., Roberts, C.D., Sagoo, N., Shields, C., Valdes, P.J., Winguth, A., Winguth, C., Pancost, R.D., 2015. Insights into the early Eocene hydrological cycle Insights into the early Eocene hydrological cycle from an ensemble of atmosphere-ocean GCM simulations Insights into the early Eocene hydrological cycle. Clim. Past Discuss. 11, 3277–3339. https://doi.org/10.5194/cpd-11-3277-2015.

Chandra, R., Cripps, S., Butterworth, N., Muller, R.D., 2021. Precipitation reconstruction from climate-sensitive lithologies using Bayesian machine learning. Environ. Model. Softw. 139, 105002 https://doi.org/10.1016/j.envsoft.2021.105002.

Chen, D., Chen, H.W., 2013. Using the Köppen classification to quantify climate variation and change: An example for 1901-2010. Environ. Dev. 6 (1), 69–79. https://doi.org/10.1016/j.envdev.2013.03.007.

Chiarenza, A.A., Mannion, P.D., Lunt, D.J., Farnsworth, A., Jones, L.A., Kelland, S.J., Allison, P.A., 2019. Ecological niche modelling does not support climatically-driven dinosaur diversity decline before the Cretaceous/Paleogene mass extinction. Nature Commun 10 (1), 1–14.

Chumakov, N.M., Zharkov, M.A., Herman, A.B., Doludenko, M.P., Kalandadze, N.N., Lebedev, E.L., Ponomarenko, A.G., Rautian, A.S., 1995. Climatic Belts of the Mid-Cretaceous Time. Stratigr. Geol. Correl. 3 (3), 241–260.

Cressie, N., Wikle, C., 2011. Statistics for Spatio-Temporal Data: Hoboken, New Jersey. John Wiley & Sons, Inc.

Du Toit, A.L., 1937. Our Wandering Continents : An Hypothesis of Continental Drifting (Oliver & Boyd (eds.)).

Dutra, E., Muñoz-Sabater, J., Boussetta, S., Komori, T., Hirahara, S., Balsamo, G., 2020. Environmental lapse rate for high-resolution land surface downscaling: an application to ERA5. Earth Space Sci. 7 https://doi.org/10.1029/2019EA000984.

Eiler, J.M., 2011. Paleoclimate reconstruction using carbonate clumped isotope thermometry. Quat. Sci. Rev. 30 (25–26), 3575–3588. https://doi.org/10.1016/j.quascirev.2011.09.001.

El-Shazly, S., Košťák, M., Abdel-Gawad, G., Kloukčová, B., Saber, S.G., Salama, Y.F., Žák, K., 2011. Carbon and oxygen stable isotopes of selected Cenomanian and Turonian rudists from Egypt and Czech Republic, and a note on changes in rudist diversity. Bull. Geoscie. 86 (2), 209–226.

Emiliani, C., 1954. Depth habitats of some species of pelagic foraminifera as indicated by oxygen isotope ratios. Am. J. Sci. 252 (3), 149–158.

Erez, J., Luz, B., 1983. Experimental paleotemperature equation for planktonic foraminifera. Geochim. Cosmochim. Acta 47, 1025–1031.

Feng, R., Poulsen, C.J., 2016. Refinement of Eocene lapse rates, fossil-leaf altimetry, and North American Cordilleran surface elevation estimates. Earth Planet. Sci. Lett. 436, 130–141. https://doi.org/10.1016/j.epsl.2015.12.022.

Ferguson, K.M., Gregory, R.T., Constantine, A., 1999. Lower Cretaceous (Aptian-Albian) secular changes in the oxygen and carbon isotope record from high paleolatitude, fluvial sediments, southeast Australia: Comparisons to the marine record. SPECIAL PAPERS-GEOLOGICAL SOCIETY OF AMERICA,, 59–72.

Frakes, L.A., 1979. Climates Through Geologic Time. Elsevier.

Frakes, L.A., Francis, J.E., Syktus, J.I., 1992. Climate Modes of the Phanerozoic. Cambridge University Press.

Gaskell, D.E., Huber, M., O'Brien, C.L., Inglis, G.N., Acosta, R.P., Poulsen, C.J., Hull, P. M., 2022. The latitudinal temperature gradient and its climate dependence as inferred from foraminiferal δ 18 O over the past 95 million years. Proc. Natl. Acad. Sci. 119 (11) https://doi.org/10.1073/pnas.2111332119.

Gates, T.A., Cai, H., Hu, Y., Han, X., Griffith, E., Burgener, L., Hyland, E., Zanno, L.E., 2022. Estimating ancient biogeographic patterns with statistical model discrimination. Anat. Rec. https://doi.org/10.1002/ar.25067.

Gill, E.C., Rajagopalan, B., Molnar, P., Marchitto, T.M., 2016. Reduced-dimension reconstruction of the equatorial Pacific SST and zonal wind fields over the past 10,000 years using Mg/Ca and alkenone records. Paleoceanography 31 (7), 928–952. https://doi.org/10.1002/2016PA002948.

Goswami, A., 2012. Predicting the geographic distribution of ancient soils with special reference to the Cretaceous..

Gradstein, F.M., Ogg, J.G., Schmitz, M., Ogg, G. (Eds.), 2020. Geological Time Scale 2020, 2. Elsevier.

Grossman, E.L., 2012a. Applying Oxygen Isotope Paleothermometry in Deep Time. In: Ivany, L., Huber, B. (Eds.), Reconstructing Earth's Deep-Time Climate: State of the Art in 2012, Paleontological Society Short Course, 18. The Paleontological Society Papers, pp. 39–67.

Grossman, E.L., 2012b. Oxygen Isotope Stratigraphy. In: Gradstein, F.M., Ogg, J.G., Schmitz, M.D., Ogg, G.M. (Eds.), The Geologic Time Scale 2012, 1. Elsevier, pp. 181–206.

Grossman, E.L., Joachimski, M.M., 2020. Oxygen Isotope Stratigraphy. In: Geologic Time Scale 2020. Elsevier, pp. 279–307. https://doi.org/10.1016/B978-0-12-824360-2.00010-3.

Grossman, E.L., Joachimski, M.M., 2022. Ocean temperatures through the Phanerozoic reassessed. Sci. Rep. 12 (1), 8938. https://doi.org/10.1038/s41598-022-11493-1.

Habicht, J.K.A., 1979. Paleoclimate, Paleomagnetism, and Continental Drift, AAPG Studies in Geology No. 9. American Association of Petroleum Geologists.

Hall, Tracy, L., 2005. Paleoenvironmental Reconstruction of the Late Cretaceous Eastern Gulf Coastal Plain in. Columbus State University, Georgia and Alabama. http://archive.org/details/paleoenvironmentOOhall.

Haq, B.U., 2014. Cretaceous eustasy revisited. In: Global and Planetary Change (Vol. 113, pp. 44–58). https://doi.org/10.1016/j.gloplacha.2013.12.007.

Harper, D.T., Suarez, M.B., Uglesich, J., You, H., Li, D., Dodson, P., 2020. Aptian-Albian clumped isotopes from northwest China: Cool temperatures, variable atmospheric pCO2 and regional shifts in hydrologic cycle. Clim. Past Discuss. 17 (4), 1–29. https://doi.org/10.5194/cp-2020-152.

Hasegawa, H., Tada, R., Jiang, X., Suganuma, Y., Imsamut, S., Charusiri, P., Ichinnorov, N., Khand, Y., 2012. Drastic shrinking of the Hadley circulation during the mid-Cretaceous Supergreenhouse. Clim. Past 8 (4), 1323–1337. https://doi.org/10.5194/cp-8-1323-2012.

Hay, W.W., Floegel, S., 2012. New thoughts about the Cretaceous climate and oceans. In: Earth-Science Reviews (Vol. 115, Issue 4, pp. 262–272). https://doi.org/10.1016/j.earscirev.2012.09.008.

Hay, W.W., DeConto, R.M., de Boer, P., Flögel, S., Song, Y., Stepashko, A., 2019. Possible solutions to several enigmas of Cretaceous climate. Int. J. Earth Sci. 108 (2), 587–620. https://doi.org/10.1007/s00531-018-1670-2.

Haywood, A.M., Valdes, P.J., Aze, T., Barlow, N., Burke, A., Dolan, A.M., von der Heydt, A.S., Hill, D.J., Jamieson, S.S.R., Otto-Bliesner, B.L., Salzmann, U., Saupe, E., Voss, J., 2019. What can Palaeoclimate Modelling do for you? Earth Syst. Environ. 3 (1), 1–18. https://doi.org/10.1007/s41748-019-00093-1.

Held, I.M., Soden, B.J., 2006. Robust responses of the hydrological cycle to global warming. J. Clim. 19 (21), 5686–5699. https://doi.org/10.1175/JCLI3990.1.

Ho, S.L., Mollenhauer, G., Fietz, S., Martínez-Garcia, A., Lamy, F., Rueda, G., Schipper, K., Méheust, M., Rosell-Melé, A., Stein, R., Tiedemann, R., 2014. Appraisal of TEX86 and TEX86L thermometries in subpolar and polar regions. Geochim. Cosmochim. Acta 131, 213–226. https://doi.org/10.1016/j.gca.2014.01.001.

Hollis, C.J., Dunkley Jones, T., Anagnostou, E., Bijl, P.K., Cramwinckel, M.J., Cui, Y., Dickens, G.R., Edgar, K.M., Eley, Y., Evans, D., Foster, G.L., Frieling, J., Inglis, G.N., Kennedy, E.M., Kozdon, R., Lauretano, V., Lear, C.H., Littler, K., Lourens, L., Lunt, D. J., 2019. The DeepMIP contribution to PMIP4: Methodologies for selection, compilation and analysis of latest Paleocene and early Eocene climate proxy data, incorporating version 0.1 of the DeepMIP database. In: Geoscientific Model Development (Vol. 12, Issue 7, pp. 3149–3206). Copernicus GmbH. https://doi.org/10.5194/gmd-12-3149-2019.

Hollis, C.J., Taylor, K.W., Handley, L., Pancost, R.D., Huber, M., Creech, J.B., Zachos, J. C., 2012. Early Paleogene temperature history of the Southwest Pacific Ocean: Reconciling proxies and models. Earth Planet. Sci. Lett. 349, 53–66.

Huber, M., 2012. Progress in greenhouse climate modeling. In: Ivany, L., Huber, B. (Eds.), Reconstructing Earth's Deep-Time Climate – The State of the Art in 2012, Paleontological Society Short Course, Volume 18. Paleontological Society Papers, pp. 213–262.

Huber, M., Caballero, R., 2011. The early Eocene equable climate problem revisited. Clim. Past 7 (2), 603–633. https://doi.org/10.5194/cp-7-603-2011.

Hutchinson, D.K., De Boer, A.M., Coxall, H.K., Caballero, R., Nilsson, J., Baatsen, M., 2018. Climate sensitivity and meridional overturning circulation in the late Eocene using GFDL CM2.1. Clim. Past 14 (6), 789–810. https://doi.org/10.5194/cp-14-789-2018.

Hutchinson, D.K., Coxall, H.K., Oregan, M., Nilsson, J., Caballero, R., de Boer, A.M., 2019. Arctic closure as a trigger for Atlantic overturning at the Eocene-Oligocene Transition. Nat. Commun. 10 (1) https://doi.org/10.1038/s41467-019-11828-z.

Hutchinson, D.K., Coxall, H.K., Lunt, D.J., Steinthorsdottir, M., De Boer, A.M., Baatsen, M., Von Der Heydt, A., Huber, M., Kennedy-Asser, A.T., Kunzmann, L., Ladant, J.B., Lear, C.H., Moraweck, K., Pearson, P.N., Piga, E., Pound, M.J., Salzmann, U., Scher, H.D., Sijp, W.P., Zhang, Z., 2021. The Eocene-Oligocene transition: A review of marine and terrestrial proxy data, models and model-data comparisons. In: Climate of the Past (Vol. 17, Issue 1, pp. 269–315). Copernicus GmbH. https://doi.org/10.5194/cp-17-269-2021.

Hüve, K., Bichele, I., Rasulov, B., Niinemets, Ü., 2011. When it is too hot for photosynthesis: Heat-induced instability of photosynthesis in relation to respiratory burst, cell permeability changes and H2O2 formation. Plant Cell Environ. 34 (1), 113–126. https://doi.org/10.1111/j.1365-3040.2010.02229.x.

Hyland, E.G., Sheldon, N.D., 2016. Examining the spatial consistency of palaeosol proxies: Implications for palaeoclimatic and palaeoenvironmental reconstructions in terrestrial sedimentary basins. Sedimentology 63 (4), 959–971. https://doi.org/10.1111/sed.12245.

Hyland, E.G., Sheldon, N.D., Van der Voo, R., Badgley, C., Abrajevitch, A., 2015. A new paleoprecipitation proxy based on soil magnetic properties: Implications for expanding paleoclimate reconstructions. Bull. Geol. Soc. Am. 127 (7–8), 975–981. https://doi.org/10.1130/B31207.1.

Judd, E.J., Tierney, J.E., Huber, B.T., Wing, S.L., Lunt, D.J., 2021a. The Phanerozoic Technique Averaged Surface Temperature Integrated Curve: A record of Phanerozoic global mean surface temperature using data assimilation. In: AGU Fall Meeting.

Judd, E., Tierney, J., Huber, B., Wing, S., Lunt, D., 2021b. The Phanerozoic Technique Averaged Surface Temperature Integrated Curve: A record of Phanerozoic global mean surface temperature using data assimilation. In: AGU Fall Meeting 2021. , December 13.

Kargel, J.S., Leonard, G.J., Bishop, M.P., Kaab, A., Raup, B., (Eds.), 2014. Global land ice measurements from space. Springer-Praxis.

Karger, D.N., Conrad, O., Böhner, J., Kawohl, T., Kreft, H., Soria-Auza, R.W., Zimmermann, N.E., Linder, H.P., Kessler, M., 2017. Climatologies at high resolution for the earth's land surface areas. Sci. Data 4. https://doi.org/10.1038/sdata.2017.122.

Karger, D.N., Conrad, O., Böhner, J., Kawohl, T., Kreft, H., Soria-Auza, R.W., Zimmermann, N.E., Linder, H.P., Kessler, M., 2018. Data from: climatologies at high resolution for the earth's land surface areas. In: Dryad Digital Repository.

Kennett, J., Shackleton, N., 1975. Laurentide ice sheet meltwater recorded in Gulf of Mexico Deep-Sea Cores. Science 188, 147–150.

Köppen, W., 1936. Das geographisca System der Klimate. In: Köppen, W., Gieger, G. (Eds.), Handbuch der Klimatologie, 1. Gebrüder Borntraeger, pp. 1–44.

Korasidis, V.A., Wing, S.L., Shields, C.A., Kiehl, J.T., 2022. Global changes in terrestrial vegetation and continental climate during the paleocene-eocene thermal maximum. Paleoceanogr. Paleoclimatol. 37 (4) https://doi.org/10.1029/2021PA004325.

Kump, L.R., Pollard, D., 2008. Amplification of Cretaceous warmth by biological cloud feedbacks. Science 320 (2), 195. https://doi.org/10.1029/2005PA001203.

Ladant, J.B., Donnadieu, Y., 2016. Palaeogeographic regulation of glacial events during the Cretaceous supergreenhouse. Nat. Commun. 7 https://doi.org/10.1038/ncomms12771.

Lawrimore, J.H., Menne, M.J., Gleason, B.E., Williams, C.N., Wuertz, D.B., Vose, R.S., Rennie, J., 2011. Global Historical Climatology Network - Monthly (GHCN-M), Version 3. NOAA National Centers for Environmental Information.

Legates, D.R., Willmott, C.J., 1990. Mean seasonal and spatial variability in global surface air temperature. Theor. Appl. Climatol. 41 (1–2), 11–21. https://doi.org/10.1007/BF00866198.

Li, X., Hu, Y., Guo, J., Lan, J., Lin, Q., Bao, X., Yuan, S., Wei, M., Li, Z., Man, K., Yin, Z., Han, J., Zhang, J., 2022. A high-resolution climate simulation dataset for the past 540 million years. Sci. Data 9. https://doi.org/10.1038/s41597-022-01490-4.

Lunt, D.J., Huber, M., Anagnostou, E., Baatsen, M.L.J., Caballero, R., DeConto, R., Dijkstra, H.A., Donnadieu, Y., Evans, D., Feng, R., Foster, G.L., Gasson, E., Von Der Heydt, A.S., Hollis, C.J., Inglis, G.N., Jones, S.M., Kiehl, J., Turner, S.K., Korty, R.L., Zeebe, R.E., 2017. The DeepMIP contribution to PMIP4: experimental design for model simulations of the EECO, PETM, and pre-PETM (version 1.0). Geosci. Model Dev. 10 (2), 889–901. https://doi.org/10.5194/gmd-10-889-2017.

Lunt, D.J., Bragg, F., Chan, W., Hutchinson, D.K., Ladant, J.B., Morozova, P., Niezgodzki, I., Steinig, S., Zhang, Z., Zhu, J., Abe-Ouchi, A., Anagnostou, E., De Boer, A.M., Coxall, H.K., Donnadieu, Y., Foster, G., Inglis, G.N., Knorr, G., Langebroek, P.M., Otto-Bliesner, B.L., 2021. DeepMIP: Model intercomparison of early Eocene climatic optimum (EECO) large-scale climate features and comparison with proxy data. Clim. Past 17 (1), 203–227. https://doi.org/10.5194/cp-17-203-2021.

Markwick, P.J., 2007. The palaeogeographic and palaeoclimatic significance of climate proxies for data-model comparisons. In: Williams, M., Haywood, A.M., Gregory, F.J., Schmidt, D.N. (Eds.), Deep-Time perspectives on climate change: marrying the signal from computer models and biological proxies. Geological Society of Londond, pp. 251–312.

Masse, J.-P., Fenerci-Masse, M., 2008. Time contrasting palaeobiogeographies among Hauterivian–Lower Aptian rudist bivalves from the Mediterranean Tethys, their climatic control and palaeoecological implications. Palaeogeogr. Palaeoclimatol. Palaeoecol. 269 (1–2), 54–65. https://doi.org/10.1016/j.palaeo.2008.07.024.

Menne, M.J., Williams, C.N., Gleason, B.E., Jared Rennie, J., Lawrimore, J.H., 2018. The global historical climatology network monthly temperature dataset, version 4. J. Clim. 31 (24), 9835–9854. https://doi.org/10.1175/JCLI-D-18-0094.1.

Miller, I.M., Brandon, M.T., Hickey, L.J., 2006. Using leaf margin analysis to estimate the mid-Cretaceous (Albian) paleolatitude of the Baja BC block. Earth Planet. Sci. Lett. 245 (1–2), 95–114.

Mills, B.J.W., Krause, A.J., Scotese, C.R., Hill, D.J., Shields, G.A., Lenton, T.M., 2019. Modelling the long-term carbon cycle, atmospheric CO2, and Earth surface temperature from late Neoproterozoic to present day. Gondwana Res. 67, 172–186. https://doi.org/10.1016/j.gr.2018.12.001.

Müller, R.D., Cannon, J., Qin, X., Watson, R.J., Gurnis, M., Williams, S., Pfaffelmoser, T., Seton, M., Russell, S.H.J., Zahirovic, S., 2018. GPlates: building a virtual earth through deep time. Geochem. Geophys. Geosyst. 19 (7), 2243–2261. https://doi.org/10.1029/2018GC007584.

Niezgodzki, I., Knorr, G., Lohmann, G., Tyszka, J., Markwick, P.J., 2017. Late Cretaceous climate simulations with different CO2 levels and subarctic gateway configurations: A model-data comparison. Paleoceanography 32 (9), 980–998. https://doi.org/10.1002/2016PA003055.

O'Brien, C.L., Robinson, S.A., Pancost, R.D., Sinninghe Damsté, J.S., Schouten, S., Lunt, D.J., Alsenz, H., Bornemann, A., Bottini, C., Brassell, S.C., Farnsworth, A., Forster, A., Huber, B.T., Inglis, G.N., Jenkyns, H.C., Linnert, C., Littler, K., Markwick, P., McAnena, A., Wrobel, N.E., 2017. Cretaceous sea-surface temperature evolution: Constraints from TEX86 and planktonic foraminiferal oxygen isotopes. In: Earth-Science Reviews, 172. Elsevier B.V, pp. 224–247. https://doi.org/10.1016/j.earscirev.2017.07.012.

Parrish, J.T., 1998. Interpreting Pre-Quaternary Climate from the Geologic Record. Columbia University Press.

Parrish, J.T., Ziegler, A.M., Scotese, C.R., 1982. Rainfall patterns and the distribution of coals and evaporites in the Mesozoic and Cenozoic. Palaeogeogr. Palaeoclimatol. Palaeoecol. 40 (1–3), 67–101. https://doi.org/10.1016/0031-0182(82)90085-2.

Peel, M.C., Finlayson, B.L., Mcmahon, T.A., 2007. Hydrology and Earth system sciences updated world map of the Köppen-Geiger climate classification. Hydrol. Earth Syst. Sci. 11, 1633–1644. www.hydrol-earth-syst-sci.net/11/1633/2007/.

Peppe, D.J., Royer, D.L., Cariglino, B., Oliver, S.Y., Newman, S., Leight, E., Enikolopov, G., Fernandez-Burgos, M., Herrera, F., Adams, J.M., Correa, E., Currano, E.D., Erickson, J.M., Hinojosa, L.F., Hoganson, J.W., Iglesias, A., Jaramillo, C.A., Johnson, K.R., Jordan, G.J., Wright, I.J., 2011. Sensitivity of leaf size and shape to climate: global patterns and paleoclimatic applications. New Phytol. 190 (3), 724–739. https://doi.org/10.1111/j.1469-8137.2010.03615.x.

Pirrie, D., Doyle, P., Marshall, J.D., Ellis, G., 1995. Cool Cretaceous climates: new data from the Albian of Western Australia. J. Geol. Soc. Lond. 152, 739–742. https://doi.org/10.1144/gsjgs.152.5.0739.

Pirrie, D., Marshall, J.D., Doyle, P., Riccardi, A.C., 2004. Cool early Albian climates; new data from Argentina. Cretac. Res. 25, 27–33. https://doi.org/10.1016/j.cretres.2003.10.002.

Polik, C.A., Elling, F.J., Pearson, A., 2018. Impacts of paleoecology on the TEX 86 sea surface temperature proxy in the Pliocene-Pleistocene Mediterranean Sea. Paleoceanogr. Paleoclimatol. 33 (12), 1472–1489. https://doi.org/10.1029/2018PA003494.

Poulsen, C.J., Pollard, D., White, T.S., 2007. General circulation model simulation of the δ18O content of continental precipitation in the middle Cretaceous: a model-proxy comparison. Geology 35 (3), 199–202. https://doi.org/10.1130/G23343A.1.

Price, G.D., Ruffell, A.H., Jones, C.E., Kalin, R.M., Mutterlose, J., 2000. Isotopic evidence for temperature variation during the early Cretaceous (late Ryazanian–mid-Hauterivian). J. Geol. Soc. 157 (2), 335–343. https://doi.org/10.1144/jgs.157.2.335.

Price, G.D., Williamson, T., Henderson, R.A., Gagan, M.K., 2012. Barremian-Cenomanian palaeotemperatures for Australian seas based on new oxygen-isotope data from belemnite rostra. Palaeogeogr. Palaeoclimatol. Palaeoeco. 358–360, 27–39. https://doi.org/10.1016/j.palaeo.2012.07.015.

Quadrennial Defense Review Report (QDRR), 2010. Crafting a Strategic Approach to Climate.

Rees, P.M., Ziegler, A.M., Valdes, P.J., 2000. Jurassic phytogeography and climates: new data and model comparisons. In: Huber, B.T., Macleod, K.G., Wing, S.L. (Eds.), Warm Climates in Earth History. Cambridge University Press, pp. 297–318. https://doi.org/10.1017/cbo9780511564512.011.

Rees, P.M., Ziegler, A.M., Gibbs, M.T., John, E., Behling, P.J., Rowley, D.B., 2002. Permian phytogeographic patterns and climate data / model comparisons. J. Geol. 110 (January), 1–31.

Reichgelt, T., West, C.K., Greenwood, D.R., 2018. The relation between global palm distribution and climate. Sci. Rep. 8 (1) https://doi.org/10.1038/s41598-018-23147-2.

Rogov, M., Ershova, V., Vereshchagin, O., Vasileva, K., Mikhailova, K., Krylov, A., 2021. Database of global glendonite and ikaite records throughout the Phanerozoic. Earth Syst. Sci. Data 13 (2), 343–356.

Rose, B.E.J., Ferreira, D., 2013. Ocean heat transport and water vapor greenhouse in a warm equable climate: A new look at the low gradient paradox. J. Clim. 26 (6), 2117–2136. https://doi.org/10.1175/JCLI-D-11-00547.1.

Royer, D.L., Berner, R.A., Montañez, I.P., Tabor, N.J., Beerling, D.J., 2004. CO2 as a primary driver of Phanerozoic climate. GSA Today 14 (3), 4. https://doi.org/10.1130/1052-5173(2004)014<4:CAAPDO>2.0.CO;2.

Santos, A., De Lira Mota, M.A., Kern, H.P., Fauth, G., Paim, P.S.G., Netto, R.G., Sedorko, D., Lavina, E.L.C., Krahl, G., Fallgatter, C., Silveira, D.M., Aquino, C.D., Santos, M.O., do., Baecker-Fauth, S., & Vieira, C. E. L., 2022. Earlier onset of the Early Cretaceous Equatorial humidity belt. Glob. Planet. Chang. 208 https://doi.org/10.1016/j.gloplacha.2021.103724.

Schouten, S., Forster, A., Panoto, F.E., Damste, J.S.S., 2007. Towards calibration of the TEX86 palaeothermometer for tropical sea surface temperatures in ancient greenhouse worlds. Org. Geochem. 38, 1537–1546. https://doi.org/10.1029/2004PA001041.

Scotese, C.R., 2016. PALEOMAP PaleoAtlas for GPlates and the PaleoData Plotter Program Tutorial, PALEOMAP Project. https://doi.org/10.13140/RG.2.2.34367.00166.

Scotese, C.R., 2021. An Atlas of Phanerozoic Paleogeographic Maps: The Seas Come In and the Seas Go Out. Annu. Rev. Earth Planet. Sci. 49 (1), 679–728. https://doi.org/10.1146/annurev-earth-081320-064052.

Scotese, C.R., 2022. Global Mean Surface Temperatures for 100 Phanerozoic Time Intervals (dataset). https://doi.org/10.5281/zenodo.5718392.

Scotese, C.R., Wright, N., 2018. PALEOMAP Paleodigital Elevation Models (PaleoDEMS) for the Phanerozoic. https://www.earthbyte.org/paleodem-resource-scotese-and-wright-2018/.

Scotese, C.R., Song, H., Mills, B.J.W., van der Meer, D.G., 2021. Phanerozoic paleotemperatures: The earth's changing climate during the last 540 million years. Earth Sci. Rev. 215, 103503 https://doi.org/10.1016/j.earscirev.2021.103503.

Sellwood, B.W., Price, G.D., 1994. Sedimentary facies as indicators of Mesozoic palaeoclimate. In: Allen, J.R.L., Hoslins, B.J., Sellwood, B.W., Spicer, R.A., Valdes, P.J. (Eds.), Palaeoclimates and their Modelling, with Special Reference to the Mesozoic Era. Chapman & Hall, London, pp. 17–25.

Sewall, J.O., Fricke, H.C., 2013. Andean-scale highlands in the Late Cretaceous Cordillera of the North American western margin. Earth Planet. Sci. Lett. 362, 88–98. https://doi.org/10.1016/j.epsl.2012.12.002.

Sharkey, T.D., 2000. Some like it hot. In: Science (Vol. 287, Issue 5452, pp. 435–437). https://doi.org/10.1126/science.287.5452.435.

Sheldon, N.D., Tabor, N.J., 2009. Quantitative paleoenvironmental and paleoclimatic reconstruction using paleosols. Earth Sci. Rev. 95 (1–2), 1–52. https://doi.org/10.1016/j.earscirev.2009.03.004.

Sheldon, N.D., Retallack, G.J., Tanaka, S., 2002. Geochemical climofunctions from North American soils and application to paleosols across the Eocene-Oligocene boundary in Oregon. J. Geol. 110 (6), 687–696. https://doi.org/10.1086/342865.

Skea, et al., 2022. Mitigation of Climate Change Summary for Policymakers Climate Change 2022 Working Group III contribution to the Sixth Assessment Report of the Intergovernmental Panel on Climate Change. https://www.researchgate.net/publication/359746855.

Sluijs, A., et al., 2006. Subtropical Arctic Ocean temperatures during the Palaeocene/Eocene thermal maximum. Nature 441, 610–613. https://doi.org/10.1038/nature04668.

Song, H., Wignall, P.B., Song, H., Dai, X., Chu, D., 2019. Seawater Temperature and Dissolved Oxygen over the Past 500 Million Years. J. Earth Sci. 30 (2), 236–243. https://doi.org/10.1007/s12583-018-1002-2.

Spicer, R.A., Herman, A.B., 2010. The Late Cretaceous environment of the Arctic: A quantitative reassessment based on plant fossils. Palaeogeogr. Palaeoclimatol. Palaeoecol. 295 (3–4), 423–442. https://doi.org/10.1016/j.palaeo.2010.02.025.

Spicer, R.A., Ahlberg, A., Herman, A.B., Hofmann, C.C., Raikevich, M., Valdes, P.J., Markwick, P.J., 2008. The Late Cretaceous continental interior of Siberia: A challenge for climate models. Earth Planet. Sci. Lett. 267 (1–2), 228–235. https://doi.org/10.1016/j.epsl.2007.11.049.

Spicer, R.A., Valdes, P.J., Spicer, T.E.V., Craggs, H.J., Srivastava, G., Mehrotra, R.C., Yang, J., 2009. New developments in CLAMP: Calibration using global gridded meteorological data. Palaeogeogr. Palaeoclimatol. Palaeoecol. 283 (1–2), 91–98. https://doi.org/10.1016/j.palaeo.2009.09.009.

Spicer, R.A., Yang, J., Spicer, T.E.V., Farnsworth, A., 2021. Woody dicot leaf traits as a palaeoclimate proxy: 100 years of development and application. In: Palaeogeography, Palaeoclimatology, Palaeoecology, 562. Elsevier B.V. https://doi.org/10.1016/j.palaeo.2020.110138.

Suarez, M.B., González, L.A., Ludvigson, G.A., 2011. Quantification of a greenhouse hydrologic cycle from equatorial to polar latitudes: The mid-Cretaceous water bearer revisited. Palaeogeogr. Palaeoclimatol. Palaeoecol. 307 (1–4), 301–312. https://doi.org/10.1016/j.palaeo.2011.05.027.

Suarez, C.A., González, L.A., Ludvigson, G.A., Kirkland, J.I., Cifelli, R.L., Kohn, M.J., 2014. Multi-taxa isotopic investigation of paleohydrology in the lower cretaceous cedar mountain formation, Eastern Utah, U.S.A.: Deciphering effects of the nevadaplano plateau on regional climate. J. Sediment. Res. 84 (11), 975–987. https://doi.org/10.2110/jsr.2014.76.

Tabor, C.R., Poulsen, C.J., Lunt, D.J., Rosenbloom, N.A., Otto-Bliesner, B.L., Markwick, P.J., Brady, E.C., Farnsworth, A., Feng, R., 2016. The cause of Late Cretaceous cooling: A multimodel-proxy comparison. Geology 44 (11), 963–966. https://doi.org/10.1130/G38363.1.

Tardif, D., Toumoulin, A., Fluteau, F., Donnadieu, Y., Le Hir, G., Barbolini, N., Licht, A., Ladant, J.-B., Sepulchre, P., Viovy, N., Hoorn, C., Dupont-Nivet, G., 2021. Orbital variations as a major driver of climate and biome distribution during the greenhouse to icehouse transition. Sci. Adv. (7) https://www.science.org.

Thorne, R.L., Roberts, S., Herrington, R., 2012. Climate change and the formation of nickel laterite deposits. Geology 40 (4), 331–334. https://doi.org/10.1130/G32549.1.

Tierney, J.E., Tingley, M.P., 2014. A Bayesian, spatially-varying calibration model for the TEX86 proxy. Geochim. Cosmochim. Acta 127, 83–106. https://doi.org/10.1016/j.gca.2013.11.026.

Tierney, J.E., Tingley, M.P., 2015. A TEX 86 surface sediment database and extended Bayesian calibration. Sci. Data 2. https://doi.org/10.1038/sdata.2015.29.

Tierney, J.E., Poulsen, C.J., Montañez, I.P., Bhattacharya, T., Feng, R., Ford, H.L., Hönisch, B., Inglis, G.N., Petersen, S.V., Sagoo, N., Tabor, C.R., Thirumalai, K., Zhu, J., Burls, N.J., Foster, G.L., Goddéris, Y., Huber, B.T., Ivany, L.C., Turner, S.K., Zhang, Y.G., 2020. Past climates inform our future. In: Science (Vol. 370, Issue 6517). American Association for the Advancement of Science. https://doi.org/10.1126/science.aay3701.

Trewartha, G., 1968. An Introduction to Climate, 4th ed. McGraw-Hill Kogakusha.

Ufnar, D.F., González, L.A., Ludvigson, G.A., Brenner, R.L., Witzke, B.J., 2004. Evidence for increased latent heat transport during the Cretaceous (Albian) greenhouse warming. Geology 32 (12), 1049–1052. https://doi.org/10.1130/G20828.1.

Valdes, P.J., Armstrong, E., Badger, M.P.S., Bradshaw, C.D., Bragg, F., Crucifix, M., Davies-Barnard, T., Day, J.J., Farnsworth, A., Gordon, C., Hopcroft, P.O., Kennedy, A.T., Lord, N.S., Lunt, D.J., Marzocchi, A., Parry, L.M., Pope, V., Roberts, W.H.G., Stone, E.J., Williams, J.H.T., 2017. The BRIDGE HadCM3 family of climate models: HadCM3@Bristol v1.0. Geosci. Model Dev. 10 (10), 3715–3743. https://doi.org/10.5194/gmd-10-3715-2017.

Valdes, P.J., Lunt, D.J., Scotese, C.R., 2018. Modelling the climate history of the phanerozoic. In: American Geophysical Union Fall Meeting 2018.

Valdes, P.J., Scotese, C.R., Lunt, D.J., 2021. Deep ocean temperatures through time. Clim. Past 17 (4), 1483–1506. https://doi.org/10.5194/cp-17-1483-2021.

Vaughan, A.P.M., 2007. A Phanerozoic perspective. In: Williams, M., Haywood, A.M., Gregory, F.J., Schmidt, D.N. (Eds.), Deep-Time Perspectives on Climate Change: Marrying the Signal from Computer Models and Biological Proxies. Micropalaeontological Society Special Publication, Geological Society of London, pp. 5–59.

Veizer, J., Prokoph, A., 2015. Temperatures and oxygen isotopic composition of Phanerozoic oceans. Earth Sci. Rev. 146, 92–104. https://doi.org/10.1016/j.earscirev.2015.03.008.

Vérard, C., Veizer, J., 2019. On plate tectonics and ocean temperatures. Geology 47 (9), 881–885. https://doi.org/10.1130/G46376.1.

Voigt, S., Wilmsen, M., Mortimore, R.N., Voigt, T., 2003. Cenomanian palaeotemperatures derived from the oxygen isotopic composition of brachiopods and belemnites: Evaluation of Cretaceous palaeotemperature proxies. Int. J. Earth Sci. 92, 285–299. https://doi.org/10.1007/s00531-003-0315-1.

Walliser, E.O., Schöne, B.R., 2020. Paleoceanography of the Late Cretaceous northwestern Tethys Ocean: Seasonal upwelling or steady thermocline? PLoS One 15, 1–26. https://doi.org/10.1371/journal.pone.0238040.

Wegener, A.L., 1912a. Die Entstehung der Kontinente [The origin of continents]. Geol. Rundsch. 3, 276–292.

Wegener, A.L., 1912b. Die Entstehung der Kontinente [The origin of continents]. Petermanns Geogr. Mitt. 58 (185–195).

Wegener, A.L., 1915. Die Entstehung der Kontinente und Ozeane [The origin of continents and oceans].

Wijeysundera, H.C., Wang, Tomlinson, Ko, D., Krahn., 2012. Techniques for estimating health care costs with censored data: an overview for the health services researcher. ClinicoEcon. Outcomes Res. 145 https://doi.org/10.2147/CEOR.S31552.

de Winter, N.J., Müller, I.A., Kocken, I.J., Thibault, N., Ullmann, C.V., Farnsworth, A., Lunt, D.J., Claeys, P., Ziegler, M., 2021. Absolute seasonal temperature estimates from clumped isotopes in bivalve shells suggest warm and variable greenhouse climate. Commun. Earth Environ. 2, 1–8. https://doi.org/10.1038/s43247-021-00193-9.

Xu, J., Morris, P.J., Liu, J., Holden, J., 2018. PEATMAP: refining estimates of global peatland distribution based on a meta-analysis. CATENA 160, 134–140.

Zakharov, Y.D., et al., 2005. Seasonal temperature fluctuations in the high northern latitudes during the Cretaceous Period: Isotopic evidence from Albian and Coniacian shallow-water invertebrates of the Talovka River Basin. Koryak Upland Russ. Far East Cretaceous Res. 26, 113–132. https://doi.org/10.1016/j.cretres.2004.11.005.

Zakharov, Y.D., Popov, A.M., Shigeta, Y., Smyshlyaeva, O.P., Sokolova, E.A., Nagendra, R., Velivetskaya, T.A., Afanasyeva, T.B., 2006. New Maastrichtian oxygen and carbon isotope record: Additional evidence for warm low latitudes. Geosci. J. 10, 347–367. https://doi.org/10.1007/BF02910375.

Zhang, L., Wang, C., Li, X., Cao, K., Song, Y., Hu, B., Lu, D., Wang, Q., Du, X., Cao, S., 2016. A new paleoclimate classification for deep time. Palaeogeogr. Palaeoclimatol. Palaeoecol. 443, 98–106. https://doi.org/10.1016/j.palaeo.2015.11.041.

Ziegler, A.M., Rowley, D.B., Lottes, A.L., Sahagian, D.L., Hulver, M.L., Gierlowski, T.C., 1985. Paleogeographic interpretation: with an example from the Mid-Cretaceous. Annu. Rev. Earth Planet. Sci. 13, 385.